CIVIL ENGINEERING STUDIES

STRUCTURAL RESEARCH SERIES NO. 340

LUMPED-PARAMETER ANALYSIS OF CYLINDRICAL PRESTRESSED CONCRETE REACTOR VESSELS

By

A. Echeverria Gomez

and

W. C. Schnobrich

Subcontract No. 2906
Under Contract No. W-7405-eng-26

A REPORT ON AN INVESTIGATION
CARRIED OUT AS PART OF THE
PRESTRESSED CONCRETE REACTOR VESSEL PROGRAM
OF THE
OAK RIDGE NATIONAL LABORATORY

Operated by
Union Carbide Corporation
for the
U. S. Atomic Energy Commission

UNIVERSITY OF ILLINOIS

URBANA, ILLINOIS

DECEMBER, 1968

CIVIL ENGINEERING STUDIES
STRUCTURAL RESEARCH SERIES NO. 340

LUMPED-PARAMETER ANALYSIS OF CYLINDRICAL PRESTRESSED CONCRETE REACTOR VESSELS

By

A. Echeverria Gomez
and
W. C. Schnobrich

DECEMBER 1968

Subcontract No. 2906
Under Contract No. W-7405-eng-26

A Report on an Investigation
carried out as part of the
Prestressed Concrete Reactor Vessel Program
of the
Oak Ridge National Laboratory

Operated by
Union Carbide Corporation
for the
U. S. Atomic Energy Commission

University of Illinois
Urbana, Illinois

ACKNOWLEDGMENT

This thesis study was conducted under the immediate direction of Dr. W. C. Schnobrich, Professor of Civil Engineering.

The investigation was undertaken as a part of a program in the Department of Civil Engineering. This program is supported by the U. S. Atomic Energy Commission, under contract AEC UCC Subcontract 2906.

The author wishes to express his recognition and thanks to Dr. Schnobrich for his continuous guidance and encouragement and to Dr. B. Mohraz, Assistant Professor of Civil Engineering, for his constructive criticism and invaluable suggestions regarding this study.

Acknowledgment is also due to the personnel of the Department of Computer Science for their cooperation in the use of their facilities, especially the IBM 360-50/75 digital computer system.

TABLE OF CONTENTS

TABLE OF CONTENTS (Continued)

LIST OF FIGURES

LIST OF FIGURES (Continued)

I. INTRODUCTION

1.1. General

The use of nuclear energy in the production of electrical power involves substantial structural systems comprised of pressure and containment vessels that house the nuclear reactor. Efficient operation of a nuclear plant requires a large electrical output. This requirement means structures of sizeable dimensions.

Most of the water-cooled nuclear reactors in operation at present are sheltered by two major structural units: the primary pressure vessel and the secondary containment vessel. The primary container is normally a steel pressure vessel whose basic function is to hold the coolant system's pressure. This vessel is surrounded by a massive concrete primary shielding structure. The secondary structure, the containment vessel, encloses the primary container providing a second protective shield.

An alternate to the use of liquid coolants is a pressurized gas system. The gas-cooled reactor calls for a large core space, which requires the construction of much larger primary pressure vessels. The inherent difficulties that would be involved in the transportation and construction of steel units of the size necessary for gas-cooled reactors have led to the need for a more versatile type of structure. The vessel must be built on site and meet the serviceability and safety requirements. The solution adopted has been the use of prestressed concrete reactor vessels (PCRV's), which not only serve to hold the coolant system but also provide the shielding and containment. Most

of the existing PCRV units have been built in the United Kingdom and France.[13] The first nuclear reactor of this type in the United States will be the Fort St Vrain high-temperature gas-cooled reactor. The design and construction of this plant, is being performed by Gulf General Atomic, for the Public Service Company of Colorado.[24]

The basic principle in the design of this type of structure is analogous to that of the prestressed concrete beam or slab. The fundamental concept is to precompress the walls of the vessel to such a level that the tension caused by interior pressure, temperature and other service loads, is balanced by the initial prestress resulting in an essentially stress free container (load balancing concept). This zero stress situation can not be accomplished exactly throughout the entire structure. Stress gradients are too sharp in some regions. In those regions, particularly where discontinuities are present, some high tensions exist requiring special reinforcement provisions.

Overall, the load carrying members of the vessel are the prestressing tendons. The concrete serves to transmit the pressure loads to the tendons and to provide the shielding of a containment vessel.

The shapes used for prestressed vessels have varied from a cylinder bounded by two inverted, nonprestressed, hemispherical heads (Marcoule Vessels, France), to a spherical shell (Wylfa vessels, England).[13,24] The current trend of prestressed concrete vessel configurations in the United States, as well as in Europe, is to thick walled cylinders delimited by flat end slabs. This study is concerned with such a cylinder-flat end slab vessel configuration.

Most of the conventional methods of analysis for pressure vessels are based on thin shell theory. This approach, although quite suitable for steel vessels, can only be used to a limited extent for prestressed concrete vessels. Since prestressed concrete vessels are thick-walled structures the assumptions of thin shell theory are not valid.

A wide variety of methods has been utilized for the analysis and design of PCRV's. The range extends from the compatibility method[3] to sophisticated procedures based on the finite element and finite difference techniques. Model testing has also been used to confirm and amplify the results of analytical studies. One of the analytical procedures used rather extensively by the British designers is the dynamic relaxation method.[17,18] Dynamic relaxation is a direct application of the finite difference concept that is closely related to the lumped parameter method of analysis employed in this study. The American design approach has been, basically, the finite element procedure,[19,20] duly complemented by model tests.

A very important feature of the finite difference and finite element methods is their flexibility in dealing with almost any vessel configuration. Even problems associated with openings in the vessels can be conveniently studied by extending these methods to a three-dimensional analysis.[19]

Reactor vessels have several major openings as needed for the operation of the unit. These openings introduce discontinuities resulting in localized concentration of stresses. Although this fact cannot be overlooked when designing the unit, the assumption of

axi-symmetry is an extremely good approximation insofar as the overall structural behavior of the vessel is concerned.

Design, according to current standards, is satisfied by elastic analysis of the pressure vessel. A commonly accepted design criterion consists in requiring that the structure exhibit an elastic response under all possible combinations of design and test loads. The importance of an analysis which goes beyond the elastic limit and therefore indicates the mechanism by which the structure fails should be recognized. Such an analysis should provide for the detection of incipient failure, and the evaluation of damage and serviceability in case of an accidental increase of the loads beyond the operating levels.

As already mentioned, a PCRV is intended to perform the functions of both the primary and secondary containers. As such, it is mandatory that the mode of failure of the vessel be essentially ductile. There is no second line of defense. For a particular vessel configuration, the failure of the unit may result from any of several different yet possible mechanisms. The predominance of one mechanism over the others depends upon the relative dimensions of the elements which make up the vessel and the level of prestressing. Some form of ultimate analysis is the only certain way to determine the failure mechanism for a given prestressed concrete pressure vessel.

In the case of cylindrical vessels with flat ends, the failure mechanism may be associated with the cylindrical wall or the slab.

The wall, prestressed longitudinally by straight or slightly curved cables and laterally confined by some type of circumferential prestressing, can fail by either of two basic mechanisms:

(a) longitudinal tensile stresses exceeding the longitudinal prestress, resulting in a horizontal fracture near the midsection of the vessel, or (b) circumferential tension, resulting in longitudinal cracks that eventually split the vessel into slices. Since these two modes of failure are controlled by the prestressing tendons, they are essentially ductile.

The slab, whether reinforced or unreinforced, is laterally confined. It may fail as a consequence of: (a) bending, developing into generalized yielding, or (b) shear, characterized by part or all of the slab suddenly punching out.

The shear mode of failure is brittle and, for this reason, must be avoided. The shear failure of the end slab of a PCRV is similar, in consequence, to that of the steel pressure vessel when used as primary container for water-cooled reactors. A steel pressure vessel, being in a state of nearly uniform tension, exhibits a sudden failure which results in the complete destruction of the unit. The possibility of a shear mode of failure in a PCRV develops as undesirable a vessel as a steel vessel.

The ultimate analysis then becomes a necessary tool in selecting the right dimensions and prestressing to assure a design with a ductile mode of failure.

1.2. Description of the Type of Vessels Under Study

1.2.1. The Vessels

In accordance with the present trends in the construction of prestressed concrete nuclear reactor vessels (PCRV's), the pressure

vessel under study is a thick-walled concrete cylinder with flat ends. The ends are thick circular slabs built monolithically with the wall. This analysis considers the case of a vessel free from openings.

A vertical cross section through the vessel is shown in Fig. 1. Two different types of prestressing provide the structural integrity for this unit: (a) longitudinal prestressing, supplied by a set of high-strength steel cables or rods placed inside the cylindrical wall, at a specified distance from its interior face; (b) circumferential or hoop prestressing, provided by either a single cable helically wrapped around the cylindrical body, or by a series of independent cables prestressed individually. As shown in Fig. 2 the longitudinal tendons are uniformly spaced and arranged in an annular manner. The prestressing loads are transmitted to the head through steel plates, which distribute the high reactive stresses to the neighboring area.

The longitudinal cables, representing prestressing tendons in the full-scale vessel, can be grouted or ungrouted. Although both cases have been considered in the analysis, the results presented later correspond only to the ungrouted case. Because the circumferential prestressing occupies a peripheral position, it has been treated as an ungrouted tendon.

1.2.2. The Loads

Two types of loading are considered to be acting on the vessel: the prestressing applied to the concrete unit and the internal pressure.

The first type of load is, in general, the combination of the initial applied prestressing and the increase in prestressing due to the deformations induced in the vessel through the application of internal pressure. The second loading, internal pressure, simulates the effect of the pressurized gases contained by the PCRV. In the case of an operational accident, this internal pressure may build up high enough to force the structure into inelastic behavior.

Because of the uniform arrangement of the prestressing cables and the axi-symmetry of the vessel, the loads acting on the structure are also axi-symmetric.

The temperature gradient that develops during the operation of the unit, although a very important aspect in the design of a reactor vessel, is not considered in this analysis.

1.3. Object and Scope

The object of this study is the development of a mathematical procedure suitable for the analysis of prestressed concrete pressure vessels in both the elastic and inelastic ranges. It has been found that a lumped parameter approach offers a number of advantages in the treatment of localized inelastic behavior. The analogue used here is an extension of the lumped parameter model developed at the University of Illinois. The model was initially used for a study of contained plastic flow problems.[11]

Axial and radial displacements, as well as stresses and strains, are calculated at various points in the body of the vessel at various stages of loading. Material properties, at the nodes

representing the continuum, are evaluated according to whether elastic behavior or cracking prevails at that particular location. A cracking table, showing such a status, is produced every time that the tensile strain at a new node exceeds a specified level, taken as the cracking criterion.

The numerical results obtained illustrate the behavior of a sample vessel from the regular operational level of internal pressure to the advanced state of cracking which precedes complete failure. The mode of failure of the unit is inferred from this ultimate analysis.

A comparison is made with some experimental results obtained from a series of tests on small-scale pressure vessels at the Structural Laboratory of the University of Illinois.

1.4. Nomenclature

Each symbol used in the test is explained when it is first introduced. However, a summary of the notation is also presented below for convenience of reference.

A_{cp}	cross-sectional area of the circumferential prestressing cable or cables
$A_{\ell p}$	cross-sectional area of the longitudinal prestressing cables
[C]	orthotropic stress-strain coefficient matrix after cracking
{d}	grid displacement vector
D	external diameter of vessel
E_c	Young's modulus of concrete
E_{st}	Young's modulus of steel

F	scale factor on increment of internal pressure to the formation of a new crack
F_{cp}	prestressing force in the circumferential prestressing cables
$F_{\ell p}$	prestressing force in the longitudinal prestressing cables
F_r^a, F_r^b	radial forces acting on element faces a,b
F_z^c, F_z^d	longitudinal forces acting on element faces c,d
F_θ^{ij}	circumferential force acting on element radial faces
H	height of vessel
$[M]$	coefficient matrix for the discrete system of equilibrium equations
n	number of displacement nodes in the grid
N	number of longitudinal prestressing cables
p	applied internal pressure
$\{P\}$	load vector
P_{rk}	load in the r direction for the kth displacement node
P_{zk}	load in the z direction for the kth displacement node
r,z,θ	polar cylindrical system of coordinates
s	spacing of circumferential prestressing cables
$[S]$	elastic stress-strain coefficient matrix
t_c	cylindrical wall thickness
t_s	slab thickness
$T_{rz}^a, T_{rz}^b, T_{rz}^c, T_{rz}^d$	shear forces at element faces a,b,c,d
$[T_\epsilon]$	strain transformation matrix from r,z,θ coordinate system to I,II,θ principal directions
u	displacement in the radial direction

u_{ij}	radial displacement at node (i,j)
w	displacement in the longitudinal direction
w_{ij}	longitudinal displacement at node (i,j)
I,II,θ	cartesian system of coordinates in the principal strain directions
β	angle between the maximum principal strain and the r axis
$\gamma_{rz},\gamma^{a}_{rz}$	shear strain in the rz-plane; superscript refers to the node where strain is defined
$\Delta F_{\ell p}$	increment of prestressing force in an ungrouted longitudinal cable caused by vessel deformations
$\Delta F^{ij}_{\ell p}$	increment of prestressing force in a grouted longitudinal cable caused by local deformations at node (i,j)
Δp	internal pressure increment
$\Delta\epsilon_r,\Delta\epsilon_z,\Delta\epsilon_\theta,\Delta\gamma_{rz}$	strain increments caused by Δp increase of internal pressure
$\Delta\theta/2$	dihedral angle between two radial grids
Δw	longitudinal displacement increment at distribution plate
$\{\epsilon\}$	strain vector in the r,z,θ coordinate system
$\{\epsilon_p\}$	principal strain vector
ϵ_{cr}	cracking strain criterion
$\epsilon_r,\epsilon^{a}_{r}$	radial strain; superscript refers to the node where strain is defined
$\epsilon^{cr}_r,\epsilon^{cr}_z,\epsilon^{cr}_\theta,\gamma^{cr}_{rz}$	nodal strains at incipient cracking
$\epsilon^{pr}_r,\epsilon^{pr}_z,\epsilon^{pr}_\theta,\gamma^{pr}_{rz}$	nodal strains after cracking
ϵ_I,ϵ_{II}	principal strains in plane rz
ϵ_θ	circumferential strain

λ_r	grid length in the r direction
λ_z	grid length in the z direction
ν	Poisson's ratio of concrete
$\{\sigma\}$	stress vector in the r,z,θ coordinate system
σ_{cp}	equivalent circumferential prestressing pressure
$\{\sigma_p\}$	principal stress vector
$\sigma_r, \sigma_r^a, \sigma_r^b$	radial stress; superscript identifies particular stress
$\bar{\sigma}_r^b$	equivalent radial stress at the re-entrant corner, represents internal pressure and interaction stresses at the node
$\sigma_z, \sigma_z^c, \sigma_z^d$	longitudinal stress; superscript identifies particular stress node
σ_θ	circumferential stress
$\tau_{rz}, \tau_{rz}^a, \tau_{rz}^b$	shear stress in the rz plane; superscript identifies particular stress node

II. METHOD OF ANALYSIS

2.1. Governing Equations

For the purpose of presenting the governing differential equations, the axi-symmetric body shown in Figs. 3(a) and 3(b) is considered. The position of an element in the plane of a cross section is defined by means of the cylindrical polar system of coordinates r,z,θ; z has been chosen to coincide with the axis of symmetry, r points outwards from this axis in a radial direction, and θ is the central angle measured from an arbitrary chosen base meridional plane. The components of displacements in the radial, and longitudinal directions are denoted by u and w respectively. The standard notation σ_r, ϵ_r, σ_z, ϵ_z, σ_θ, ϵ_θ, $\tau_{\theta z}$, $\gamma_{\theta z}$ [25] is used to indicate stresses and strains in the r, z, and θ directions.

According to small displacement theory, the components of strain for axially symmetric deformations in polar cylindrical coordinates are:

$$\epsilon_r = \frac{\partial u}{\partial r} \quad , \qquad \gamma_{rz} = \frac{\partial u}{\partial z} + \frac{\partial w}{\partial r}$$

$$\epsilon_z = \frac{\partial w}{\partial z} \quad , \qquad \gamma_{r\theta} = 0 \qquad (2.1)$$

$$\epsilon_\theta = \frac{u}{r} \quad , \qquad \gamma_{\theta z} = 0$$

Considering the infinitesimal element shown in Fig. 3, the equations of equilibrium can be derived by projecting forces on the coordinate axes. From equilibrium of forces in the r direction:

$$(\sigma_r + \frac{\partial \sigma_r}{\partial r} dr)(r + \frac{dr}{2})d\theta dz - \sigma_r(r - \frac{dr}{2})d\theta dz$$

$$+ (\tau_{rz} + \frac{\partial \tau_{rz}}{\partial z} dz)rd\theta dr - \tau_{rz}rd\theta dr - 2\sigma_\theta drdz \frac{d\theta}{2} = 0$$

in the z direction:

$$(\sigma_z + \frac{\partial \sigma_z}{\partial z} dz)rd\theta dr - \sigma_z rd\theta dr + (\tau_{rz} + \frac{\partial \tau_{rz}}{\partial r} dr)(r + \frac{dr}{2})d\theta dz$$

$$- \tau_{rz}(r - \frac{dr}{2})d\theta dz = 0$$

This derivation is presented here in order to emphasize the similarities between the differential equations for the continuum and the discrete equations for the model. A comparison of the equations for the continuum with those of the discrete system, developed subsequently, shows that there is a one to one correspondence between the two sets of equations when 2nd and higher order terms are neglected.

Rearranging, and neglecting second order terms, the differential equation of equilibrium can be written as:

$$\frac{\partial \sigma_r}{\partial r} + \frac{\partial \tau_{rz}}{\partial z} + \frac{\sigma_r - \sigma_\theta}{r} = 0 \qquad (2.2)$$

for the r direction, and

$$\frac{\partial \sigma_z}{\partial z} + \frac{\partial \tau_{rz}}{\partial r} + \frac{\tau_{rz}}{r} = 0 \qquad (2.3)$$

for the z direction.

2.2. Selection of the Method of Analysis

A survey of the different methods available for the analysis of axi-symmetric bodies reveals that the most suitable approach to the solution of this three-dimensional problem is through the use of a discrete mathematical model. An important consideration in the selection of the discrete mathematical model is the adaptability of the procedure to the treatment of cracking and inelastic behavior.

The conventional compatibility method, which has been frequently used in the preliminary design of nuclear reactor containment vessels, is not well suited to include consideration of local plastic and/or fracture properties of the material. The same limitations are in general true for the theories of thick or moderately thick shells, such as the one recently developed by Martinez-Marquez.[14] The finite element procedure, although very promising, has been employed only recently in the treatment of inelastic behavior.

The finite difference technique is rarely used directly. Instead, various methods based on the theory of finite differences have been devised to tackle specific problems. These methods make use of models that provide a physical representation of the continuum and facilitate the introduction of boundary conditions. The equations for such models are consistent with the corresponding finite difference equations. An outstanding example of these methods is Otter's dynamic relaxation.[17,18]

The lumped parameter model is a quite simple and yet versatile method for obtaining solutions to continuum problems. In particular, it is capable of treating localized inelastic behavior. Lumped

parameter models have been used extensively at the University of Illinois to solve a variety of problems, including the elastic and plastic behavior of thin shells[15,22,23] and thick circular plates,[9] wave and crack propagation through a continuum,[1,4,7,10] and circular plates undergoing large displacements.[6]

The lumped parameter model consists of a network of rigid bars joining deformable nodes arranged to form a finite degree of freedom approximation to the actual structure. The mechanical properties of the continuum are discretized at these deformable nodes, where the complete strain and stress tensors are defined. This way, when the equilibrium equations are written for a mass delimited by the six neighboring extensional nodes, any kind of behavior: elastic, plastic, fracture, or even local anisotropies, can be easily incorporated for those problems where such considerations are necessary.

This versatility in treating the properties of the continuum is very significant, especially when dealing with concrete, a material that exhibits a very complex elastic-plastic behavior in compression and an elastic-fracture behavior when in tension.

The model is perfectly consistent with the differential equations governing the continuum. It will be shown later that the mathematical relations employed are equivalent to the central difference analogues of the respective governing equations.

The simplicity in introducing boundary conditions and the physical interpretation that the model itself provides are additional assets of this method.

2.3. Description of the Lumped Parameter Model

The lumped parameter model is composed of mass or displacements nodes and deformable or stress nodes, arranged in a prescribed pattern. Their relative position, in the three-dimensional grid representing the vessel is shown in Fig. 4.

Polar cylindrical coordinates r,z,θ, are used to fit the configuration of the vessel. The mesh lengths, i.e., the distance between two consecutive displacement nodes belonging to the same radial section, are λ_r and λ_z in the radial and vertical directions. Two contiguous radial sections are separated by the dihedral angle $\Delta\theta/2$, which encloses the material corresponding to a pie-shaped segment that contains and is centered about one longitudinal prestressing cable. Thus, the numerical value of dihedral angle equals 360° divided by the number of longitudinal cables.

The displacements u and w are measured in the r and z directions at the location of each mass node. A deformable node is the point of definition of the complete average strain and stress tensors in an element enclosed by the six neighboring displacement nodes. Three orthogonal springs provide the physical representation of the extensional properties in the radial, vertical and tangential directions, while circular rings, in the rz plane, simulate the shear properties. Since there are no shear deformations in the $r\theta$ and θz planes, because of axi-symmetry, the corresponding rings have been omitted in Fig. 4(a).

The condition of axi-symmetry simplifies the study of the structure. To obtain a complete solution for the vessel it is

sufficient to analyze a single radial section, with due consideration given to the direct circumferential strains and stresses. Because of symmetry, only one quarter of the vessel's cross section is sufficient to describe the entire vessel's behavior.

A typical grid arrangement, for the radial cross section representing the vessel, is illustrated in Fig. 5. Two coordinate systems serve to identify the position of the different nodes in the mesh. The r,z coordinates, mentioned above, have their origin at the center of the cylindrical cavity. The discrete coordinates i,j take on only integer values. The coordinate i=1 is the locus of the points on the axis of the cylinder, and j=1 is the locus of those points lying in the horizontal plane of symmetry at mid-height of the vessel. The symmetry condition at mid-height is represented by a roller support which, while introducing a rotational constraint, allows lateral displacements of the wall.

2.4. Basic Definitions and Relations for the Model

2.4.1. Strain-Displacement Relationships

A typical element in the model is enclosed, as indicated above, by the six neighboring stress nodes. The strain tensor, defined at the location of a stress node, is evaluated directly from the displacements measured at the surrounding mass nodes.

Using the nodal numbering system shown in Fig. 6, the strain-displacement relationships for stress node a are:

$$\epsilon_r^a = \frac{u_{i+2j} - u_{ij}}{\lambda_r}$$

$$\epsilon_z^a = \frac{w_{i+1j+1} - w_{i+1j-1}}{\lambda_z} \qquad (2.4)$$

$$\epsilon_\theta^a = \frac{1}{r_{i+1}} \frac{u_{i+2j} + u_{ij}}{2}$$

$$\gamma_{rz}^a = \frac{u_{i+1j+1} - u_{i+1j-1}}{\lambda_z} + \frac{w_{i+2j} - w_{ij}}{\lambda_r}$$

where ϵ_r^a, ϵ_z^a, ϵ_θ^a and γ_{rz}^a are the radial, longitudinal, tangential and shear strains at stress node a; u_{ij}, w_{ij}, u_{i+2j}, w_{i+2j}, u_{i+1j+1}, w_{i+1j+1}, etc., are the radial and longitudinal displacements at mass nodes whose discrete coordinates are (i,j), (i+2,j), (i+1,j+1), etc.; r_{i+1} is the r coordinate of stress node a. Since displacements are only defined at the mass nodes, i.e., u_{i+1j} does not have any meaning in terms of the model, ϵ_θ has been expressed as the average of the displacements u_{i+2j} and u_{ij}.

In the original model, as developed by Harper and Ang,[11] two consecutive radial grids are analyzed simultaneously. In this way both displacements, u and w, as well as the stress and strain tensors appear completely defined at every single node in the network. The averaging process described above, in connection with the equation for ϵ_θ, is avoided, but in so doing, the number of equations to be solved is approximately twice as large as the number required for the model presented here. The results obtained with the single net model show that this averaging approximation is perfectly valid.

The strain-displacement relationships given by Eqs. 2.4 are the central finite differences equivalents of the corresponding differential equations.

2.4.2. Equations of Equilibrium

The equations of equilibrium for an element, represented in the grid system by a displacement node, are related to the displacements defined at the nine neighboring nodes, including the one corresponding to the element in question. Figure 6 shows such a set of displacement and stress nodes.

The networks shown in Fig. 7 are composed of u and w displacement nodes and direct and shear stress nodes. Horizontally the u displacement nodes alternate with direct stress nodes, represented by two orthogonal springs, and the displacements nodes alternate with shear stress nodes, represented by rings. Only one of these grids is needed for the finite approximation to the vessel in the elastic range. In fact, such a grid would be the perfect physical analogue for Otter's dynamic relaxation method.[17] However, the Otter model is not amenable to plastic behavior and has a physical separation of the points of definition of the various components of both the stress and the displacement vectors.

The typical mass element corresponding to displacement node ij in grid 1, Fig. 7(a), has dimensions λ_r, λ_z, $\Delta\theta$. Figure 8 shows this element and the forces participating in the r equation. These forces are:

$$
\begin{aligned}
F_r^a &= \sigma_r^a \, r_{i+1} \, \Delta\theta \, \lambda_z \\
F_r^b &= \sigma_r^b \, r_{i-1} \, \Delta\theta \, \lambda_z \\
F_\theta^{ij} &= \sigma_\theta^{ij} \, \lambda_r \lambda_z \\
T_{rz}^c &= \tau_{rz}^c \, r_i \, \Delta\theta \, \lambda_r \\
T_{rz}^d &= \tau_{rz}^d \, r_i \, \Delta\theta \, \lambda_r
\end{aligned}
\qquad (2.5)
$$

Since

$$
r_{i+1} = r_i + \frac{\lambda_r}{2} \qquad \text{and} \qquad r_{i-1} = r_i - \frac{\lambda_r}{2} \ ,
$$

the sum of the projections on the r-axis yields:

$$
\sigma_r^a (r_i + \frac{\lambda_r}{2}) \Delta\theta \lambda_z - \sigma_r^b (r_i - \frac{\lambda_r}{2}) \Delta\theta \lambda_z + \tau_{rz}^c r_i \Delta\theta \lambda_r
$$

$$
- \tau_{rz}^d r_i \Delta\theta \lambda_r - 2\sigma_\theta \lambda_r \lambda_z \frac{\Delta\theta}{2} = 0
$$

after simplifying, the r equation becomes:

$$
\frac{\sigma_r^a - \sigma_r^b}{\lambda_r} + \frac{\tau_{rz}^c - \tau_{rz}^d}{\lambda_z} + \frac{\frac{1}{2}(\sigma_r^a + \sigma_r^b) - \sigma_\theta}{r_i} = 0 \qquad (2.6)
$$

Figure 9 shows the mass element associated with displacement node ij in grid 2, Fig. 7(b). The longitudinal forces acting on it are:

$$
\begin{aligned}
F_z^c &= \sigma_z^c \, r_i \, \Delta\theta \lambda_r \\
F_z^d &= \sigma_z^d \, r_i \, \Delta\theta \lambda_r
\end{aligned}
$$

$$T^a_{rz} = \tau^a_{rz} r_{i+1} \Delta\theta \lambda_z \qquad (2.7)$$

$$T^b_{rz} = \tau^b_{rz} r_{i-1} \Delta\theta \lambda_z$$

Performing similar operations to those outlined above, the z equation is obtained,

$$\frac{\sigma^c_z - \sigma^d_z}{\lambda_z} + \frac{\tau^a_{rz} - \tau^b_{rz}}{\lambda_r} + \frac{\frac{1}{2}(\tau^a_{rz} + \tau^b_{rz})}{r_i} = 0 \qquad (2.8)$$

Equations 2.6 and 2.8 are mathematically consistent with the central finite difference analogues of the governing differential equations.

The displacement form of the equations of equilibrium is obtained by substituting the pertinent stress-strain and strain displacement relationships in Eqs. 2.6 and 2.8. These equilibrium equations in terms of displacements, for the typical element in the elastic range, are presented in the Appendix.

The model described in Section 2.3 is obtained by superimposing grid 1 on grid 2 (Fig. 7). By so doing, shear nodes combine with the direct stress node, and vice versa, thus defining complete stress and strain tensors at each point. Also both the u and w displacements are defined at each displacement node and represent components of a complete displacement vector. Every one of the component grids approximates one half of the continuum. The equations derived for the single grid model, are accordingly valid for the complete model. Since every one of the grids represents half of the vessel, and both of them act independently in the elastic stage, a mesh uncoupling problem can be expected. A study of the finite difference operators presented in

the Appendix exposes the problem. The best illustration can be found in the equilibrium equations for the typical node. The operator associated with the z equation is a perfect example of uncoupling. The terms in the equation refer exclusively to the displacements defined in a single network. In the r equation, however, a slight amount of coupling is obtained from the terms involving the w displacements defined one space above and below the central displacement node. These terms come from a Poisson effect and result from the averaging technique adopted for ϵ_z at (i,j).

A limited amount of coupling is also obtained from the Poisson effect in the special equations written for nodes located at the free and the loaded surfaces of the vessel. The operators presented in the Appendix, for nodes at or near these boundaries, illustrate this situation.

In spite of all these evidences of uncoupling, if the external forces are distributed properly into the two component networks, the results obtained for both systems are in very good agreement.

2.5. Prestressing

2.5.1. Longitudinal Prestressing

Two types of prestressing action can take place depending upon whether or not bond exists between the tendons and the concrete, i.e., whether the cables are grouted or ungrouted. The difference between the two, bonded and unbonded, is related to the additional prestressing load associated with the deformations of the vessel caused

by the application of internal pressure.

The increase in the prestressing load from an ungrouted tendon is proportional to the incremental vertical displacement at the distribution plate.

An ungrouted cable subjected to the increased deformation of the vessel is uniformly strained along its length. The existing strain is increased when the vessel elongates, as a consequence of the application of internal pressure. This increment in strain produces a proportional increment in the prestressing load acting on the vessel. Consequently, the prestressing load per cable is increased by:

$$\Delta F_{\ell p} = \Delta \epsilon_z E_{st} A_{\ell p} \tag{2.9}$$

where

$$\Delta \epsilon_z = \frac{\Delta w}{H/2} \tag{2.10}$$

Δw is the increment in vertical displacement at the distribution plate, caused by incrementing the internal pressure; H is the height of the vessel; E_{st}, the Young's modulus of the steel, and $A_{\ell p}$ is the cross-sectional area of the longitudinal cable.

Since the prestressing tendons are made of high-strength steel, the proportionality between deformations and the corresponding forces induced in the cables may be assumed to prevail throughout the complete loading process. Consequently, Eq. 2.9 holds at all stages of loading. The small deviations from the nonlinear stress-strain characteristics of the steel, as it nears its ultimate strength, are not significant.

The incremental effect in the grouted cable, on the other hand, is localized. It can be evaluated, at a particular point, by the expression:

$$\Delta F_{\ell p}^{ij} = \Delta \epsilon_z^{ij} E_{st} A_{\ell p} \tag{2.11}$$

where $\Delta \epsilon_z^{ij}$ is the longitudinal strain at (i,j) caused by the increase in internal pressure.

2.5.2. Circumferential Prestressing

As pointed out above, the circumferential prestressing is ungrouted. Its effect is comparable to a steel jacket confining the vessel laterally. Since the spacing of the hoops is normally small, the replacement of the prestressing steel by a cylindrical steel jacket is a perfectly valid assumption.

The equivalent pressure applied at the exterior surface of the cylindrical wall can be obtained by equating the prestressing force in one hoop, F_{cp}, to the resultant normal pressure acting on a ring of wall corresponding to the hoop spacing. See Fig. 10. The equivalent pressure, σ_{cp}, is:

$$\sigma_{cp} = \frac{2F_{cp}}{Ds} \tag{2.12}$$

where F_{cp} is the prestressing force, D is the exterior diameter of the vessel, and s is the spacing of the circumferential cables.

As in the case of the ungrouted longitudinal prestressing the increase in prestressing load caused by the incremental deformations of the wall is:

$$\Delta F_{cp} = \frac{\Delta u}{D/2} E_{st} A_{cp} \tag{2.13}$$

where Δu is the radial displacement increment at the exterior surface of the cylinder, and A_{cp} is the cross-sectional area of the cable.

III. CONSTITUTIVE RELATIONS OF THE MATERIALS

3.1. General

Two materials play a structural role in the prestressed concrete pressure vessel, concrete and steel. The concrete contains and transmits the pressure to the prestressing steel which provides the structural integrity to the vessel.

Concrete, as the material that constitutes the continuum in our analysis, can be assumed to be perfectly homogenous and isotropic. This is a universally accepted assumption at the macro scale of the structure.

For the most part, the concrete in the vessel is under a triaxial state of stress. This stress state becomes biaxial at or near the unloaded free surfaces. It is an accepted fact that concrete under a triaxial state of stress, in a purely compressive field, exhibits a marked increase in strength.[5,21] This strength increase is not quite clear in the case of a biaxial state of compressive stresses. However, if concrete is subjected to a biaxial state of tensile and compressive stresses, the resulting strength in both directions, is less than under uniaxial conditions.[2,16] Even though these trends are well-known, there is no general failure theory that fully describes the behavior of concrete under all multiaxial states of stress.

If concrete is idealized to behave as a perfectly elasto-plastic material in compression, a yield criterion like Tresca's or von Mises could be used at points of high compression. The analytical

results obtained in this study, however, show that the stress states which could possibly cause yielding in compression occur very late in the loading process. High compressive stresses are, actually, the consequence of an advanced degree of cracking. Inelastic behavior is both triggered and propagated through the continuum by a multiaxial state of stress where tensile stresses are present. Since cracking represents the primary contribution to nonlinear vessel behavior until the failure mechanism is clearly defined, considerations of plasticity have not been taken up in this study.

Concrete behavior in tension is essentially brittle, whether the state of stress is uniaxial or multiaxial. In this analysis, concrete is assumed to be perfectly elastic in tension right to the point when cracking occurs, i.e., to exhibit elastic-fracture behavior. It is further assumed that even for an advanced degree of inelastic structural behavior, the concrete under purely compressive stresses still has not reached a state of plasticity.

The prestressing steel in a pressure vessel is in a uniaxial state of tension. The only problem associated with the determination of its behavior is stress relaxation. The term stress relaxation refers to the loss of prestressing in a steel tendon while practically no change occurs in its length. At room temperature, this phenomenon is significant only after a long period of time following prestressing. This problem, of great importance in the design of nuclear reactors where the operational temperature is very high, is not taken into account in this study. The prestressing loads are considered to change only as a function of the variations in length of the tendons, caused by

deformations of the vessel under internal pressure. Since the prestressing cables are made of high-strength steel, the tendons can be expected to behave linearly from the application of the initial prestressing load up to vessel failure.

3.2. Elasticity Relations for the Continuum

The stress-strain relationships for a homogenous and isotropic material in the elastic region, are given by Hooke's law. In matrix form:

$$\{\sigma\} = [S]\{\epsilon\} \tag{3.1}$$

where $\{\sigma\}$ represents the stress vector; $[S]$, the matrix of elastic coefficients and $\{\epsilon\}$, the strain vector.

Since the shear stresses and strains in planes $r\theta$ and θz are identically equal zero, the expanded matrix form of Hooke's law becomes:

$$\begin{Bmatrix} \sigma_r \\ \sigma_z \\ \sigma_\theta \\ \tau_{rz} \end{Bmatrix} = \frac{E_c}{(1+\nu)(1-2\nu)} \begin{bmatrix} (1-\nu) & \nu & \nu & 0 \\ \nu & (1-\nu) & \nu & 0 \\ \nu & \nu & (1-\nu) & 0 \\ 0 & 0 & 0 & \frac{1}{2}(1-2\nu) \end{bmatrix} \begin{Bmatrix} \epsilon_r \\ \epsilon_z \\ \epsilon_\theta \\ \gamma_{rz} \end{Bmatrix} \tag{3.2}$$

where E_c is the modulus of elasticity of concrete, and ν its Poisson's ratio.

This set of relationships are assumed to describe the elastic behavior of concrete.

3.3. Orthotropic Properties in Cracking State

Because the vessel under study is axi-symmetric, only two directions exist for the crack to form: (a) a radial plane containing the longitudinal axis of the cylinder, and (b) a surface of revolution (conical if the crack as seen in the rz plane is straight) centered about the longitudinal axis. Figures 11 and 12 show these two types of cracks as they occur in the elemental unit corresponding to one stress node. The first type, the radial crack, results from the circumferential strain exceeding the specified limiting value assumed as the cracking criterion. The second form of cracking is related to the maximum principal strain in plane rz. Figure 13 illustrates the trace of this second type of crack in the radial plane. Axis I, in the direction of the maximum principal strain, forms an angle β with the r axis. Consequently, the second principal axis, axis II, coincides with the direction of the trace of the crack.

The stress-strain relationships for the isotropic material in its uncracked condition are given by Eqs. 3.1 and 3.2.

After the node has cracked it suddenly takes on orthotropic properties. These new orthotropic properties of the material, in the r,z and θ directions, are described by:

$$\{\sigma\} = [C]\{\epsilon\} \tag{3.3}$$

The matrix [C] can be obtained by the principle of conservation of energy between the two orthogonal sets of directions r,z,θ and I,II,θ. The energy equality is expressed by

$$\{\epsilon\}^T\{\sigma\} = \{\epsilon_p\}^T\{\sigma_p\} \tag{3.4}$$

where the subscript p is used to indicate principal quantities and the superscript T follows standard notation for the transpose of a vector or a matrix.

The stress-strain relationships at the cracked node are defined in accordance with the nature of the crack. Symbolically,

$$\{\sigma_p\} = [C_p]\{\epsilon_p\} \tag{3.5}$$

The vector $\{\epsilon_p\}$ is related to vector $\{\epsilon\}$ through the transformation:

$$\{\epsilon_p\} = [T_\epsilon]\{\epsilon\}$$

or

$$\begin{Bmatrix} \epsilon_I \\ \epsilon_{II} \\ \epsilon_\theta \end{Bmatrix} = \begin{bmatrix} \cos^2\beta & \sin^2\beta & 0 & \frac{1}{2}\sin^2\beta \\ \sin^2\beta & \cos^2\beta & 0 & -\frac{1}{2}\sin^2\beta \\ 0 & 0 & 1 & 0 \end{bmatrix} \begin{Bmatrix} \epsilon_r \\ \epsilon_z \\ \epsilon_\theta \\ \gamma_{rz} \end{Bmatrix} \tag{3.6}$$

Substituting Eq. 3.6 into Eq. 3.4 yields,

$$\{\epsilon\}^T[C]\{\epsilon\} = \{\epsilon\}^T[T_\epsilon]^T[C_p][T_\epsilon]\{\epsilon\} \tag{3.7}$$

Hence, the orthotropic properties in the r, z, θ directions, at the cracked node, are given by:

$$[C] = [T_\epsilon]^T[C_p][T_\epsilon] \tag{3.8}$$

The matrix [C] is a fully occupied matrix if the crack develops into the conical surface.

If the crack develops in the radial plane, the previous approach is unnecessary. For such a case [C] is given by:

$$[C] = \frac{E_c}{(1+\nu)(1-2\nu)} \begin{bmatrix} (1-\nu) & \nu & 0 & 0 \\ \nu & (1-\nu) & 0 & 0 \\ 0 & 0 & 0 & 0 \\ 0 & 0 & 0 & \frac{1}{2}(1-2\nu) \end{bmatrix} \qquad (3.9)$$

IV. BOUNDARY CONDITIONS

4.1. Introductory Remarks

As mentioned in the Introduction the lumped parameter model being used in this study, greatly facilitates the treatment of boundary conditions. The stepwise formulation of the equilibrium equations in terms of radial and longitudinal displacements, by incorporating stress-strain and strain-displacement relationships in the equilibrium equations, provides for the introduction of geometric and force boundary conditions in a simple and direct way.

The equilibrium equations for a point on or near the boundary is developed in exactly the same manner as is the equation for the typical mass node. A wedge-shaped element, properly dimensioned to represent the appropriate material, is loaded with the forces acting on its six bounding faces. These forces, which may be either external loads or resultants of stresses, integrated over the areas of the associated stress nodes, are projected on the r and z axes in order to generate the corresponding equilibrium equations. At this stage, boundary conditions imposed on stresses, can be introduced. Similarly, when substituting for strains and later for displacements, boundary conditions related to strains and displacements can be incorporated.

Boundary conditions at deformable nodes which lie on the boundaries require the re-formulation of the strain-displacement relationships. Equations 2.4, presented for the typical stress node, cannot be used because they would include displacements defined at points outside the model. The new strain-displacement relationships,

involving only displacements of nodes within the model, are obtained by specifying externally applied stresses at the boundary points.

If the stress-strain and strain-displacement relationships are substituted into the equilibrium equations, a set of finite difference-type operators is obtained. Each operator is an expression of the corresponding equilibrium equation written in terms of the displacements involved. The Appendix presents some of these operators developed for the material in elastic condition at various characteristic locations throughout the quarter section representing the vessel.

4.2. Nodes on the Axis of Symmetry

Since mass nodes on the longitudinal axis of symmetry can only move in a vertical direction, the radial displacements defined at these nodes are identically equal to zero. This condition, by itself, takes the place of the equilibrium equation in the r direction,

$$u_{1j} = 0 \tag{4.1}$$

The z equation is formulated by considering a special mass element. Figures 14(a) and (b) show such a special mass element located at the axis of symmetry. The forces acting on the bounding faces, and the associated set of displacements and stress nodes are also shown. Projecting forces on the z axis and rearranging terms the following equation is obtained:

$$\frac{\sigma_z^c - \sigma_z^d}{\lambda_z} + 4\,\frac{\tau_{rz}^a}{\lambda_r} = 0 \tag{4.2}$$

New strain-displacement relationships need to be adopted for a stress node located on the axis. Considering stress node c in Fig. 14(b):

$$\epsilon_r^c = 2\frac{u_{2j}}{\lambda_r} \tag{4.3}$$

$$\epsilon_\theta^c = \epsilon_r^c \tag{4.4}$$

$$\gamma_{rz}^c = 0 \tag{4.5}$$

Equation 4.3 is developed by stipulating that the radial displacement of the node to the left of the axis is equal in magnitude to displacement u_{2j} and opposite in sign.

Equation 4.4 simply states that when r approaches zero, the tangential strain is equal to the radial strain. This relation is readily proved by investigating the limit, as r goes to zero, of the strain displacement relations.

$$\epsilon_r = \frac{\partial u}{\partial r}$$

$$\epsilon_\theta = \frac{u}{r}$$

As r goes to zero,

$$\epsilon_\theta = \lim_{r \to 0} \left(\frac{u}{r}\right)$$

$$\epsilon_\theta = \lim_{r \to 0} \left(\frac{\partial u/\partial r}{\partial r/\partial r}\right)$$

$$\epsilon_\theta = \frac{\partial u}{\partial r}$$

The shear strain is zero at the axis of symmetry. The general equation for the longitudinal strain does not require reformulation.

4.3. Nodes at Mid-Height of the Vessel

A typical mass node at the roller support, simulating the symmetry conditions at mid-height of the vessel, is represented in Fig. 15 by its grid equivalent.

At the stress node in position d, which is the mirror image of stress node point c, the shear stress is equal in magnitude and opposite in sign to that at c, i.e., $\tau_{rz}^{d} = -\tau_{rz}^{c}$. If this condition is introduced into Eq. 2.6, the equilibrium equation in the radial direction for a typical node at the support is obtained,

$$\frac{\sigma_r^a - \sigma_r^b}{\lambda_r} + 2\,\frac{\tau_{rz}^c}{\lambda_z} + \frac{\frac{1}{2}\,(\sigma_r^a + \sigma_r^b) - \sigma_\theta^{ij}}{r_i} = 0 \qquad (4.6)$$

The longitudinal displacement of a mass node at this fictitious support, used for the line of symmetry, is necessarily equal to zero. This condition replaces the regular z equation,

$$w_{il} = 0 \qquad (4.7)$$

Only the strain-displacement relationship in the z direction needs to be reformulated at the mid-height of the vessel. From symmetry considerations at stress node a:

$$\epsilon_z^a = 2\,\frac{w_{i2}}{\lambda_z} \qquad (4.8)$$

4.4. Nodes on the Loaded Surfaces

The case of a mass element on the exterior surface of the side wall is presented to illustrate the salient points in the development of the equations for a node on a loaded surface. Nodes on the other loaded surfaces would be similarly generated. Figure 16 illustrates the grid arrangement surrounding a mass node on the outside wall.

The equilibrium equation in the z direction, obtained by isolating the mass element and projecting the forces on its faces on the z axis, is:

$$\frac{\sigma_z^c - \sigma_z^d}{\lambda_z}\left(1 - \frac{\lambda_r}{4r_i}\right) - 2\frac{\tau_{rz}^b}{\lambda_r} + \frac{\tau_{rz}^b}{r_i} = 0 \qquad (4.9)$$

There is a close correspondence between the terms in this equation and those in the equilibrium equation for the typical mass node. The σ_z term is multiplied by the factor $(1-\lambda_r/4r_i)$ to correct for the special shape of the mass element. As for the shear terms, the first one can be rationalized by observing that the shear stress at the exterior surface is zero, and since the element width is $\lambda_r/2$, $\lambda_r/2$ should be used as the discrete interval in the finite difference equivalent of $\frac{\partial \tau_{rz}}{\partial r}$. The third term, τ_{rz}^b, is taken to represent the shear stress at the center of the mass element.

The equation in the r direction can be obtained from a typical r direction equilibrium equation, Eq. 2.6, by observing that, at the exterior surface of the wall, the shear stresses τ_{rz}^c and τ_{rz}^d are equal to zero and that the discrete interval along the r axis is $\lambda_r/2$.

Incorporating these conditions in the equation and substituting the circumferential prestressing equivalent pressure σ_{cp} for σ_r^a, the new equation of equilibrium in the radial direction becomes:

$$-2\frac{\sigma_{cp} + \sigma_r^b}{\lambda_r} + \frac{\sigma_r^b - \sigma_\theta^{ij}}{r_i} = 0 \tag{4.10}$$

The radial and tangential strains at stress nodes c and d cannot be expressed directly in terms of the general strain-displacement relationships. Instead, the boundary condition that the stresses at c and d equal the applied external pressure is used,

$$\sigma_r^c = \sigma_{cp} \tag{4.11}$$

From the stress-strain law:

$$\sigma_r^c = C_{11}\epsilon_r^c + C_{12}\epsilon_z^c + C_{13}\epsilon_\theta^c + C_{14}\gamma_{rz}^c \tag{4.12}$$

where the extensional coefficients C_{11} through C_{14} are evaluated according to the provisions given in Chapter III. The general strain-displacement relations for ϵ_r^c and ϵ_θ^c ,

$$\epsilon_r^c = \frac{u_{i+1j+1} - u_{i-1j+1}}{\lambda_r} \tag{4.13}$$

$$\epsilon_\theta^c = \frac{u_{i+1j+1} + u_{i-1j+1}}{2r_i} \tag{4.14}$$

suggest the utilization of a ficticious displacement node one half a

space from the wall. Substituting Eqs. 4.16 and 4.15 in Eq. 4.14, the fictitious radial displacement u_{i+1j+1} is obtained.

A similar approach is followed for nodes on the other loaded and free surfaces of the vessel.

4.5. Node at Re-entrant Corner

Either a mass node or a deformable node can be placed at the re-entrant corner. Each of the two alternatives have advantages and disadvantages depending on how far the analysis of the vessel is to proceed. Since each of the nodal placements is useful, under different circumstances, both are discussed below.

A mass or displacement node at the re-entrant corner eliminates the need to define the "average" strain and stress tensors at this location. Since the discontinuity at the corner induces highly concentrated stresses, average stresses and strains do not closely represent the physical reality of this location. The average values one half space from the corner give a more realistic estimate of the stress and strain states in the neighboring region. This arrangement is the most convenient for elastic analysis.

When proceeding beyond the elastic range, there is a high probability that because of the stress concentration at the re-entrant corner, the first crack will initiate there. The model is such that cracks can only take place at stress nodes. For this reason, it is necessary, or at the least extremely desirable, to have a stress node at the re-entrant corner when analyzing inelastic behavior. The stresses and strains measured at the re-entrant corner are, with this

arrangement, smaller than the true values since they represent averages over the associated areas.

Figure 17 shows the grid node arrangement around the re-entrant corner. The strain-displacement relations at the corner need not be reformulated. However, some of the equilibrium equations for the neighboring mass elements are affected.

If the radial direction equilibrium equation for mass node 3 is taken as an example, it can be seen that a special situation develops at the face containing stress node b. The typical equilibrium equation in the r direction,

$$\frac{\sigma_r^a - \sigma_r^b}{\lambda_r} + \frac{\tau_{rz}^c - \tau_{rz}^d}{\lambda_z} + \frac{\frac{1}{2}(\sigma_r^a + \sigma_r^b) - \sigma_\theta^{ij}}{r_i} = 0 \qquad (4.15)$$

can still be used provided σ_r^b is redefined, in such a way that the resulting force at face b equals the sum of the resultants of the applied internal pressure p and the stress at b, integrated over the associated areas. In this case, this condition means that σ_r^b, in the preceeding equation, needs to be replaced by:

$$\bar{\sigma}_r^b = \frac{1}{2}(p + \sigma_r^b) \qquad (4.16)$$

because p and σ_r^b each act on half of the face area of node b.

The equilibrium equation in the z direction at mass node 2 is derived in a similar manner.

V. COMPUTATIONAL TECHNIQUE

5.1. The Numerical Problem

The numerical method, used in this study, is based on a discrete model which has been shown to be mathematically consistent with the continuum. This model reduces the continuum to a system which is completely defined by a finite number of variables. The formulation of the problem is obtained directly from the fundamental principles of mechanics and basic behavior of materials. Such a formulation leads to a system of linear algebraic equations which are intuitively meaningful. The solution of such a system of equations can be conveniently obtained by the use of digital computers.

The IBM 360-50/75 system operated by the Department of Computer Science of the University of Illinois has been used both in generating and solving the discrete equations of equilibrium.

Before going into specifics on the utilization of this method, a brief general description of the procedure is given.

5.2. Computational Procedure

Since the full range of vessel behavior includes a nonlinear phase, the solution of the problem is carried out incrementally, in a piecewise linear fashion. This permits a re-evaluation of the stiffness coefficients and load terms each time the discrete system representing the continuum is modified. It becomes necessary to regenerate some of the governing equations when localized cracking is initiated, or when the loading is incremented. Each equilibrium equation is expressed in

terms of displacements, by a sequential substitution of stress-strain and stress-displacement relationships into the original equation.

Concrete at a deformable node is considered to have cracked if the average tensile strain in any direction at that node has reached a certain limiting value. The formation of a crack is followed by a re-evaluation of the stiffness coefficients of the discrete system, in such a way that the material at the cracked node exhibits orthotropical properties consistent with no tensile resistance in a direction perpendicular to the crack.

After the crack has been introduced the energy released from the node at cracking is redistributed throughout the network in order to re-establish the equilibrium of the system. A close surveillance of the strain condition, at the deformable nodes, is kept so that new nodes that may in turn crack as a consequence of previous cracking can be treated in a similar manner before proceeding. This repetitive process is continued until the crack ceases to propagate without increase in load. Once the crack is arrested, the internal pressure is increased until a new node reaches the limiting value assumed as the cracking strain criterion.

5.3. Solution of the Equations

As indicated above, the resulting system of algebraic equilibrium equations in u and w displacements are equivalent to the finite difference discretization of the partial differential equations governing the continuum.

These differential equations can be reduced to two independent, second order, linear, partial differential equations of the elliptic type in u and w. This being the case, and knowing that the exact boundary-value problem possesses a solution, the approximate discrete problem produces results that, as the grid is continually refined, tend to the exact solution.[8,12]

In matrix form, the system of algebraic equations is expressed by:

$$[M]\{d\} = \{P\} \tag{5.1}$$

where {d} is the displacement vector; [M] the coefficient matrix formed by the equilibrium equations, and {P} is the vector corresponding to the load terms.

In expanded form:

$$\begin{bmatrix} \ddots & & \\ & & \\ & & \ddots \end{bmatrix} \begin{Bmatrix} u_1 \\ w_1 \\ u_2 \\ w_2 \\ \vdots \\ u_k \\ w_k \\ \vdots \\ u_n \\ w_n \end{Bmatrix} = \begin{Bmatrix} P_{r1} \\ P_{z1} \\ \vdots \\ P_{rk} \\ P_{zk} \\ \vdots \\ P_{rn} \\ P_{zn} \end{Bmatrix} \tag{5.2}$$

where the subscript on the displacements represents the sequential order of the displacement nodes, n is the number of displacement nodes in the grid, and P_{rk} and P_{zk} are the load terms in the equations for the mass node of location k.

Since only a few displacements, defined at the displacement nodes surrounding the element, are present in each one of the equations, Matrix [M] is a tightly banded matrix. With the L-shaped geometry of the cross section of the vessel, the minimum band width is achieved by employing a diagonal numbering system as opposed to column or row numbering. This reduction decreases considerably the space required for the solution of the equations in the computer. Because the coefficients along the diagonal are dominant, the Gauss-Seidel method of solution is used with advantage.

5.4. Extrapolation to Crack Occurrence

As discussed in Chapter III, two basic types of cracks, radial and conical, can occur in the vessel. The occurrence of cracking is initiated when a principal strain exceeds the cracking criterion.

The condition of axi-symmetry, which results in $\gamma_{r\theta}$ and $\gamma_{\theta z}$ being identically zero, establishes ϵ_θ as one of the principal strains. The other principal strains are obtained from the direct and shear strains in plane rz. The maximum principal strain in plane rz is:

$$\epsilon_1 = \frac{1}{2}\left[\epsilon_r + \epsilon_z + \sqrt{(\epsilon_r-\epsilon_z)^2 + \gamma_{rz}^2}\right] \qquad (5.3)$$

The two strains, ϵ_θ and ϵ_1, indicate whether a stress node is in an elastic or a cracked condition.

After a crack has formed at the location of a stress node, the related stiffness coefficients need to be changed to reflect the presence of the crack.

In order to advance from a certain loading stage to the initiation of a new crack, it is necessary to determine the internal pressure level at which this new crack develops. Let ϵ_r^{pr}, ϵ_z^{pr}, ϵ_θ^{pr} and γ_{rz}^{pr} refer to the strain state at the conclusion of all previous cracking and prior to the new pressure increment and $\Delta\epsilon_r$, $\Delta\epsilon_z$, $\Delta\epsilon_\theta$ $\Delta\gamma_{rz}$ indicate the strain increments caused by an increase Δp of the internal pressure. The elastic strains at the moment of cracking are:

$$\begin{aligned}
\epsilon_r^{cr} &= \epsilon_r^{pr} + F\,\Delta\epsilon_r \\
\epsilon_z^{cr} &= \epsilon_z^{pr} + F\,\Delta\epsilon_z \\
\epsilon_\theta^{cr} &= \epsilon_\theta^{pr} + F\,\Delta\epsilon_\theta \\
\gamma_{rz}^{cr} &= \gamma_{rz}^{pr} + F\,\Delta\gamma_{rz}
\end{aligned} \tag{5.4}$$

where F is the factor that scales the pressure increment Δp to the level that will cause the next crack to form.

If the crack is radial, the cracking condition is:

$$\epsilon_\theta^{cr} = \epsilon_{cr} \tag{5.5}$$

where ϵ_{cr} is the strain value selected as the cracking criterion. In this case F, as found from Eq. 5.5, is given by:

$$F = \frac{\epsilon_{cr} - \epsilon_{\vartheta}^{pr}}{\Delta\epsilon_{\theta}}$$

On the other hand, if the crack is conical, ϵ_1 is equated to ϵ_{cr} and the following second degree equation in F is obtained:

$$\epsilon_{cr} = \frac{1}{2}\left[(\epsilon_r^{pr} + \epsilon_z^{pr}) + F(\Delta\epsilon_r + \Delta\epsilon_z) + \sqrt{\{(\epsilon_r^{pr} - \epsilon_z^{pr})^2 + F(\Delta\epsilon_r - \Delta\epsilon_z)\}^2 + (\gamma_{rz}^{pr} + F\,\Delta\gamma_{rz})^2}\right] \tag{5.6}$$

The roots from this equation are evaluated according to the particular strain situation existing at the node being investigated.

Scaling factors F are computed at all the stress nodes in the network that remain in elastic condition in either one or both of the principal directions in which the node can crack. The lowest F value corresponds to the initiation of the next crack.

5.5. Crack Propagation

The formation of a crack is accompanied by a local release of elastic energy. The energy is absorbed by the rest of the continuum through a natural process of redistribution of stresses and strains.

This natural process is simulated in the model by reanalyzing the modified discrete system that includes the new crack. Once the balance of energy is re-established, it is necessary to review the strain state throughout the vessel. If additional cracking is in evidence, i.e., if the crack has propagated without an increase in

loading the artificial redistribution process is repeated. This procedure is continued until the crack ceases to propagate.

In the early stages of loading, crack propagation is not likely to occur. The load is increased incrementally from the formation of one crack to the next. But, when cracking has become wide spread, a succession of cracks forms nearly every time the internal pressure is increased.

VI. NUMERICAL RESULTS

6.1. General Remarks

A sample problem chosen to demonstrate the applicability of the lumped parameter model is presented and discussed in this chapter. This sample problem corresponds to one of the small-scale vessels tested at the Structural Laboratory of the University of Illinois. The analytical results obtained here are compared with the experimental data.

Four stages of loading have been selected to illustrate the behavior of the sample vessel throughout the loading process. They correspond to: (a) prestressing alone (zero internal pressure), (b) the state just prior to the formation of the first crack, (c) an intermediate stage in the inelastic range and (d) the load level at the time the analysis was terminated. The case of the unprestressed vessel subjected to internal pressure is also included and presented for reference.

6.2. The Sample Problem

The dimensions, prestressing conditions, and material properties assumed for the sample problem were chosen to correspond to the dimensions and properties of one of the vessels tested at the University of Illinois. The vessel's external diameter, D, is 3 ft. 4 in. and its total height, H, is 6 ft. 8 in. The slab has a depth, t_s, of 9 inches. The cylinder has a wall thickness, t_c, of 5 inches.

The vessel is prestressed longitudinally by 30 high-strength steel ungrouted cables, 0.151 sq. in. in cross-sectional area, loaded

initially with 25.2 kips each. These ungrouted prestressing cables are placed at a distance of 3 in. from the outside surface of the wall. The circumferential prestressing is provided by a single cable with a cross-sectional area of 0.029 sq. in. The cable is helically wrapped around the cylindrical body at a spacing of 0.333 in.

The elastic constants for the materials have been determined experimentally. The Young's modulus and Poisson's ratio of the concrete are $E_c = 4.3 \times 10^6$ psi and $\nu = 0.15$, and the Young's modulus of the steel is $E_{st} = 28 \times 10^6$. There is a scarcity of information pertinent to the cracking strain of concrete under multiaxial states of stress. The value adopted for the cracking strain criterion, $\epsilon_{cr} = 0.00015$, was selected on the basis of the strains measured during the test of the small scale vessel.

A 6 x 41 grid is used to represent the cylindrical wall, while a 9 x 16 grid is employed to approximate the slab. Since the analysis is continued until a substantial portion of the vessel is in cracked state, the grid layout was selected to place a stress node at the re-entrant corner.

6.3. Behavior of the Vessel

The significant behavior of the pressure vessel, its ductility, is best discussed with the aid of a load-displacement diagram, Fig. 18. This figure shows the relationship of the longitudinal displacement at the center of the slab versus pressure. The center displacement is measured on the upper face of the slab at the axis of symmetry. The displacements shown are measured from the vessel already deformed by

the prestressing forces. That is, the origin represents the case of a fully prestressed vessel under zero internal pressure. The rationale for this choice is that the experimental tests have the fully pre-stressed vessel as their origin.

The vessel behaves linearly as the internal pressure is increased from 0 to 450 psi. Point B identifies the formation of the first crack as detected in the lumped parameter model. The first crack is a conical crack at the re-entrant corner. Since the stresses at the re-entrant corner of the vessel are highly concentrated while the stresses and strains that the model computes are average values, it is clear that in the actual vessel this corner crack is initiated slightly earlier in the loading process. Because the stiffness loss due to an incipient crack at the re-entrant corner is very small, the analytical and experimental results appear in perfect agreement at this point.

From point B on, new cracks form in succession as the internal pressure is increased. Associated with the spreading of cracking the general stiffness of the vessel decreases and the straight line that characterizes elastic behavior transforms into a curve of decreasing slope.

The analytical broken line extending from B to D is composed of slanted and horizontal segments. A slanted segment corresponds to the linear behavior of the modified network nodal system which includes all those cracks that have formed up to that time. This linear behavior prevails until a new crack forms. When the new crack is incorporated and the energy released is redistributed into the system a larger deformation corresponds to the same load level. The line joining the

points that represent the deformations of the system just before and just after the new crack is, then, horizontal. This horizontal line becomes automatically extended when additional new cracks are formed solely as a consequence of the energy released from the last node to crack.

This terrace pattern is obviously due to the finite piece-wise approach to the problem of cracking. The heavy line traced from B to D provides an approximation to the continuous behavior of the structure.

A dashed line has been traced through the experimental data points plotted. A comparison between the analytical and experimental results reveals that although there is excellent agreement in the elastic and early inelastic zones, the analytical curve departs from the experimental curve as cracking progresses. The small discrepancy is in part the product of the selection of the cracking criterion. Conceivably, the two curves can be brought into near coincidence by adjusting the cracking criterion to a slightly higher value. Nevertheless, the similarity between the slopes of these two curves is highly significant in assessing the usefulness and potentials of the method of analysis.

Figure 19 provides a comparison between the longitudinal displacements computed across the upper face of the slab for three levels of loading and the corresponding experimental values. At $p = 450$ psi, when the first crack develops, there is a perfect agreement at the center; little can be said about the rest of the values because of the limitations of the experimental equipment when dealing with very

small deformations. A much better general agreement can be observed between the other two pairs of curves. Because of the uncertainty in the cracking criterion adopted the analytical values for p = 580 psi and p = 666 psi are compared to the "equivalent" experimental results for p = 600 psi and p = 700 psi.

Figures 20 through 22 illustrate the state of stress that would be caused by the application of internal pressure to an unprestressed vessel. For this purpose, the material is considered to behave elastically. Figure 20 shows the radial stresses prevailing at the levels of the upper and lower faces of the slab. Similarly, the longitudinal stresses along the external and internal surfaces of the cylinder are presented in Fig. 22. The circumferential stresses in both the slab and the cylinder are given in Fig. 21. The concentration of high tensile stresses and strains at the re-entrant corner is clearly visible in all the figures. Other regions of interest are the central portions of the slab, both near the upper and the lower surfaces. In the upper region, tensile stresses prevail in the radial and circumferential directions. The compressive stresses in the lower region, that result from bending of the slab, are greatly increased when the vessel is subjected to the compression field produced by the prestressing systems.

As mentioned above, the first crack is formed at the re-entrant corner. Figures 23 through 27 illustrate the state of stresses and strains that determine the initiation of such a crack. Especially significant are the maximum strain trajectories in rz plane.

The cracks that develop after the corner crack are mainly radial. Some conical cracks naturally form in the neighborhood of the axis of symmetry. All this subsequent cracking occurs in the central upper region of the slab. As the load increases, the radial cracks extend rather quickly toward the outside of the cylinder, and more slowly downward from the upper face of the slab. After the radial cracking in the upper region of the slab has become widespread, the crack at the re-entrant corner propagates toward the outside of the wall. This conical crack, which initiates at approximately 45° from the horizontal, flattens out slowly as it progresses toward the longitudinal prestressing cables. Figures 28 through 33 characterize the vessel at this cracking stage. Figure 33, in particular, describes graphically the extent and nature of cracking. Since the radial cracks have propagated from the axis of symmetry all the way to the external surface of the cylinder, the circumferential stresses at the upper surface of the slab are zero. This is shown in Fig. 29.

If the pressure continues to be increased, the radial cracks continue propagating downward toward the bottom of the slab. The conical crack at the re-entrant corner, after crossing the longitudinal prestressing tendon, changes to a negative slope and continues to develop toward the external surface of the wall. The analysis is terminated when the failure mechanism appears clearly defined. For the sample vessel under study, this occurs at $p = 670$ psi. Figures 34 through 37 illustrate the stress and strain states at the stage when the analysis was stopped. Since cracking is general throughout better than the upper 60 percent of the slab and the crack at the re-entrant corner

separates the wall from the slab, the load is being carried primarily by an inverted highly compressed dome supported essentially by the longitudinal prestressing cables at the distribution plates. This situation is depicted quite clearly by the various figures that characterize this loading state.

The final failure mechanism can be readily identified from the analysis of the state of cracking illustrated by Fig. 37. As the crack initiated at the re-entrant corner propagates toward the outside of the wall, the amount of rotational constraint of the slab decreases. The slab finally fails in bending as a simply supported circular concrete plate. Pie-shaped sectors open up when the radial cracks reach the bottom of the slab. These sectors rotate about the crack across the wall.

VII. CONCLUSIONS AND RECOMMENDATIONS FOR FURTHER STUDY

A discrete element method for the elastic and inelastic analysis of cylindrical prestressed concrete reactor vessels has been developed. This method utilizes a lumped parameter model based on the theory of finite differences. The model provides good estimates of the displacements, stresses and strains that result throughout the body of the vessel at the various stages in loading, beginning with the prestressing and continuing to near final failure of the vessel.

The results obtained from the analysis indicate that an elastic-fracture approach to the inelastic properties of concrete is sufficient to predict the mode of failure of a cylindrical prestressed concrete pressure vessel with flat ends. Although considerations of plasticity can in principle be included, there is evidence that by so doing no major gain is obtained in describing the behavior of the vessel. For the sake of completeness, it is desirable to incorporate a general failure theory of concrete at the appropriate time in the future when such a theory has been developed.

This lumped parameter method can be employed to determine which mode of failure results for a vessel with a given combination of parameters, general dimensions and prestress. From this view point, the method is an invaluable tool for the design of PCRV's, where a ductile mode of failure is required.

The analytical results obtained by the use of the method compare favorably with experimental results obtained from tests on small-scale vessels at the University of Illinois.

The lumped parameter study presented here represents in effect the equivalent to an experimental test of the vessel. When interacted with the actual experimental study the combination provides a much clearer explanation of the actual behavior of the vessel.

Pressure vessels with openings can be investigated by means of a three-dimensional discrete model. The lumped parameter model used here is implicitly a three-dimensional system. With the conditions of axi-symmetry present in the problem it was possible to reduce the model to a two-dimensional network. Although a major programming effort would be involved in employing the model in its three-dimensional form, the basic approach employed here does not need to be altered in order to make such an extension.

The effect of thermal gradients across the walls of a vessel is an important problem that can be investigated in connection with nuclear reactor technology.

As investigations develop the behavior of concrete under a multiaxial state of stress, their results should be incorporated in the analysis of PCRV's. There is a particularly urgent need for information pertaining to the cracking of concrete under biaxial and triaxial states of stress. Until such investigations are conducted, the influence of various assumptions on concrete behavior can be studied with the model. From this study, it can be determined how sophisticated a failure theory need to be to provide an accurate approximation to the behavior of prestressed concrete pressure vessels.

LIST OF REFERENCES

1. Ang, A. H. S. and Rainer, J. H., "Model for Wave Propagation in Axi-Symmetric Solids," Journal of the Engineering Mechanics Division, ASCE, Vol. 90, No. EM2, April 1964.

2. Bresler, B. and Pister, K. S., "Strength of Concrete Under Combined Stresses," Proceedings of the American Concrete Institute, Vol. 55, No. 3, September 1958.

3. Brown, A. H. et al., "The Design and Construction of Prestressed Concrete Pressure Vessels with Particular Reference to Oldbury Nuclear Power Station," Proceedings of the Third International Conference on the Peaceful Uses of Atomic Energy, Geneva, Vol. 8, United Nations, New York, 1964.

4. Chang, G. C., "Interaction of Plane Stress Waves with Lined or Unlined Tunnels in Elastic-Perfectly Plastic Media," Ph.D. Thesis, University of Illinois, 1966.

5. Chinn, J. and Zimmerman, R. M., "Behavior of Plain Concrete Under Various High Triaxial Compression Loading Conditions," Technical Report No. WL TR 64-163, Air Force Weapons Laboratory, Kirtland Air Force Base, New Mexico.

6. Crose, J. G. and Ang, A. H. S., "A Large Deflection Analysis Method for Elastic-Perfectly Plastic Plates," Civil Engineering Studies, Structural Research Series No. 323, University of Illinois, June 1967.

7. Fedorkiw, J. P., "Analysis of Reinforced Concrete Frames with Filler Walls," Ph.D. Thesis, University of Illinois, 1968.

8. Forsythe, G. E. and Wasow, W. R., "Finite Difference Methods for Partial Differential Equations," John Wiley and Sons, New York, 1960.

9. Gamble, W. L., et al, "A Study of Launch Facility Closures," SAMSO-TR-67-15, U.S.Air Force Contract No. AF04(694)-796, University of Illinois, November 1967.

10. Gaus, M. P., "A Numerical Solution for the Transient Strain Distribution in a Rectangular Plate with a Propagating Crack," Civil Engineering Studies, Structural Research Series No. 182, September 1959.

11. Harper, G. N. and Ang, A. H. S., "A Numerical Procedure for the Analysis of Contained Flow Problems," Civil Engineering Studies, Structural Research Series No. 266, University of Illinois, June 1963.

12. Hildebrandt, F. B., Methods of Applied Mathematics, 4th ed., Prentice Hall, New Jersey, 1958.

13. Marsh, R. O. and Rockenhauser, W., "Prestressed Concrete Structures for Large Power Reactors," Mechanical Engineering, ASME, Vol. 88, No. 7, July 1966.

14. Martinez-Marquez, A., "General Theory for Thick Shell Analysis," Journal of the Engineering Mechanics Division, ASCE, Vol. 92, No. EM2, December 1966.

15. Mohraz, B. and Schnobrich, W. C., "The Analysis of Shallow Shells by a Discrete Element System," Civil Engineering Studies, Structural Research Series No. 304, University of Illinois, March 1966.

16. Newman, K., "Criteria for the Behavior of Plain Concrete Under Complex State of Stress," International Conference on the Structure of Concrete, Paper F1, September 1965.

17. Otter, J. R. H., Cassell, A. C. and Hobbs, R. E., "Dynamic Relaxation," Proceedings of the Institution of Civil Engineers, Vol. 35, December 1966.

18. Otter, J. R. H., "Computations for Prestressed Concrete Reactor Pressure Vessels Using Dynamic Relaxation," Nuclear Structural Engineering, Vol. 1, No. 1, 1965.

19. Rashid, Y. R., "Analysis of Asymmetric Composite Structures by the Finite Element Method," Short Course on Prestressed Concrete Nuclear Reactor Structures, Engineering Extension and the College of Engineering, University of California, Berkeley, March 1968.

20. Rashid, Y. R. and Rockenhauser, W., "Pressure Vessel Analysis by Finite Element Techniques," United States Report GA-7810, General Atomic, February 1967.

21. Richart, F. E., Brandtzaeg, A. and Brown, R. L., "A Study of the Failure Mechanism of Concrete Under Combined Stresses," Civil Engineering Studies, Structural Research Series No. 185, 1928.

22. Schnobrich, W. C., "A Physical Analogue for the Analysis of Cylindrical Shells," Ph.D. Thesis, University of Illinois, 1962.

23. Shoeb, N. A. and Schnobrich, W. C., "The Analysis of Elasto-Plastic Shell Structures," Civil Engineering Studies, Structural Research Series No. 324, University of Illinois, August 1967.

24. Tan, P. T., "Prestressed Concrete in Nuclear Pressure Vessels: A Critical Review of Current Literature," ORNL-4227, Oak Ridge National Laboratory, U. S. Atomic Energy Commission, May 1968.

25. Timoshenko, S. and Goodier, J. N., Theory of Elasticity, 2nd ed., McGraw-Hill Co., New York, 1951.

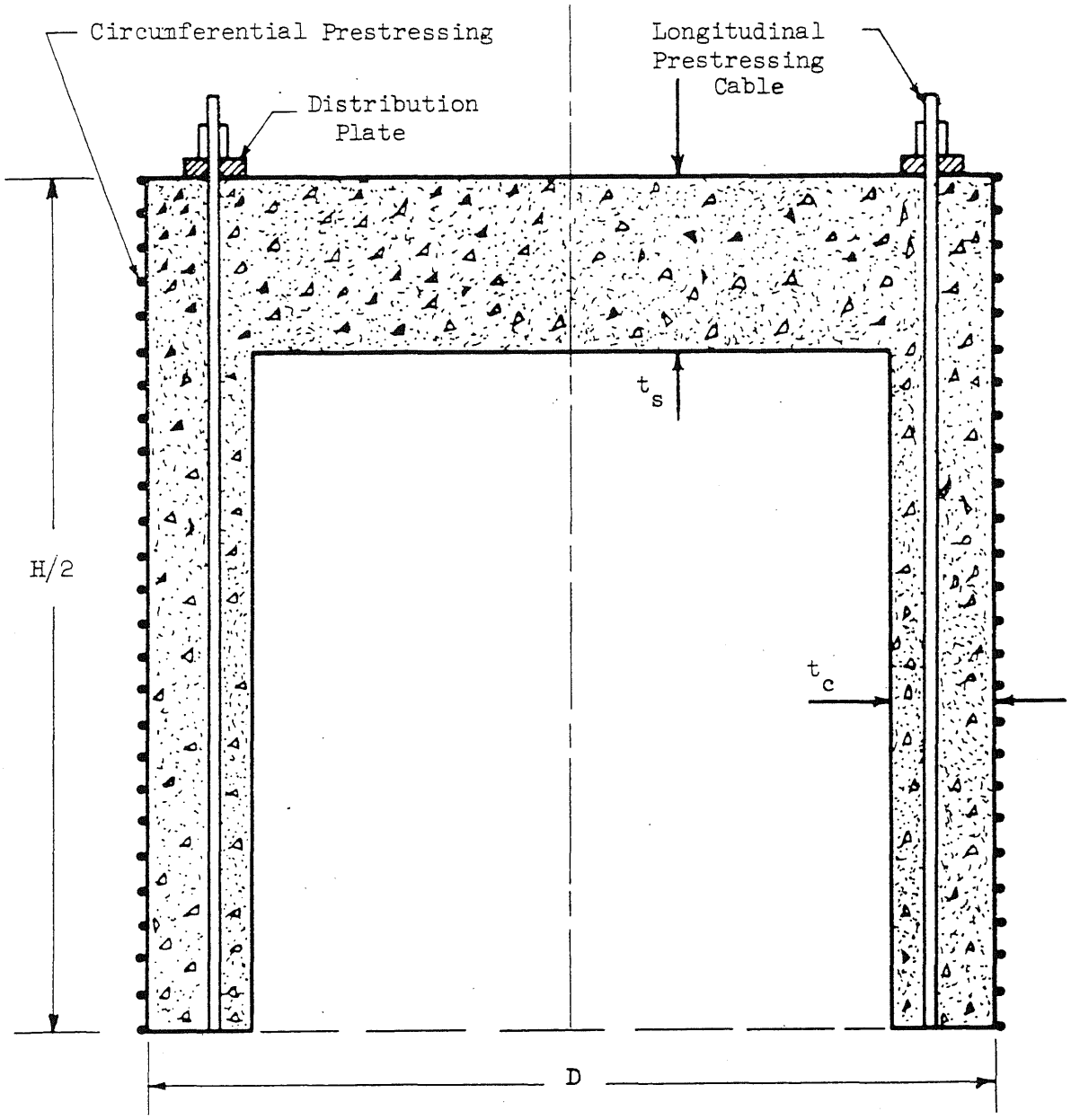

FIG. 1. LONGITUDINAL SECTION THROUGH HALF OF THE VESSEL

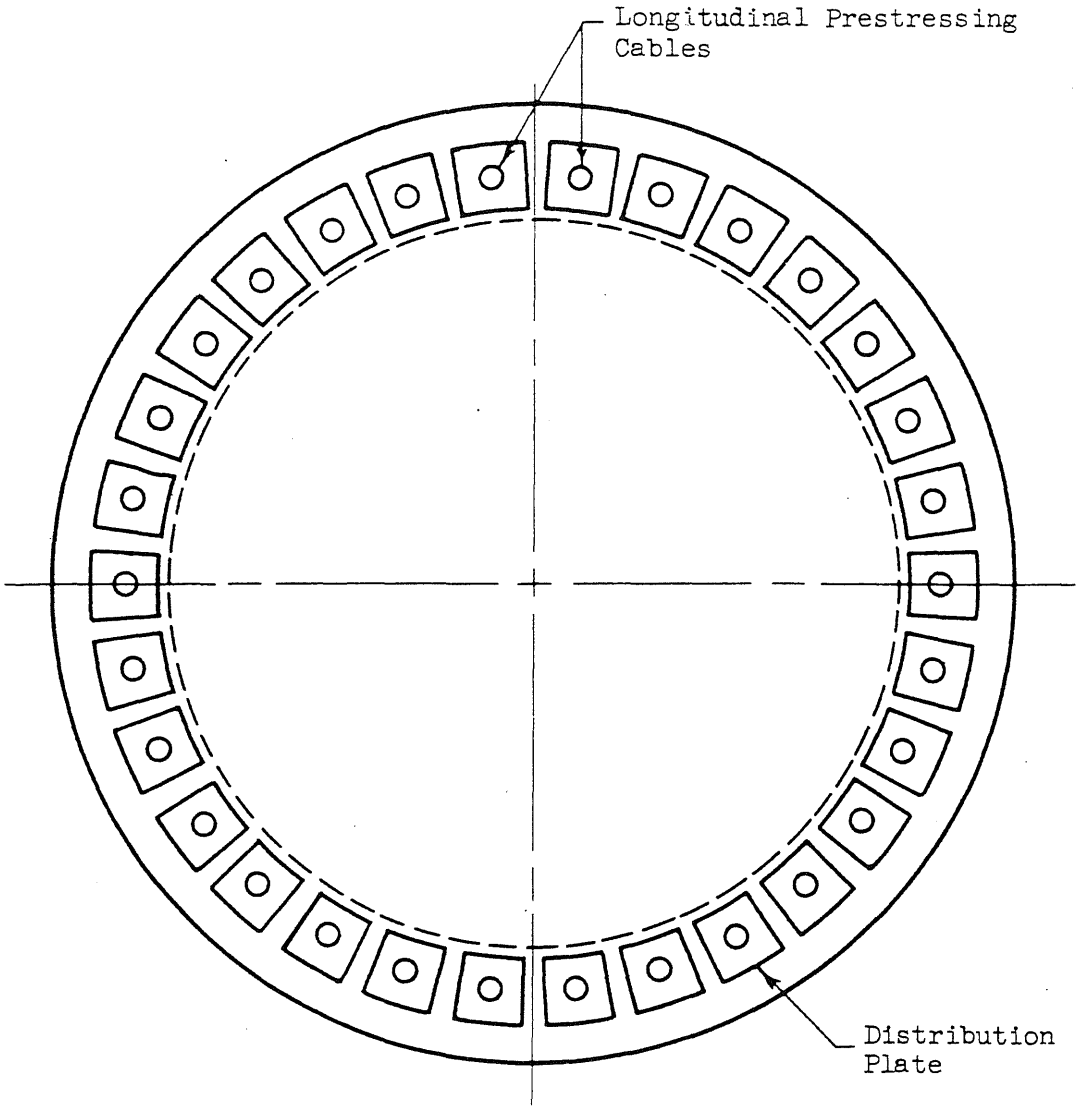

FIG. 2. PLAN VIEW OF END SLAB

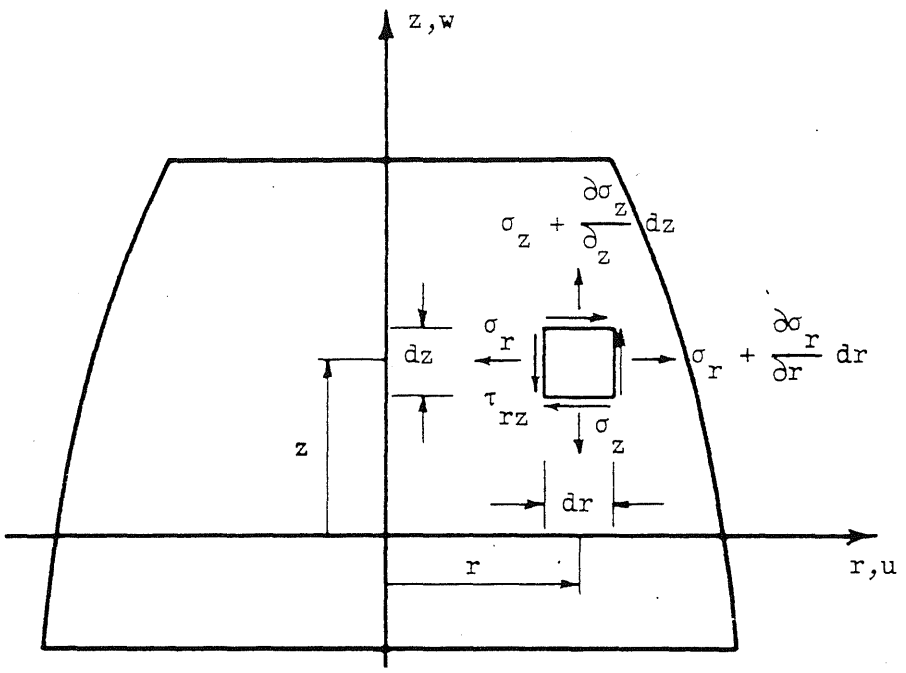

a. Longitudinal Cross Section

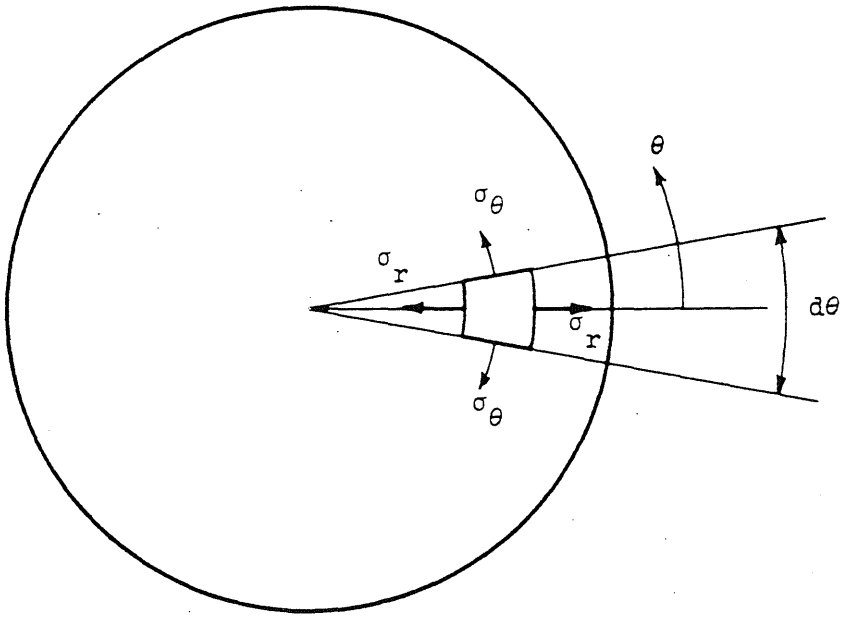

b. Horizontal Cross Section

FIG. 3. AXIALLY SYMMETRIC BODY

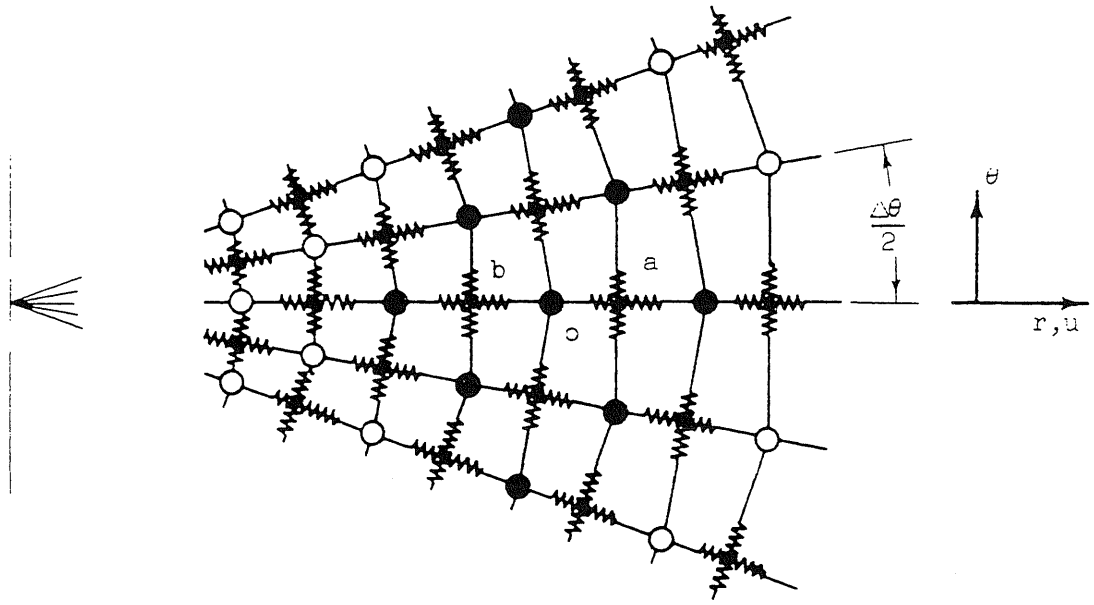

a. Plan View

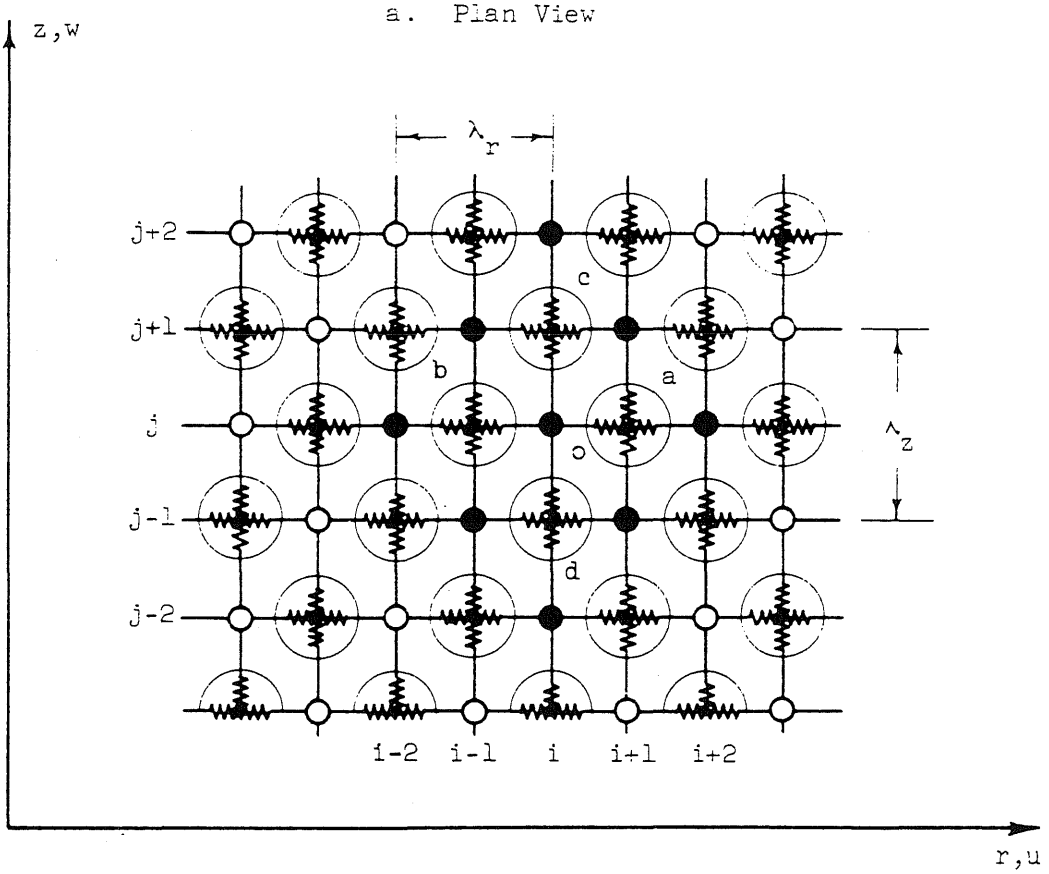

b. Radial Section ($\theta=0^{\circ}$)

FIG. 4. THE LUMPED PARAMETER MODEL

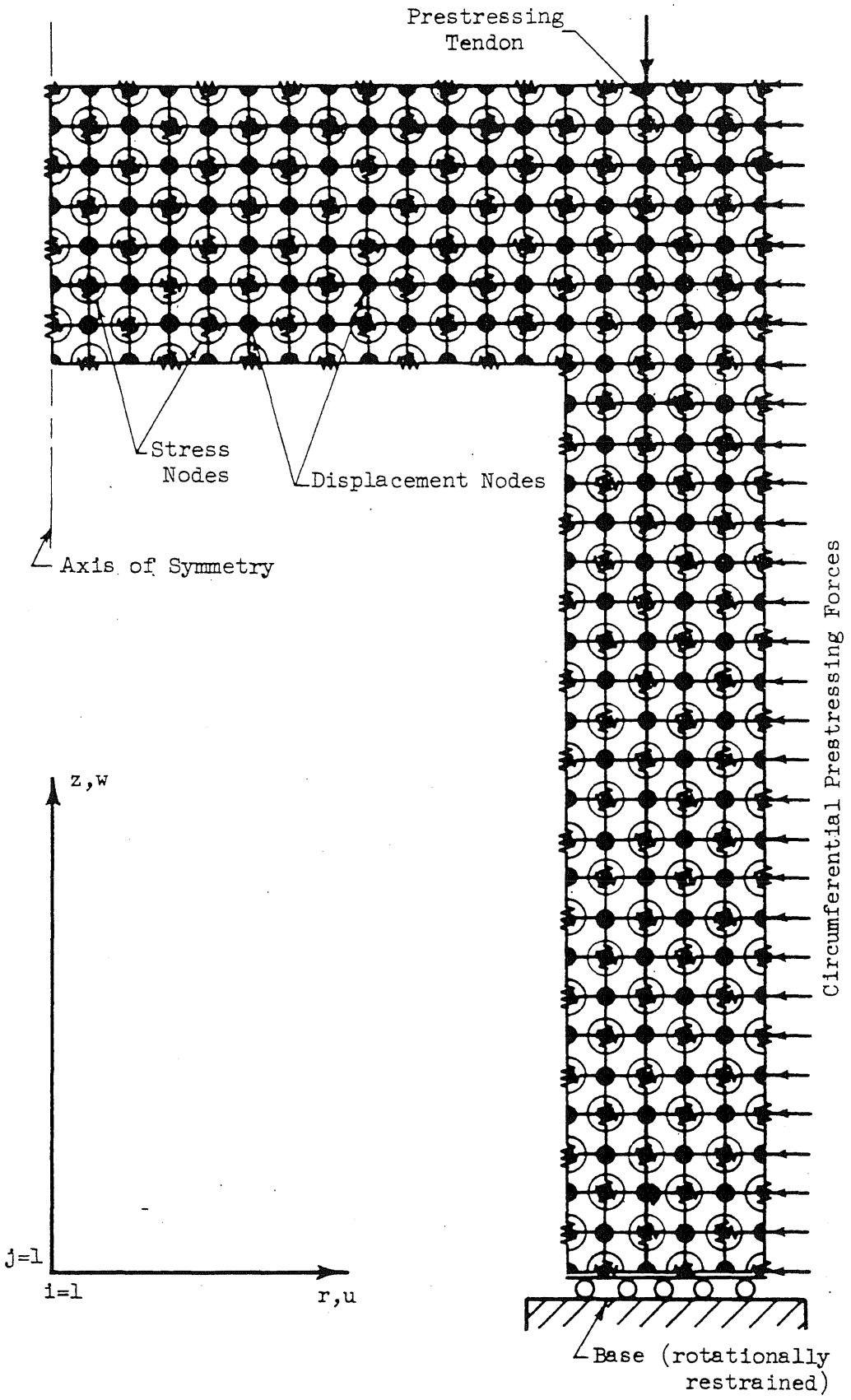

FIG. 5. LUMPED PARAMETER REPRESENTATION OF THE PRESSURE VESSEL

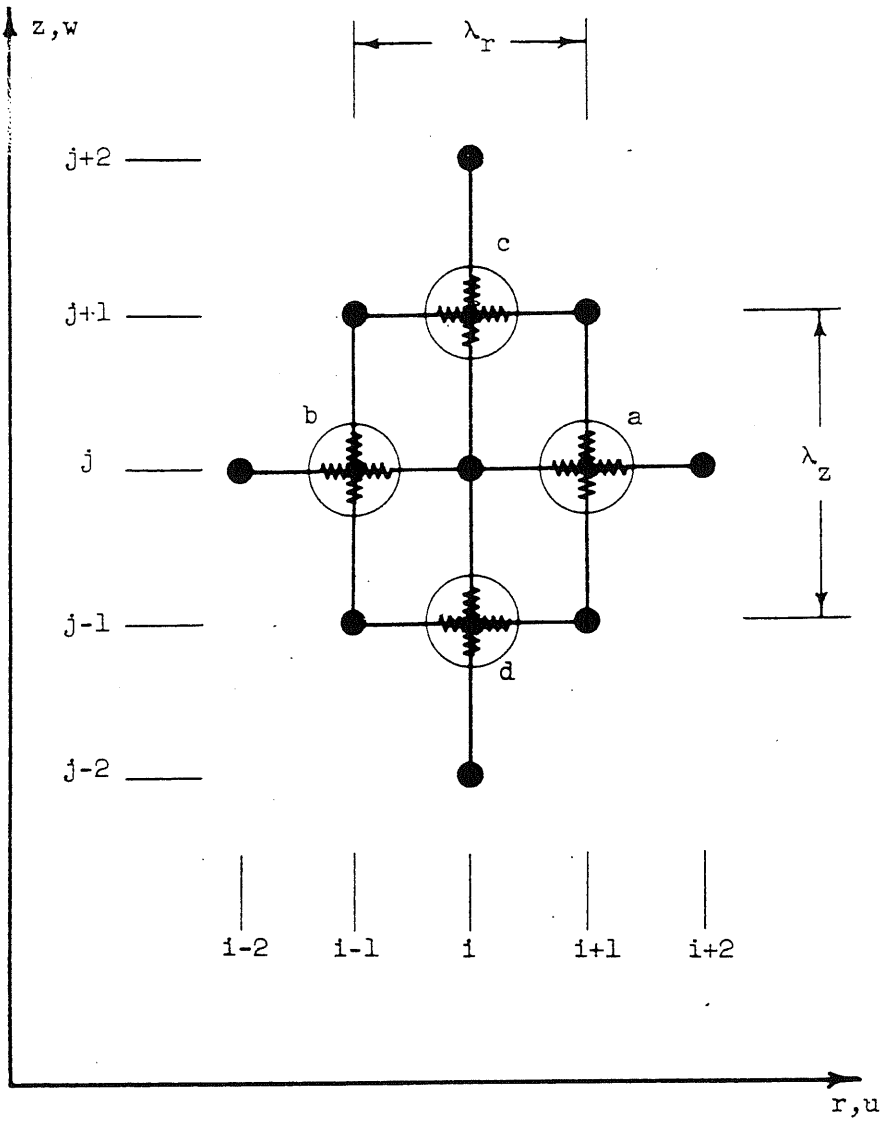

FIG. 6. MODEL ANALOGUE OF TYPICAL MASS ELEMENT

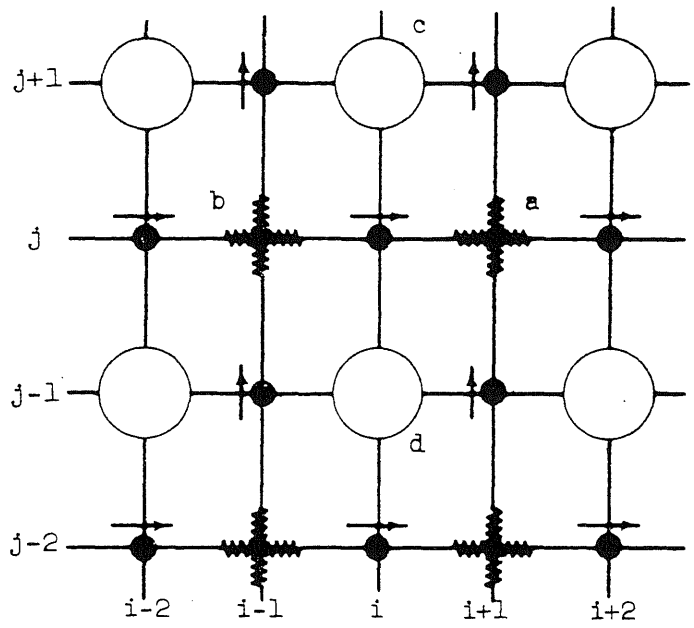

a. Grid 1

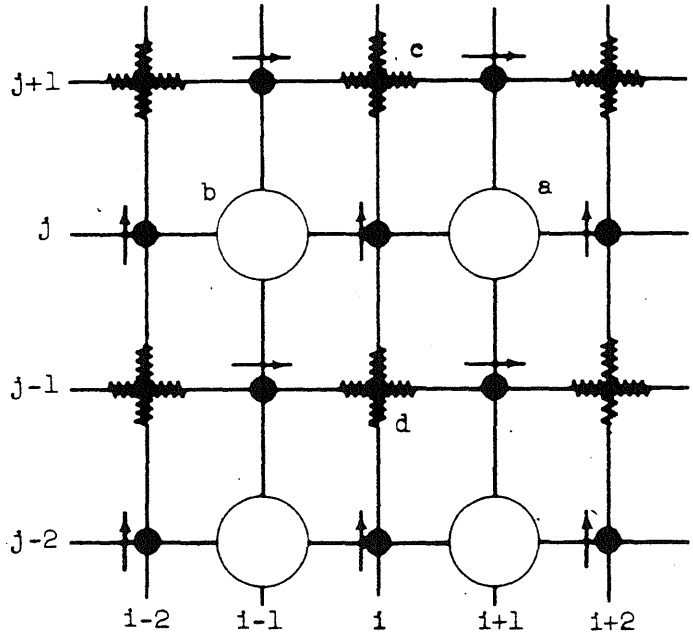

b. Grid 2

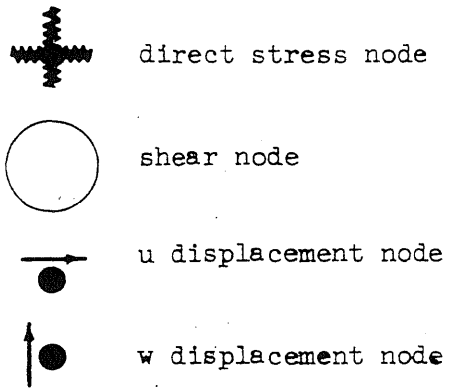

FIG. 7. COMPONENT GRIDS

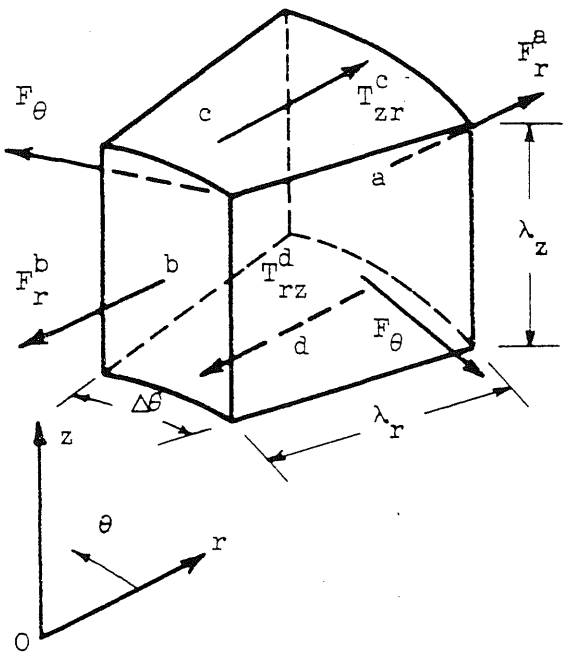

$$F_r^a = \sigma_r^a \, r_{i+1} \, \Delta\theta \, \lambda_z$$

$$F_r^b = \sigma_r^b \, r_{i-1} \, \Delta\theta \, \lambda_z$$

$$T_{rz}^c = \tau_{rz}^c \, r_i \, \Delta\theta \, \lambda_r$$

$$T_{rz}^d = \tau_{rz}^d \, r_i \, \Delta\theta \, \lambda_r$$

$$F_\theta = \sigma_\theta \, \lambda_r \lambda_z$$

FIG. 8. R EQUATION FORCES ACTING ON TYPICAL MASS ELEMENT

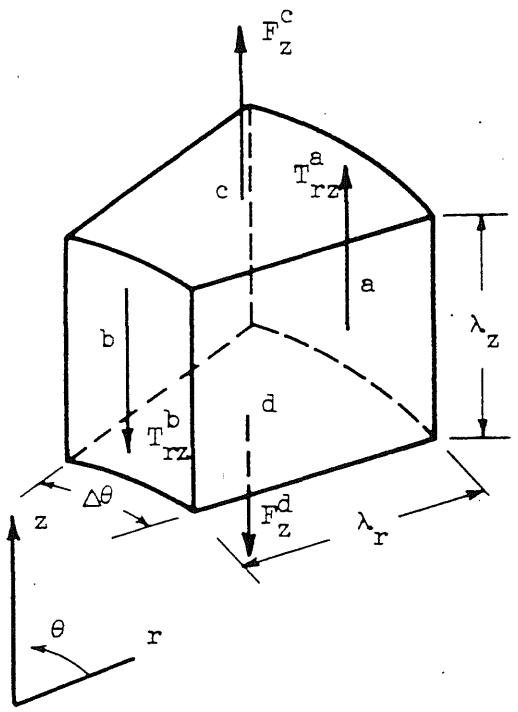

$$F_z^c = \sigma_z^c \, r_i \, \Delta\theta \, \lambda_r$$

$$F_z^d = \sigma_z^d \, r_i \, \Delta\theta \, \lambda_r$$

$$T_{rz}^a = \tau_{rz}^a \, r_{i+1} \, \Delta\theta \, \lambda_z$$

$$T_{rz}^b = \tau_{rz}^b \, r_{i-1} \, \Delta\theta \, \lambda_z$$

FIG. 9. Z EQUATION FORCES ACTING ON TYPICAL MASS ELEMENT

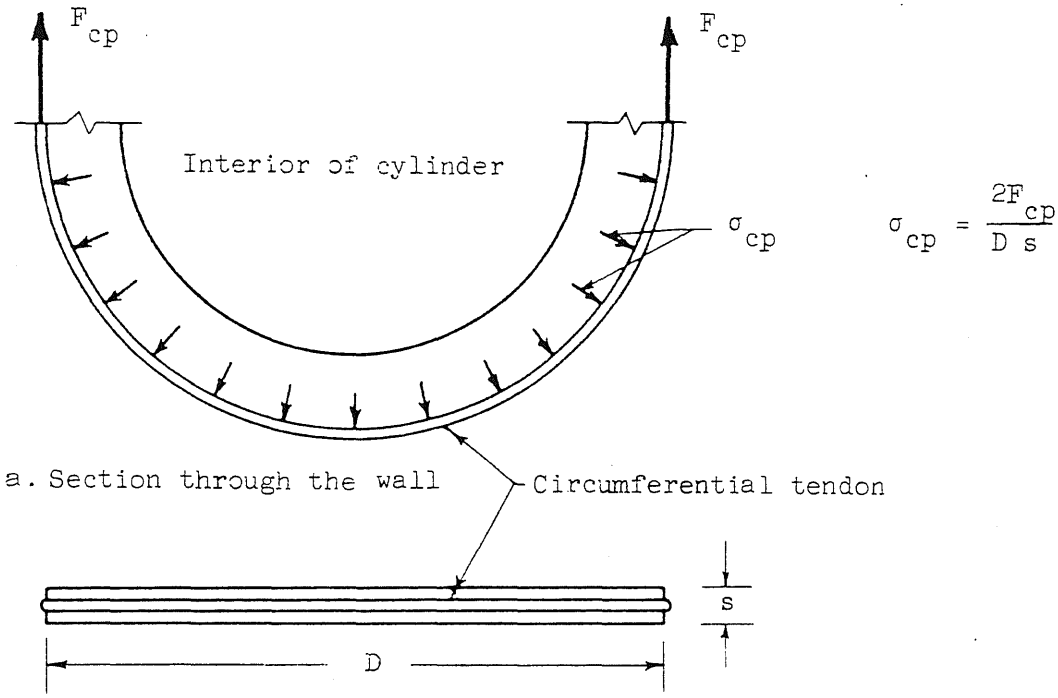

FIG. 10. NORMAL PRESSURE EQUIVALENT OF CIRCUMFERENTIAL PRESTRESSING

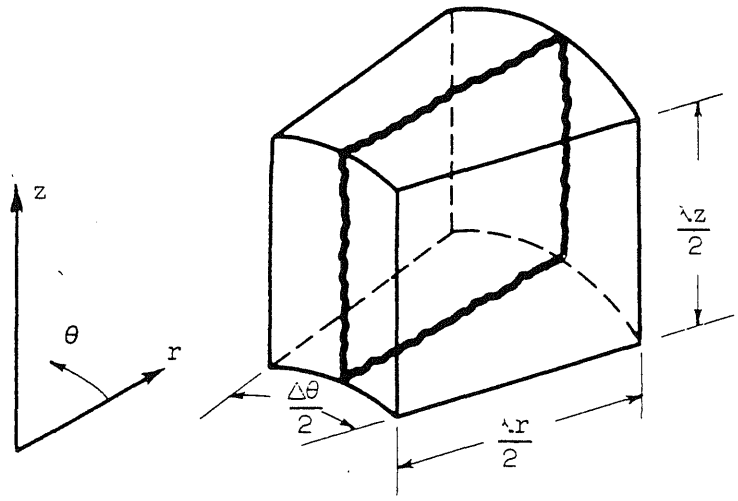

FIG. 11. RADIAL CRACK PLANE

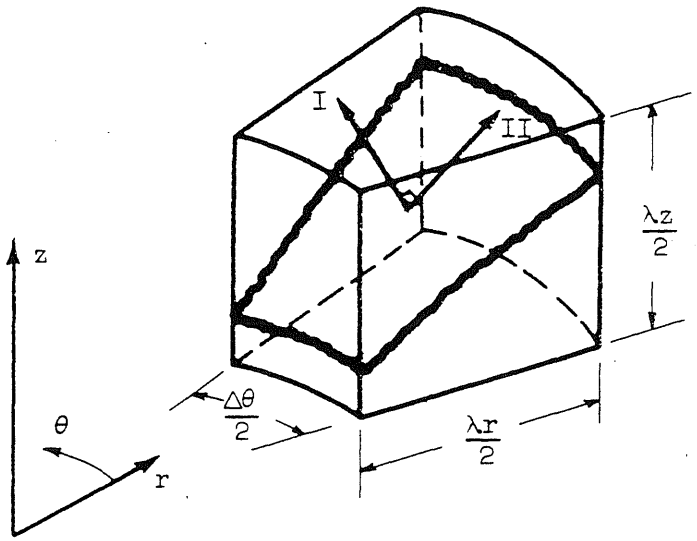

FIG. 12. CONICAL CRACK SURFACE

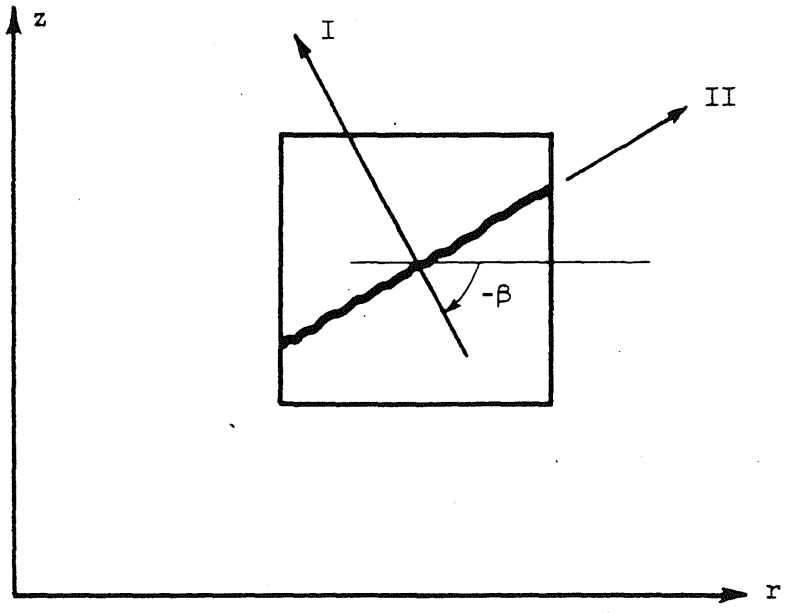

FIG. 13. CONICAL CRACK TRACE ON A RADIAL PLANE

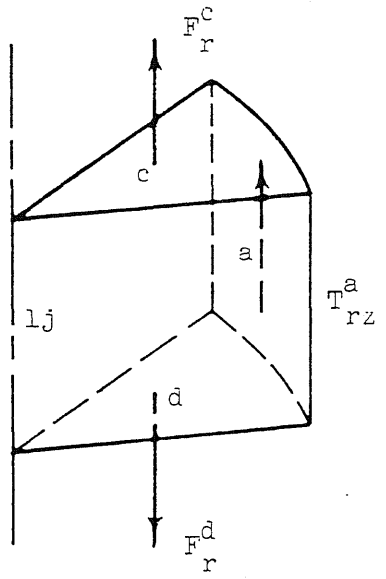

a. Mass Element

Equilibrium Equations:

r direction:

$$u_{1j} = 0$$

z direction:

$$\frac{\sigma_z^c - \sigma_z^d}{\lambda_z} + 4 \frac{\tau_{rz}^a}{\lambda_r} = 0$$

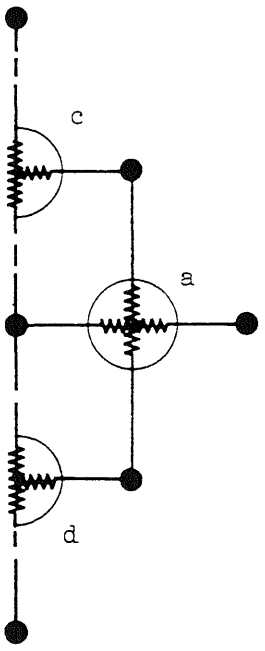

b. Grid Representation

Strain-displacement relations:

$$\epsilon_r^c = 2 \frac{u_{2j+1}}{\lambda_r}$$

$$\epsilon_\theta^c = \epsilon_r^c$$

$$\gamma_{rz}^c = 0$$

FIG. 14. BOUNDARY CONDITIONS AT THE AXIS OF SYMMETRY

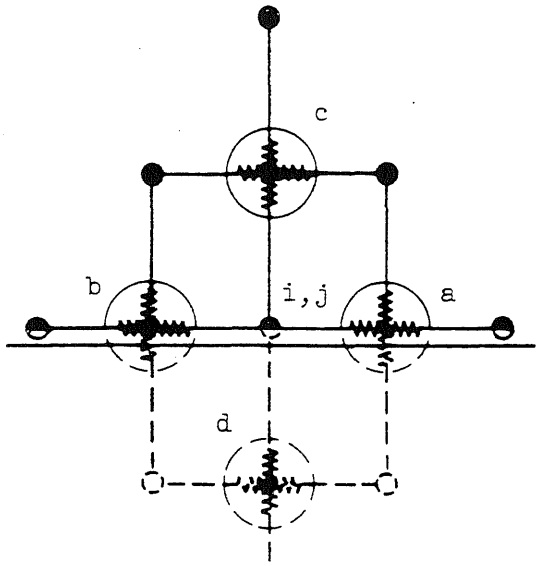

Equilibrium Equations:

r direction:

$$\frac{\sigma_r^a - \sigma_r^b}{\lambda_r} + 2\frac{\tau_{rz}^b}{\lambda_z} + \frac{\frac{1}{2}(\sigma_r^a + \sigma_r^b) - \sigma_\theta}{r_i} = 0$$

z direction:

$$w_{i1} = 0$$

$$\epsilon_z^a = 2\frac{w_{i+1,1}}{\lambda_z}$$

FIG. 15. BOUNDARY CONDITIONS AT MID-HEIGHT

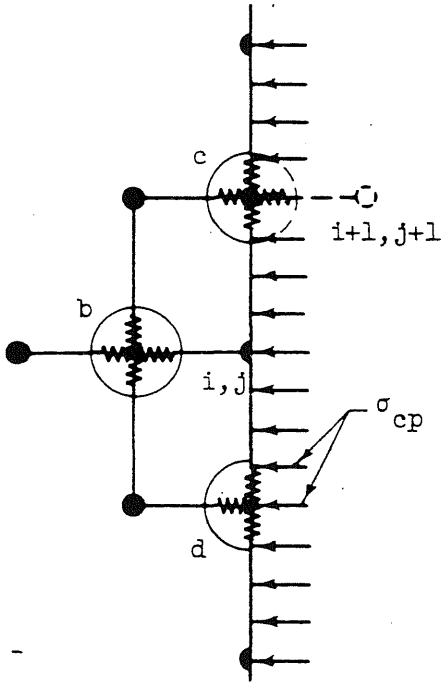

Equilibrium Equations:

r direction:

$$-2\frac{\sigma_{cp} + \sigma_r^b}{\lambda_r} + \frac{\sigma_r^b - \sigma_\theta}{r_i} = 0$$

z equation:

$$\frac{\sigma_z^c - \sigma_z^d}{\lambda_z}\left(1 - \frac{\lambda_r}{4r_i}\right) - 2\frac{\tau_{rz}^b}{\lambda_r} + \frac{\tau_{rz}^b}{r_i} = 0$$

FIG. 16. BOUNDARY CONDITIONS AT EXTERIOR WALL SURFACE

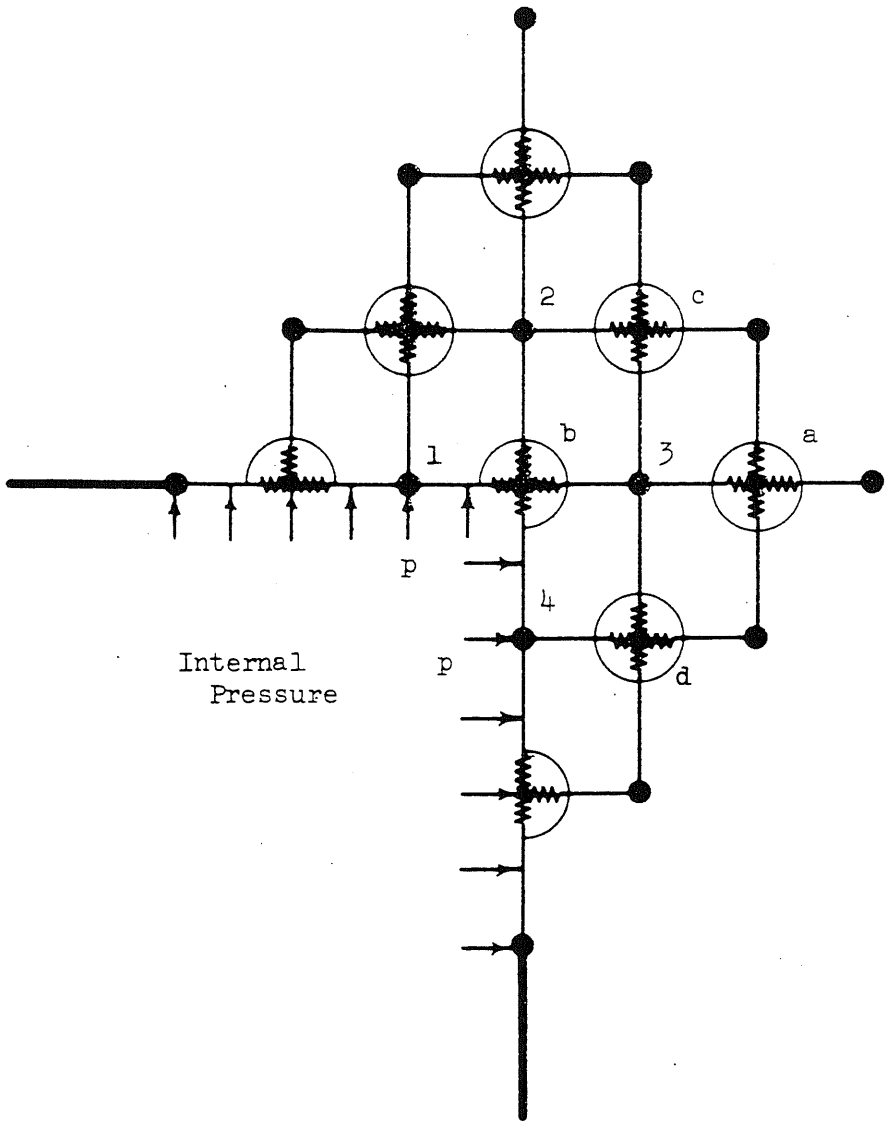

FIG. 17. GRID REPRESENTATION OF RE-ENTRANT CORNER

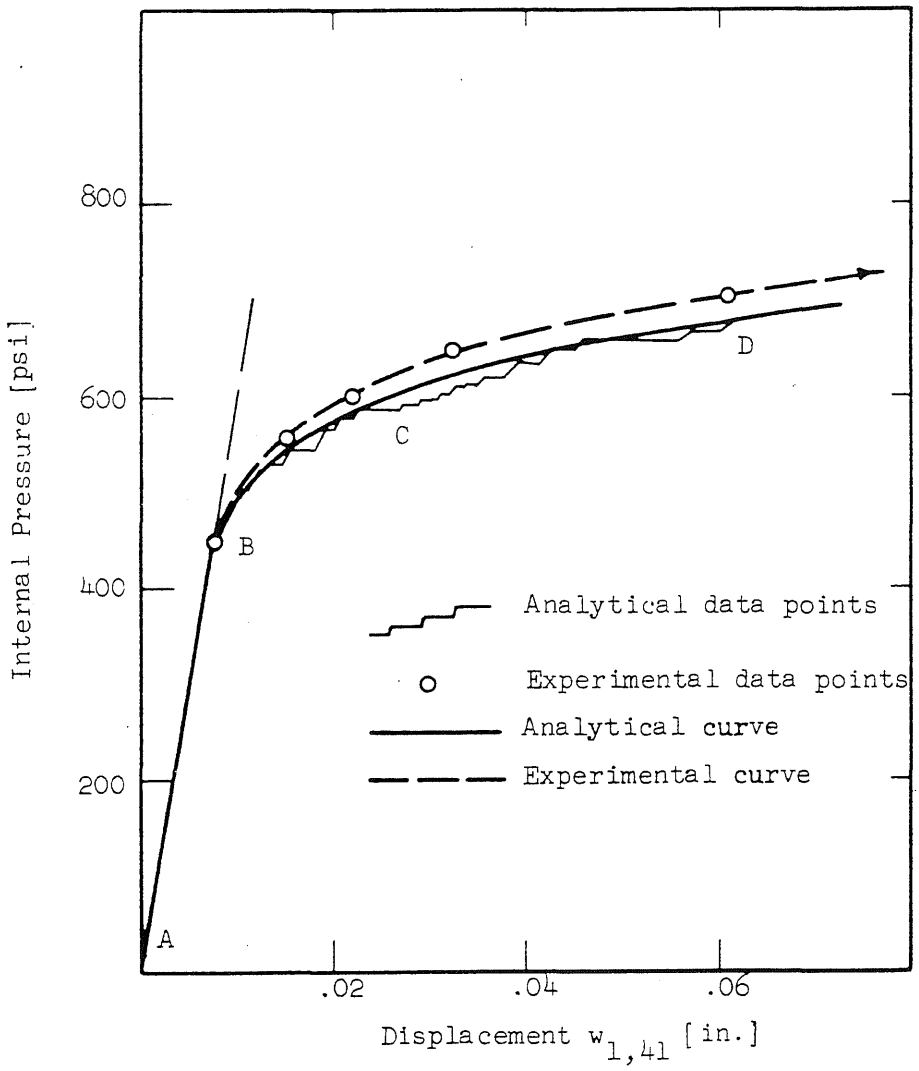

FIG. 18. LOAD-DEFORMATION DIAGRAM FOR THE SAMPLE VESSEL

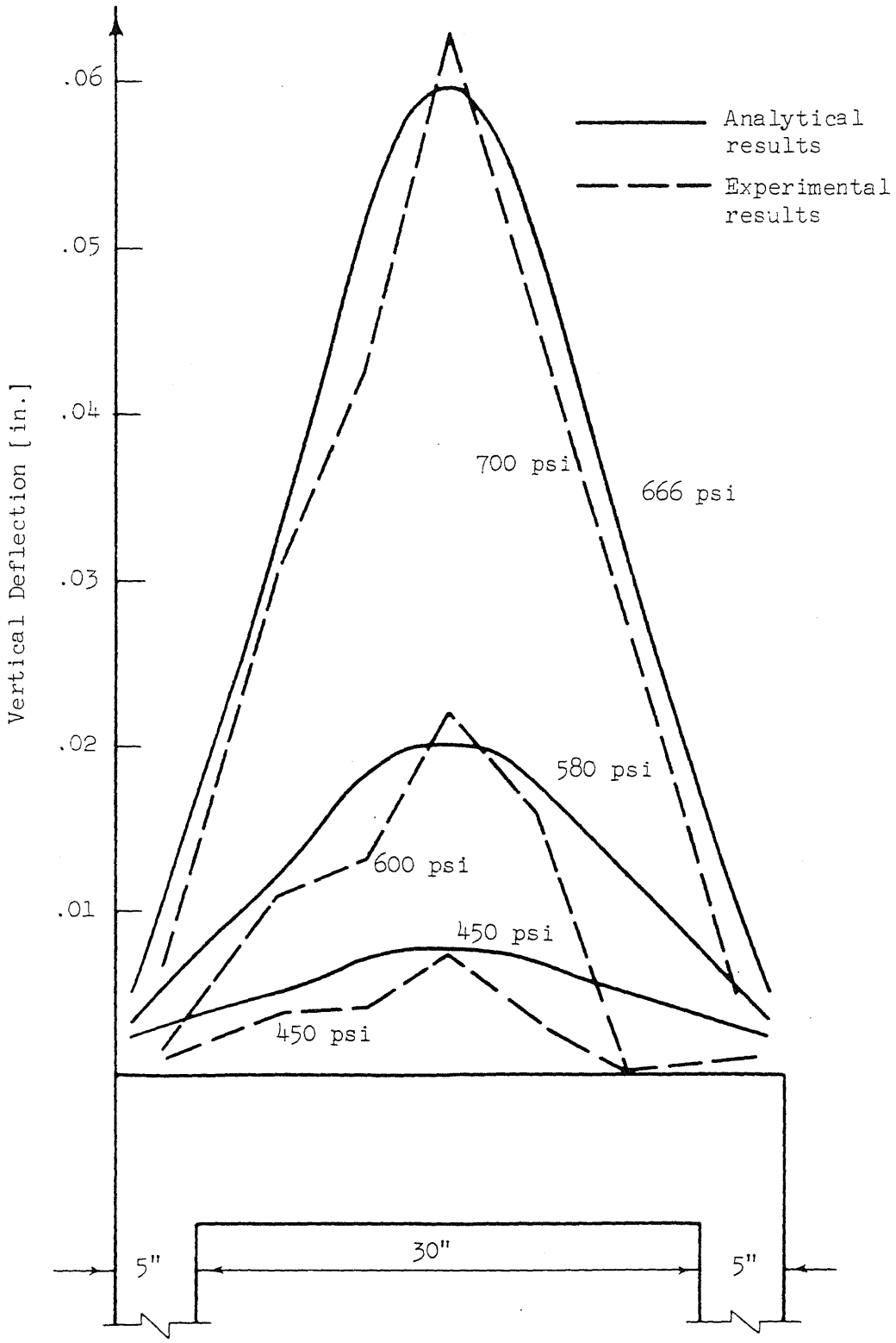

FIG. 19. DEFLECTION PROFILES OF THE END SLAB

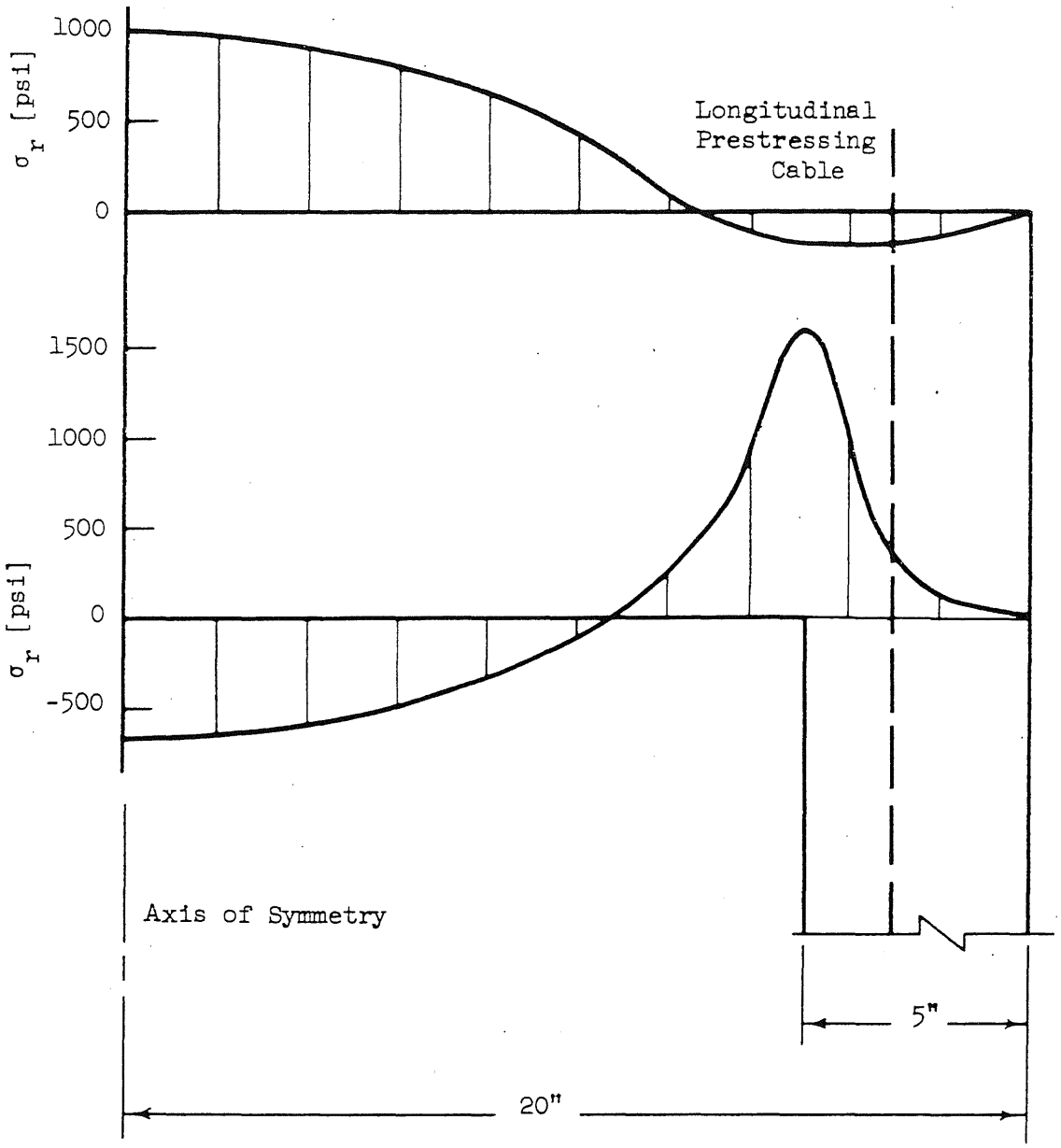

FIG. 20. RADIAL STRESSES IN THE SLAB UNDER INTERNAL PRESSURE OF 450 PSI AND ZERO PRESTRESS

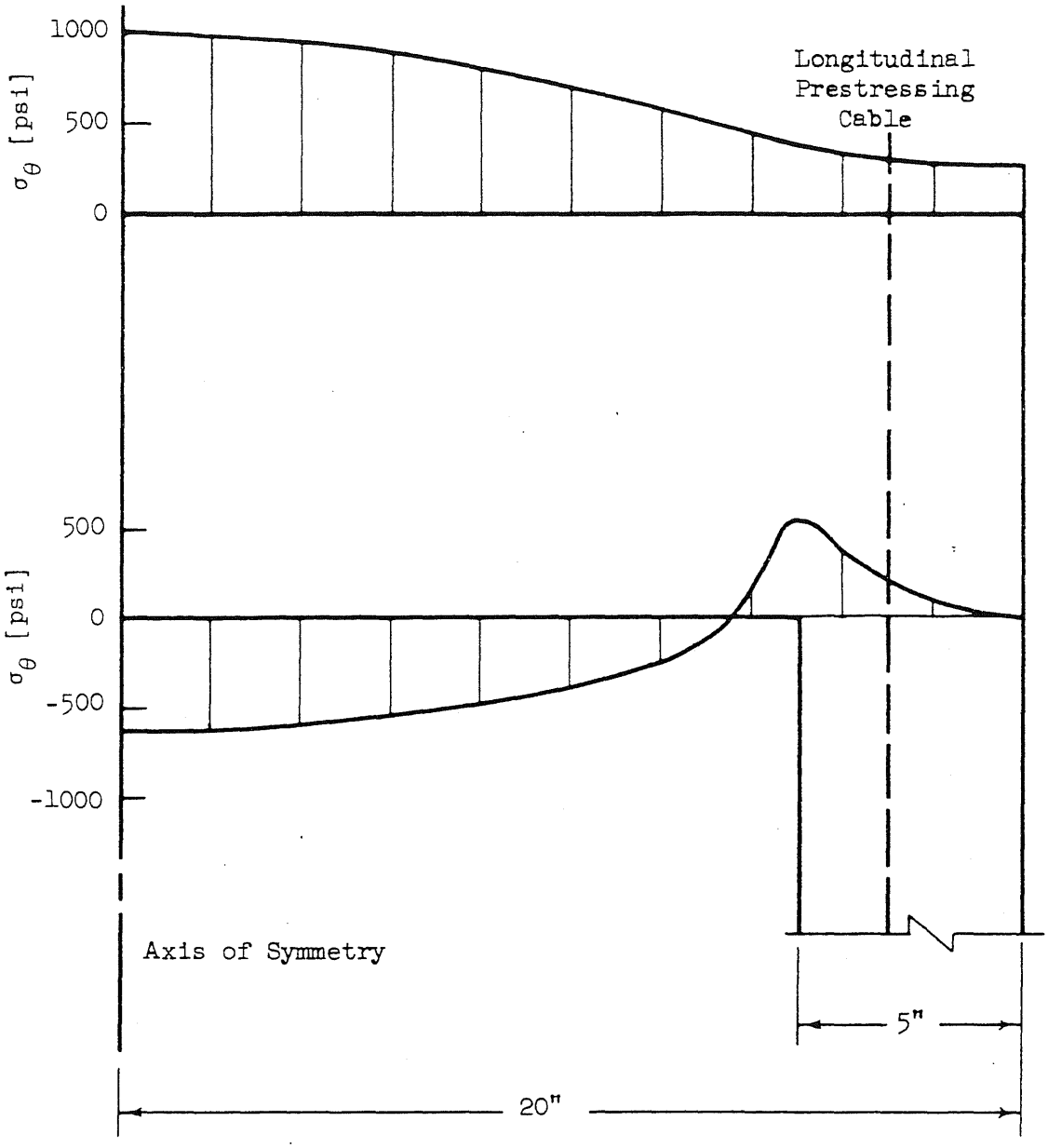

FIG. 21. CIRCUMFERENTIAL STRESSES IN THE SLAB UNDER INTERNAL PRESSURE OF 450 PSI AND ZERO PRESTRESS

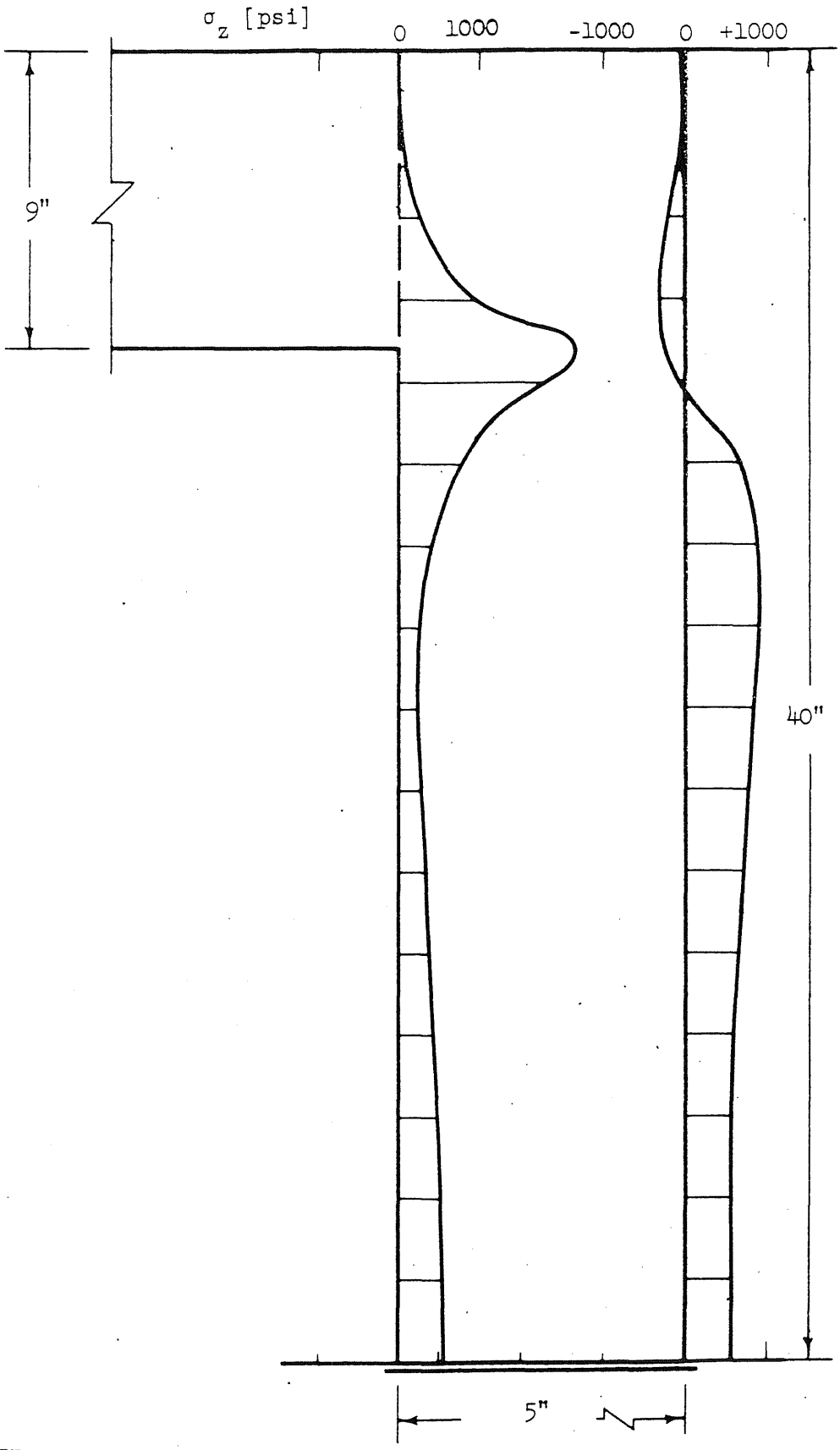

FIG. 22. LONGITUDINAL STRESSES IN THE CYLINDRICAL SIDE WALL UNDER INTERNAL PRESSURE OF 450 PSI AND ZERO PRESTRESS

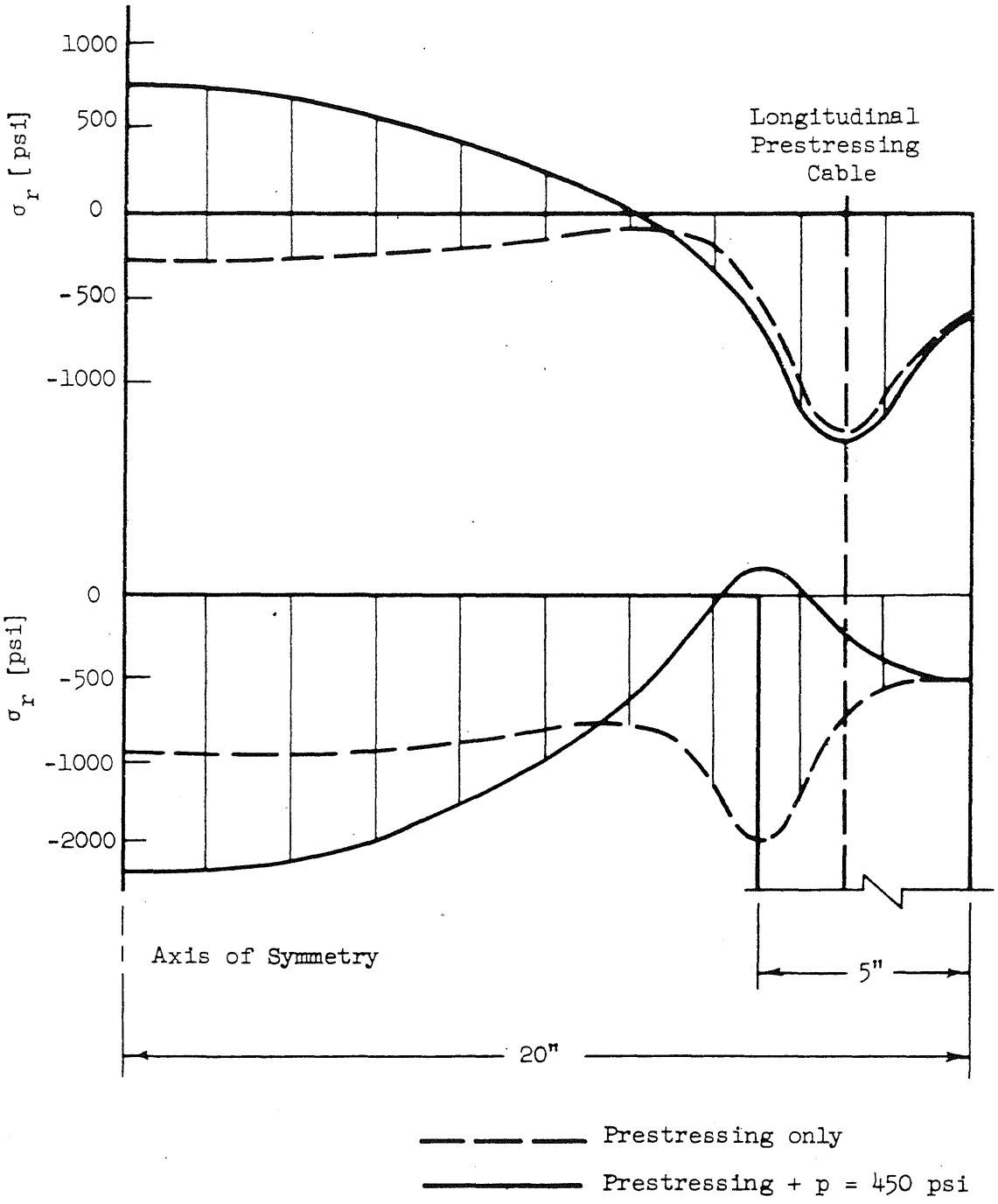

FIG. 23. RADIAL STRESSES IN THE SLAB FROM PRESTRESS AND PRESTRESS PLUS 450 PSI INTERNAL PRESSURE

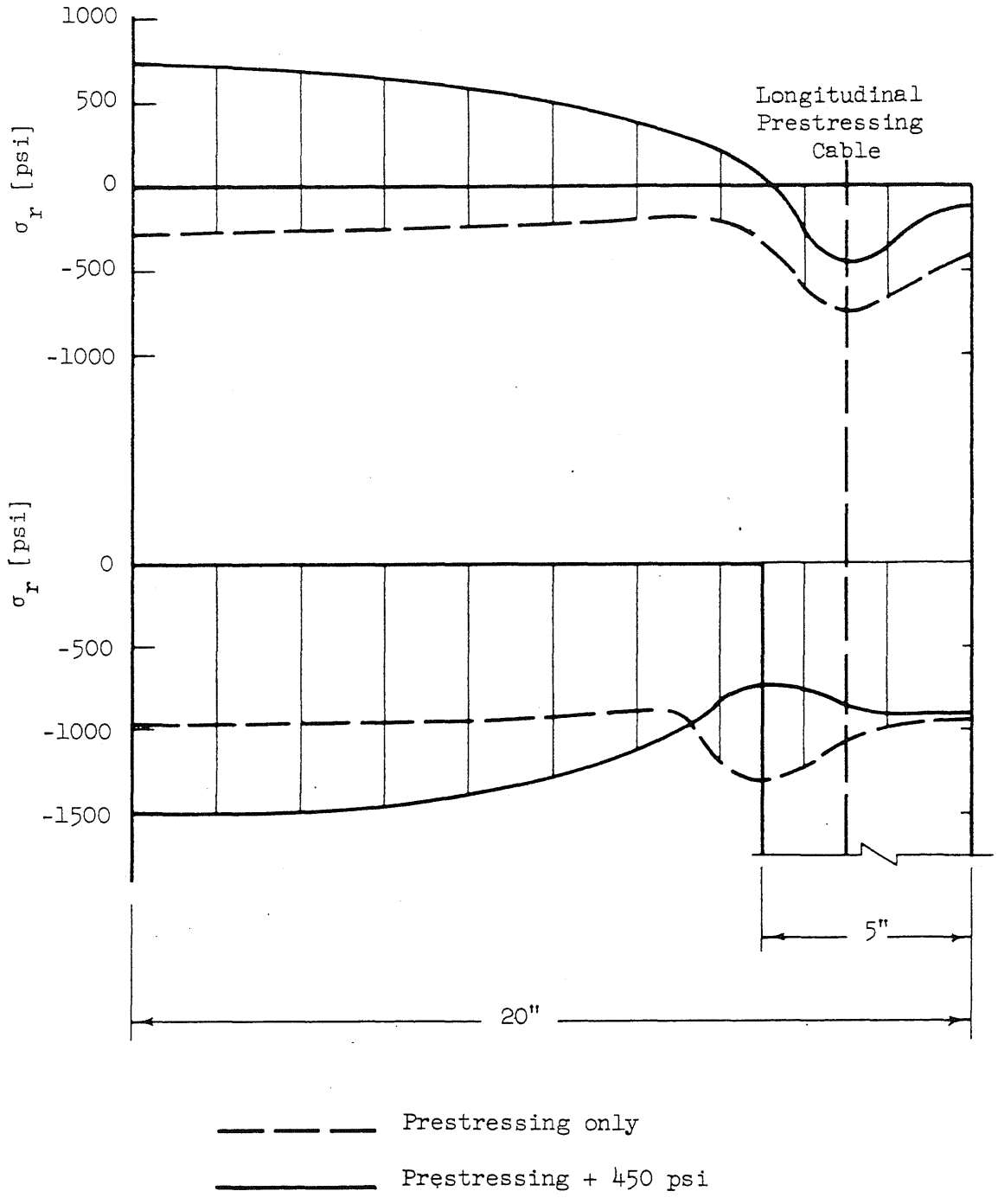

FIG. 24. CIRCUMFERENTIAL STRESSES IN THE SLAB FROM PRESTRESS AND PRESTRESS PLUS 450 PSI INTERNAL PRESSURE

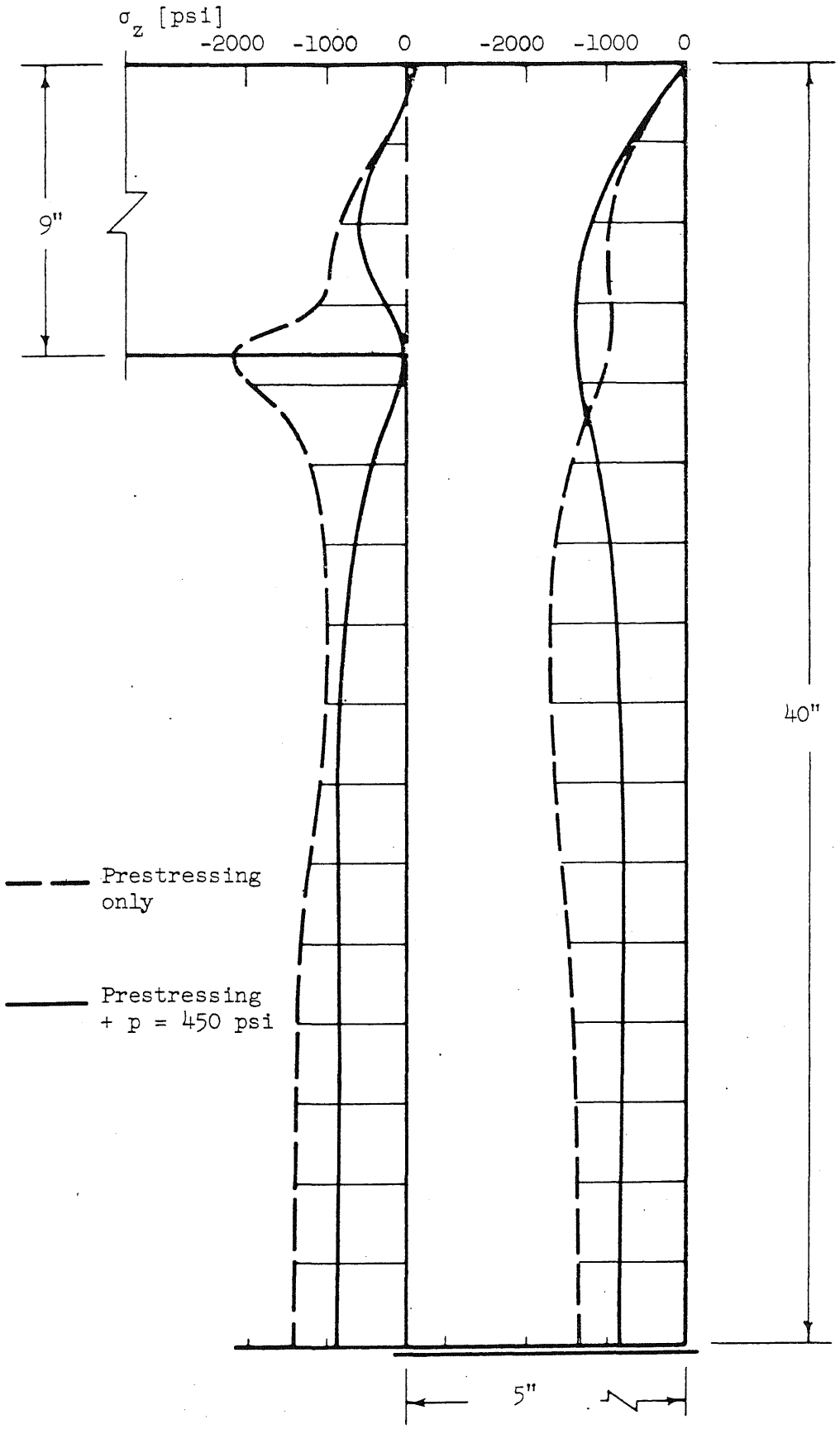

FIG. 25. LONGITUDINAL STRESSES IN THE CYLINDRICAL SIDE WALL FROM PRESTRESS AND PRESTRESS PLUS 450 PSI INTERNAL PRESSURE

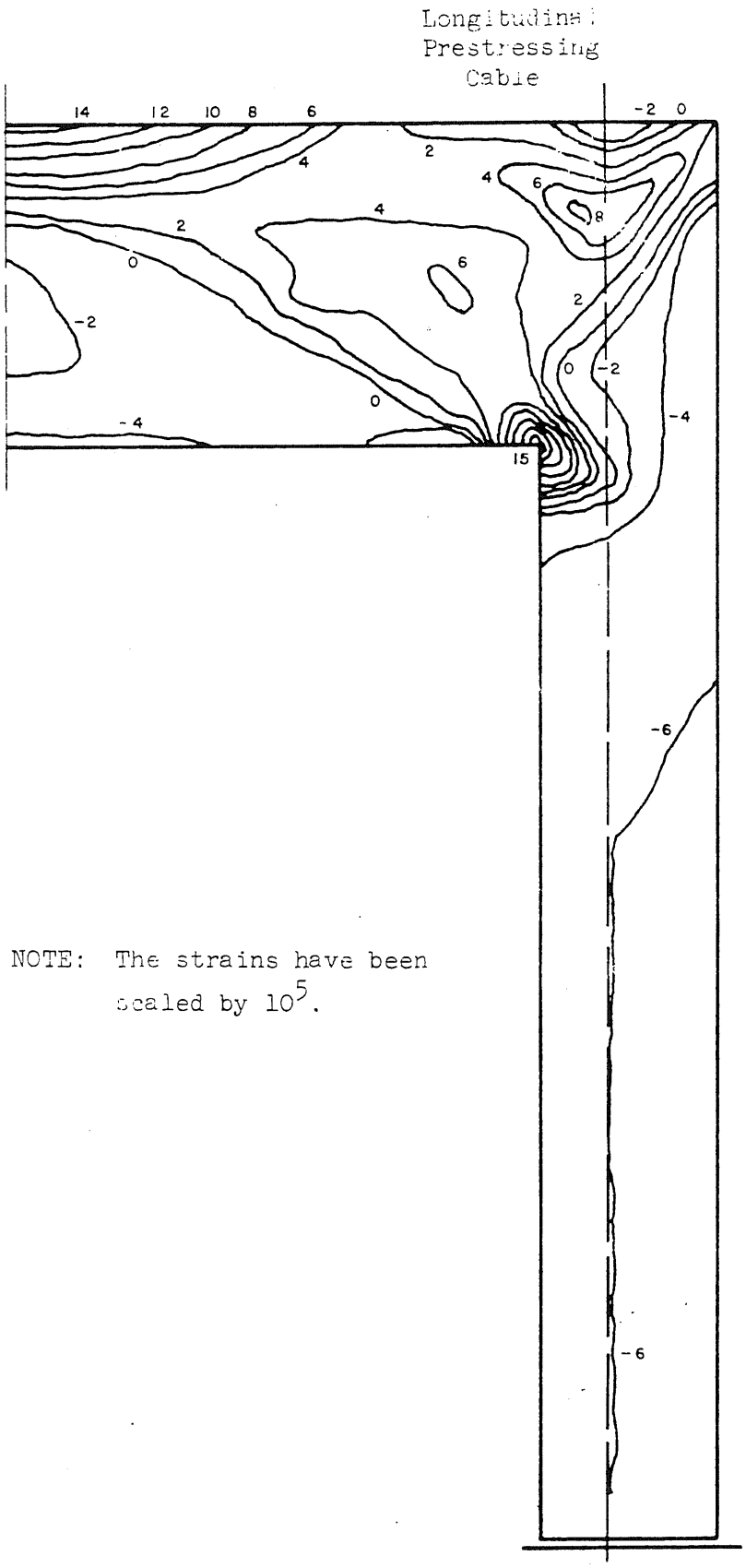

NOTE: The strains have been scaled by 10^5.

FIG. 26. MAXIMUM PRINCIPAL rz PLANE STRAIN TRAJECTORIES FOR PRESSURE OF 450 PSI

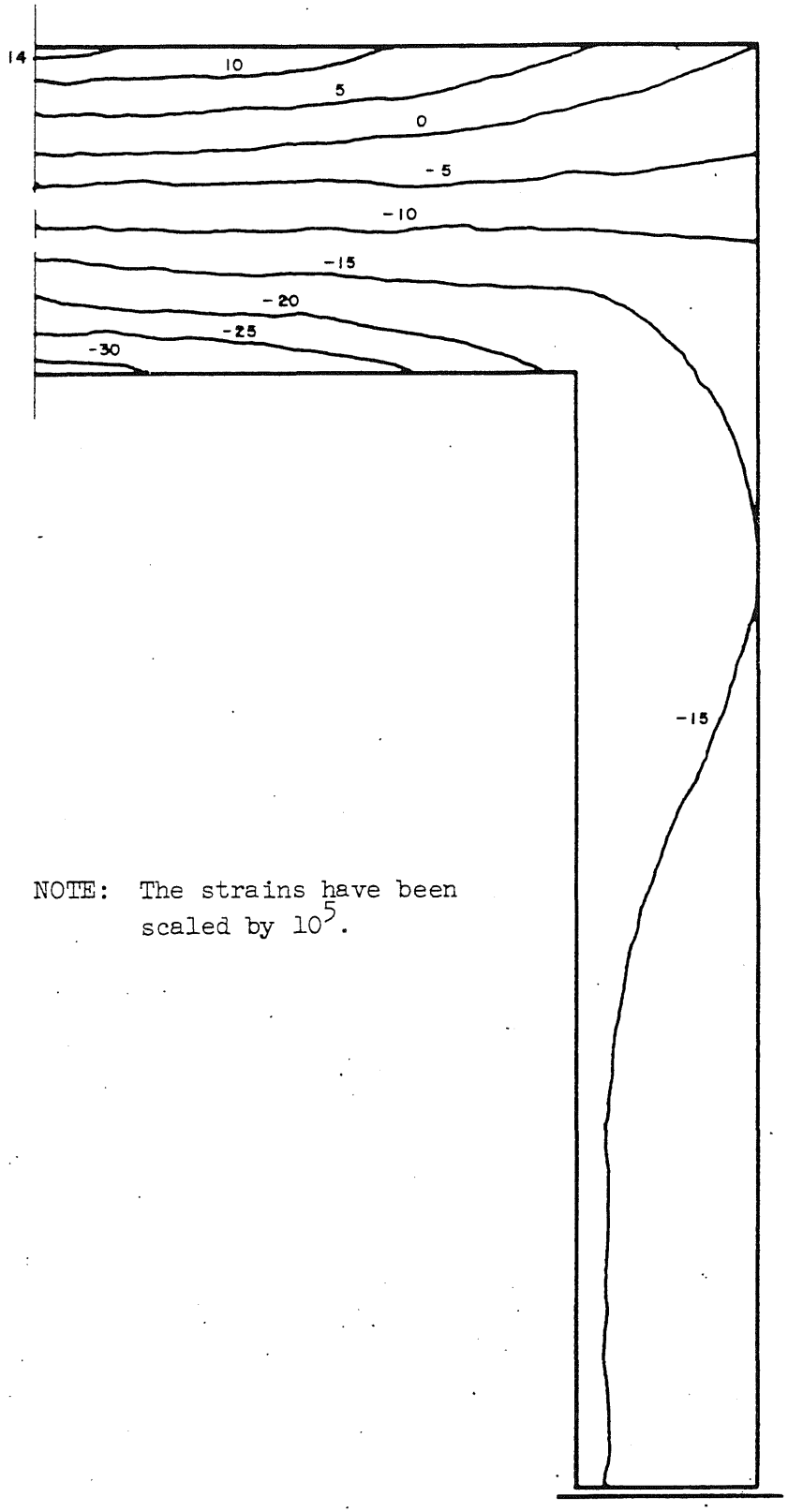

FIG. 27. CIRCUMFERENTIAL STRAIN TRAJECTORIES FOR PRESSURE OF 450 PSI

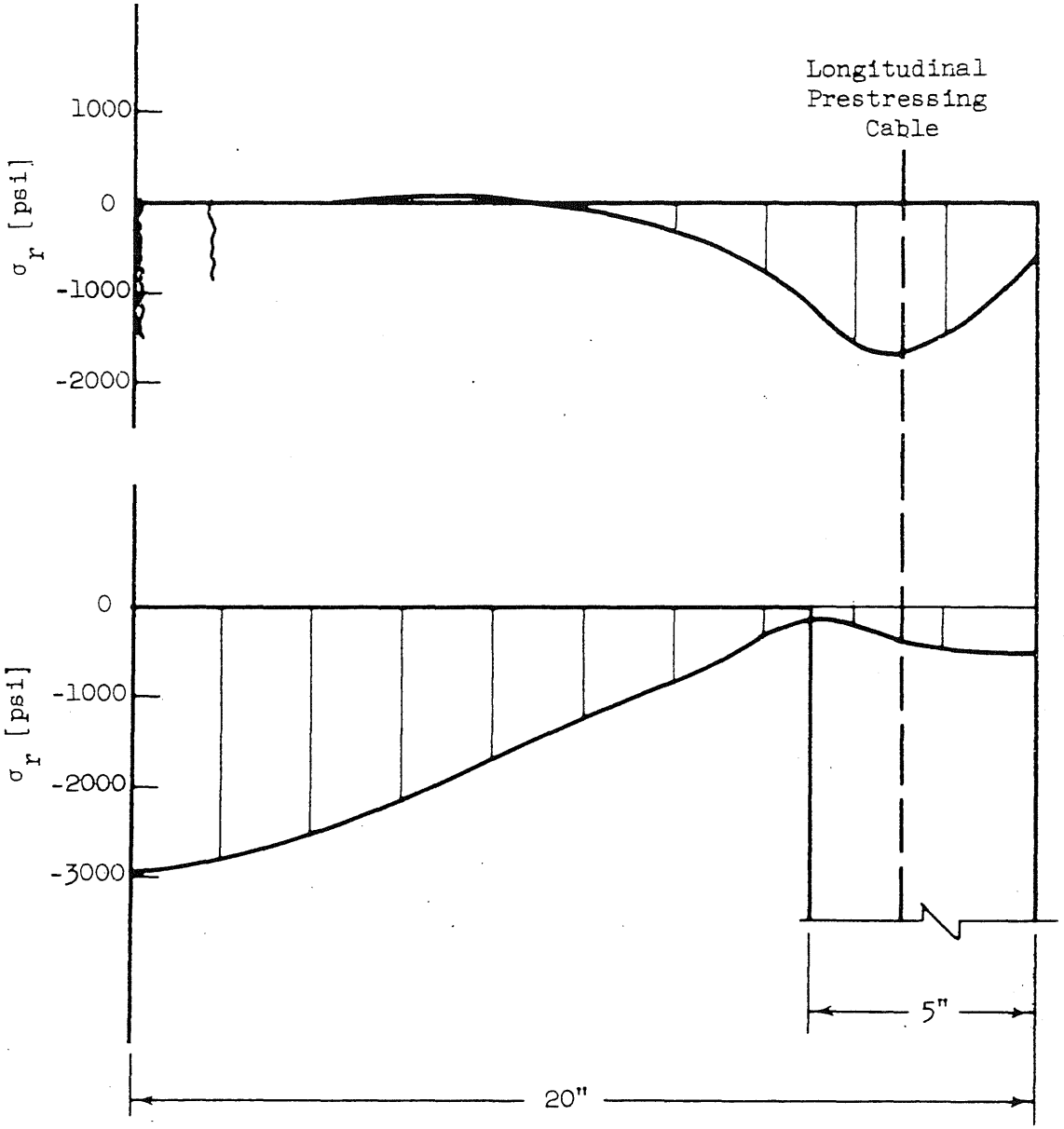

FIG. 28. RADIAL STRESSES IN THE SLAB FOR PRESSURE OF 580 PSI

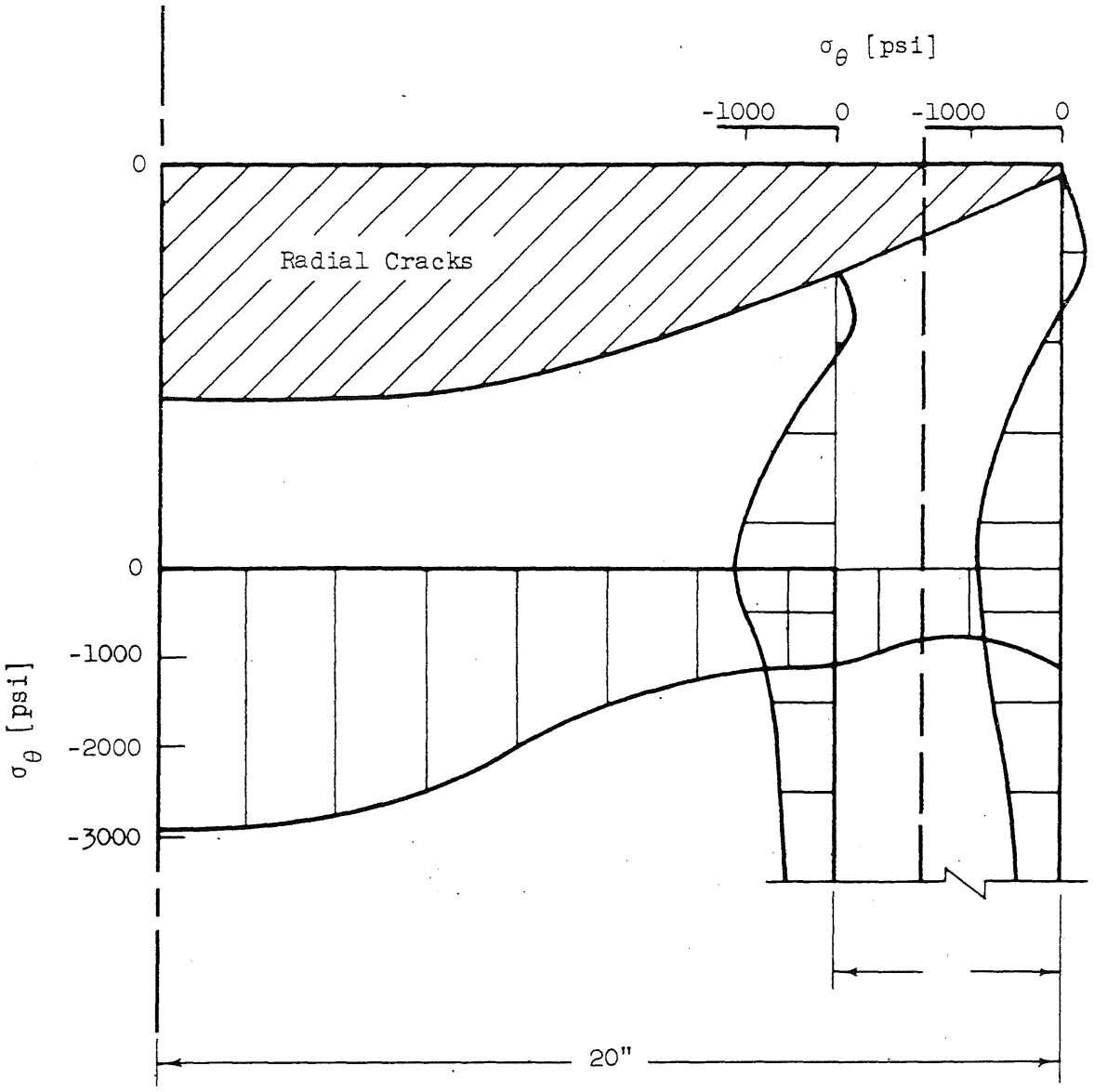

FIG. 29. CIRCUMFERENTIAL STRESSES IN THE SLAB AND CYLINDRICAL SIDE WALL FOR PRESSURE OF 580 PSI

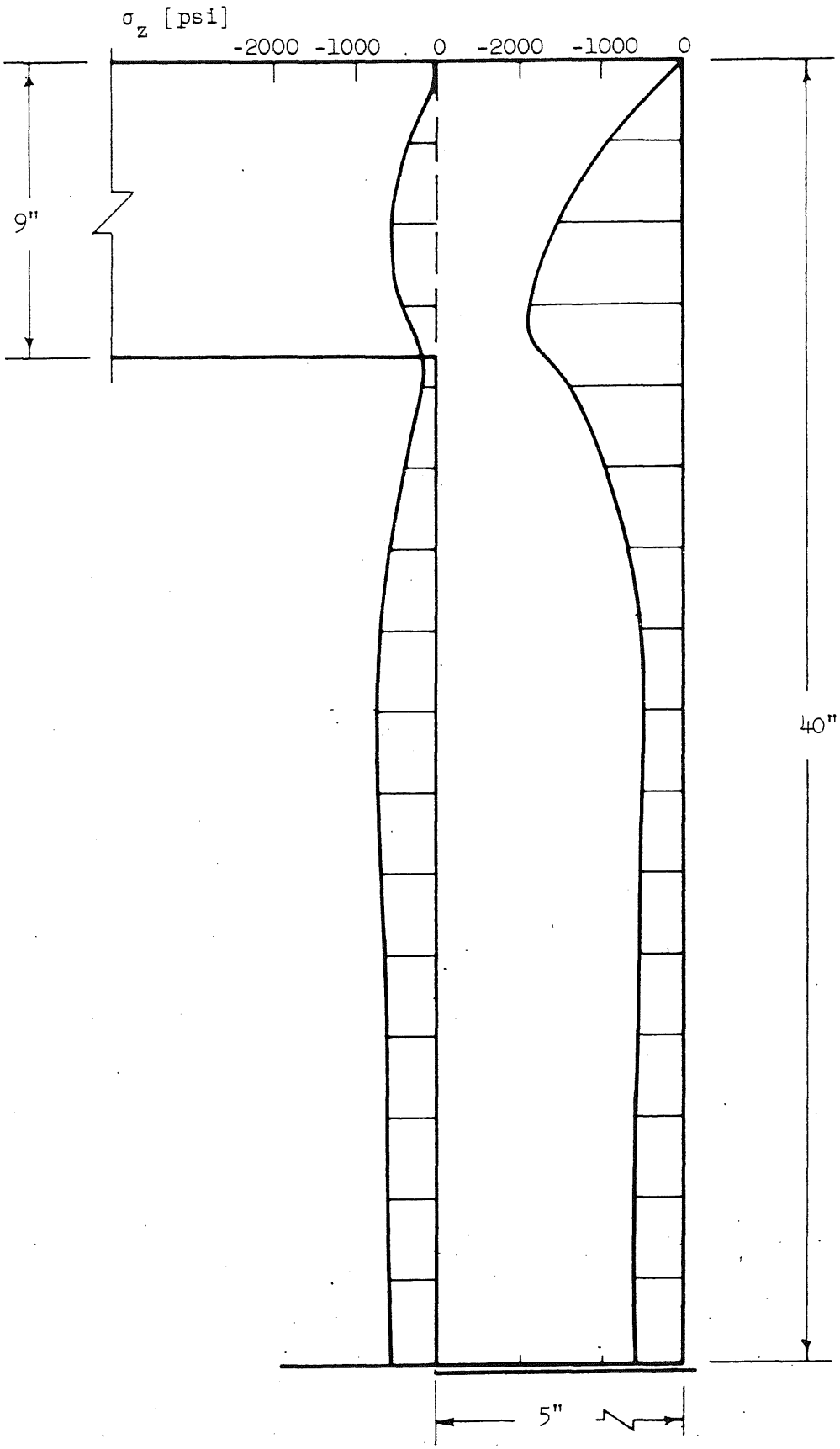

FIG. 30. LONGITUDINAL STRESSES IN THE CYLINDRICAL SIDE WALL FOR PRESSURE OF 580 PSI

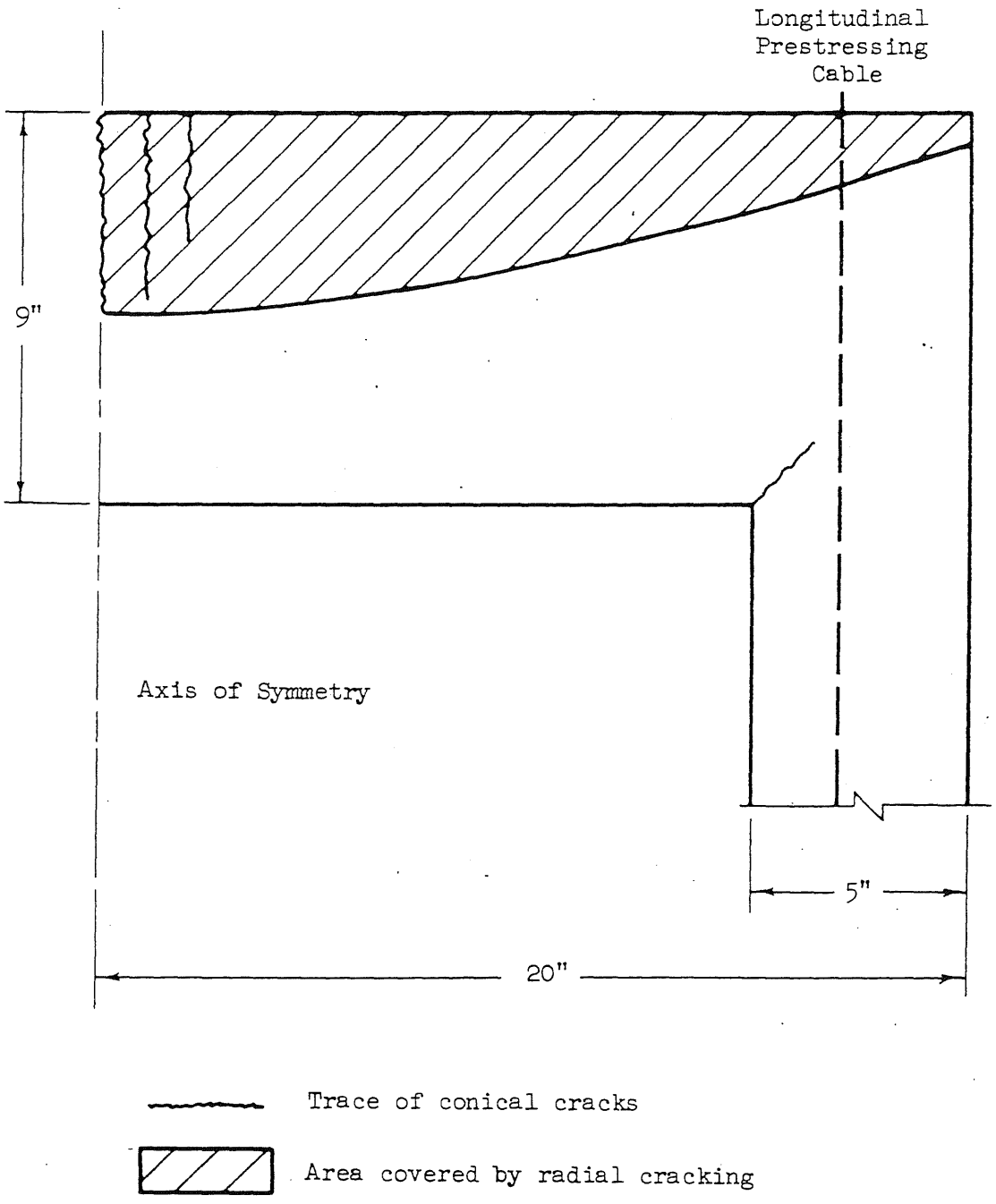

FIG. 31. EXTENT OF CRACKING FOR PRESSURE OF 580 PSI

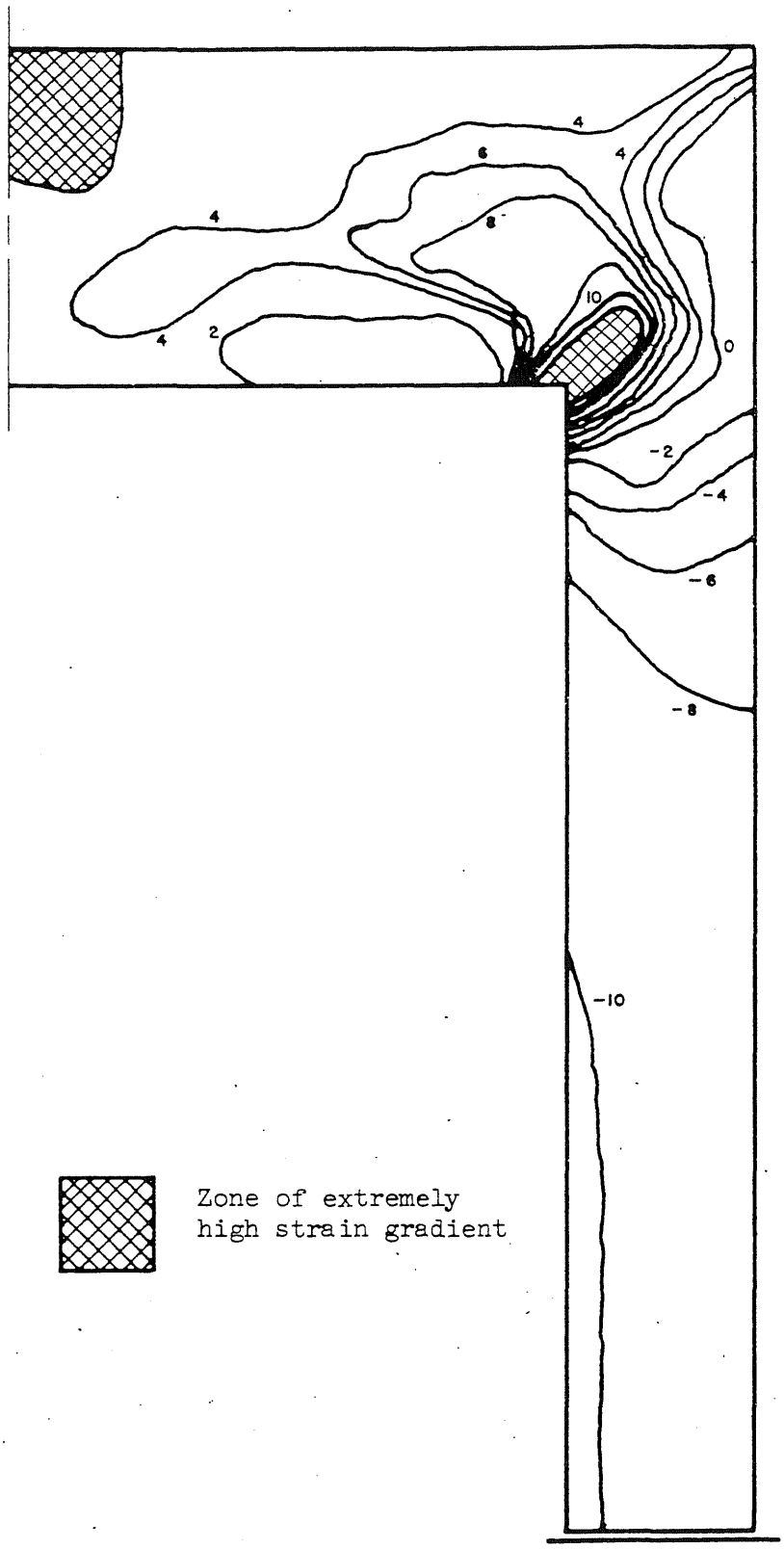

FIG. 32. MAXIMUM PRINCIPAL rz PLANE STRAIN TRAJECTORIES FOR PRESSURE OF 580 PSI

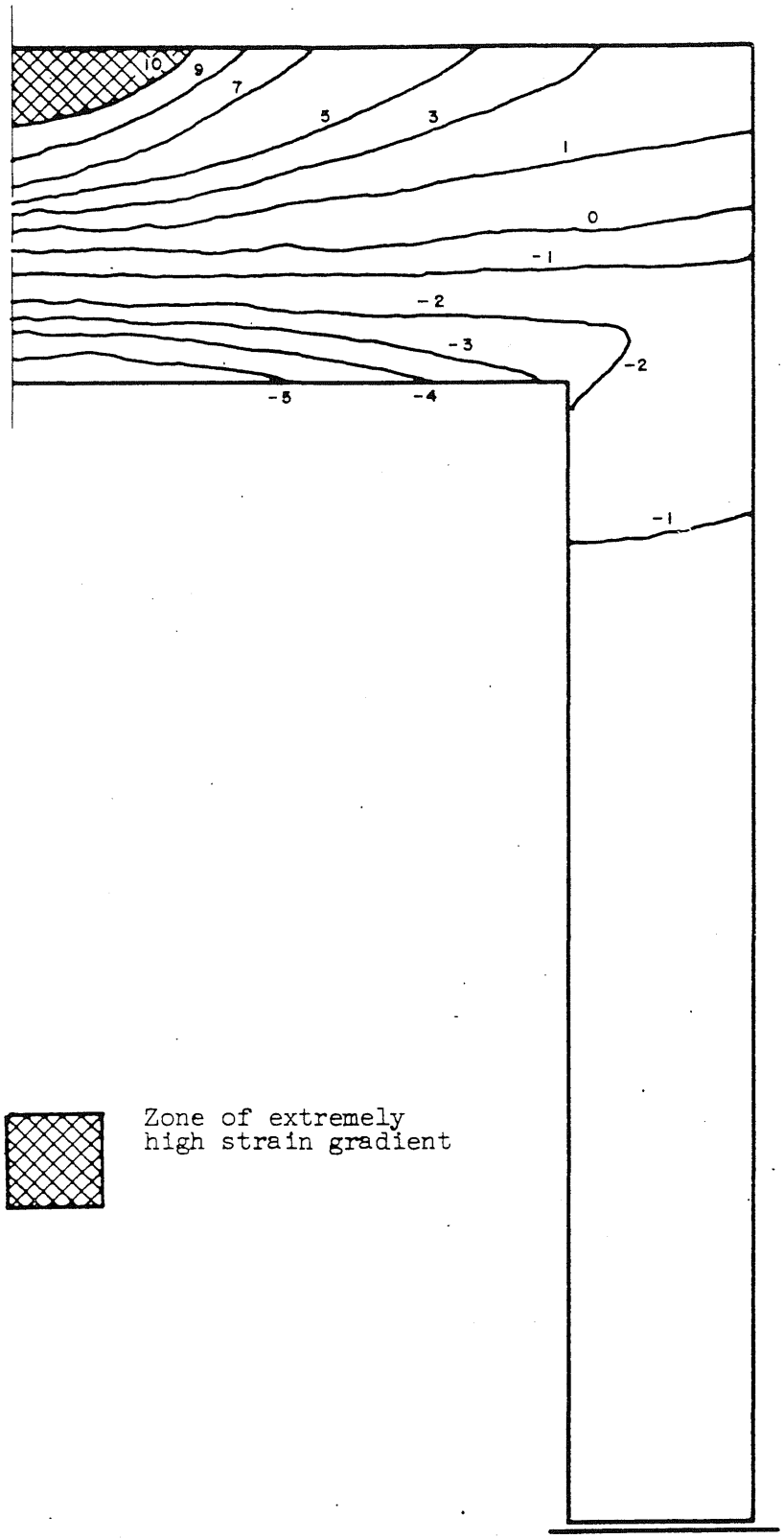

FIG. 33. CIRCUMFERENTIAL STRAIN TRAJECTORIES FOR PRESSURE OF 580 PSI

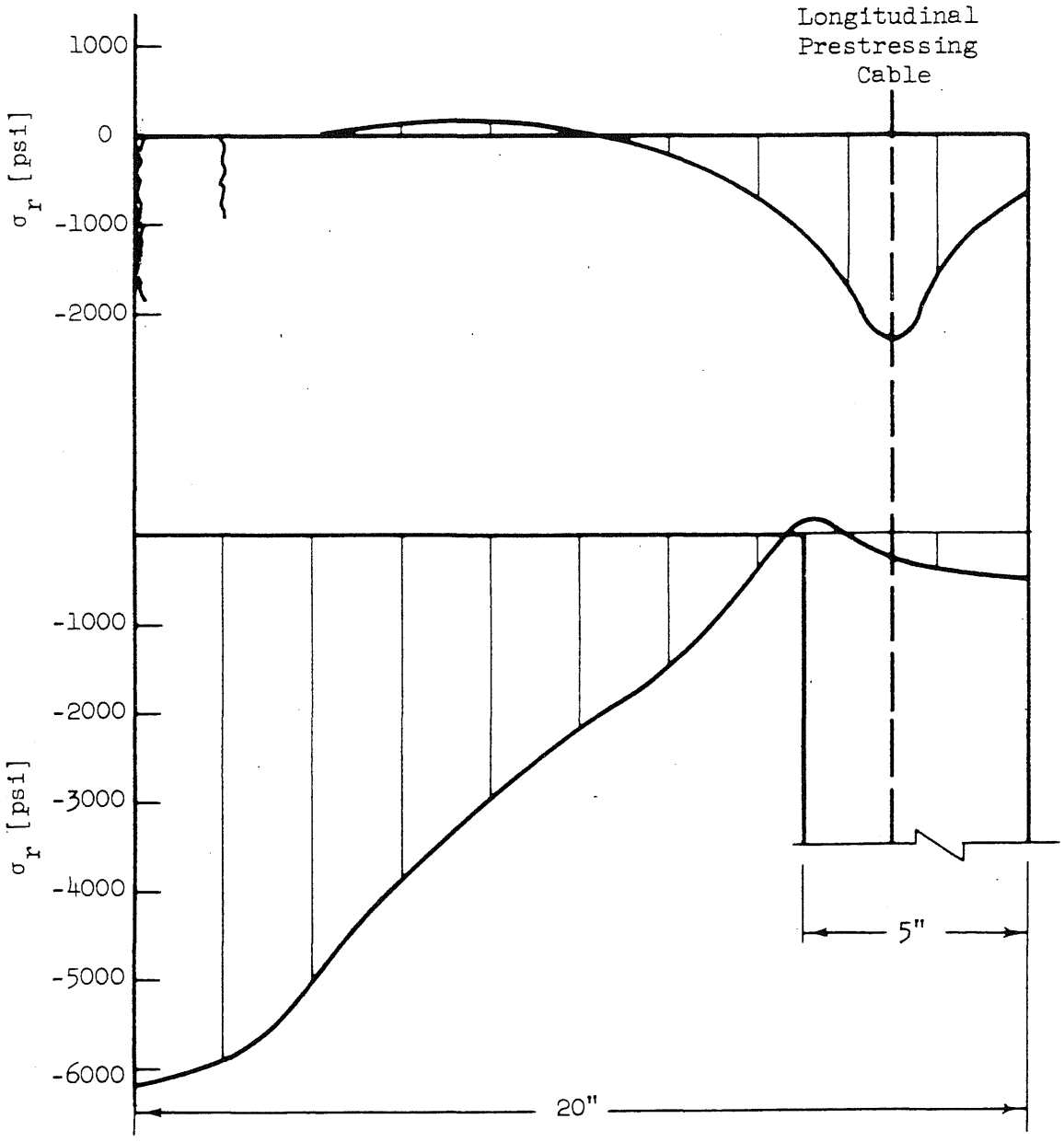

FIG. 34. RADIAL STRESSES IN THE SLAB FOR 666 PSI INTERNAL PRESSURE

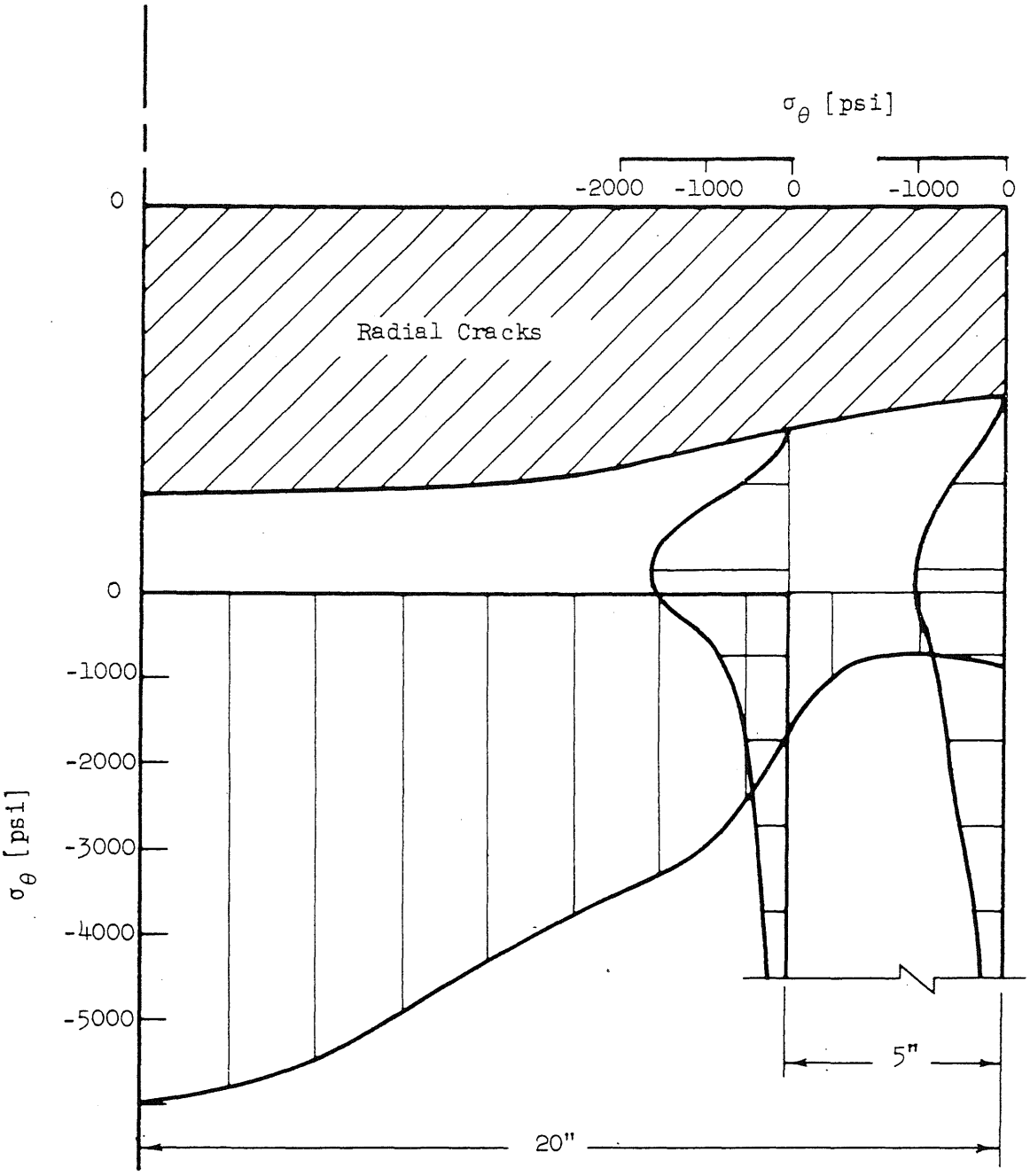

FIG. 35. CIRCUMFERENTIAL STRESSES IN THE SLAB AND CYLINDRICAL SIDE WALL FOR PRESSURE OF 666 PSI

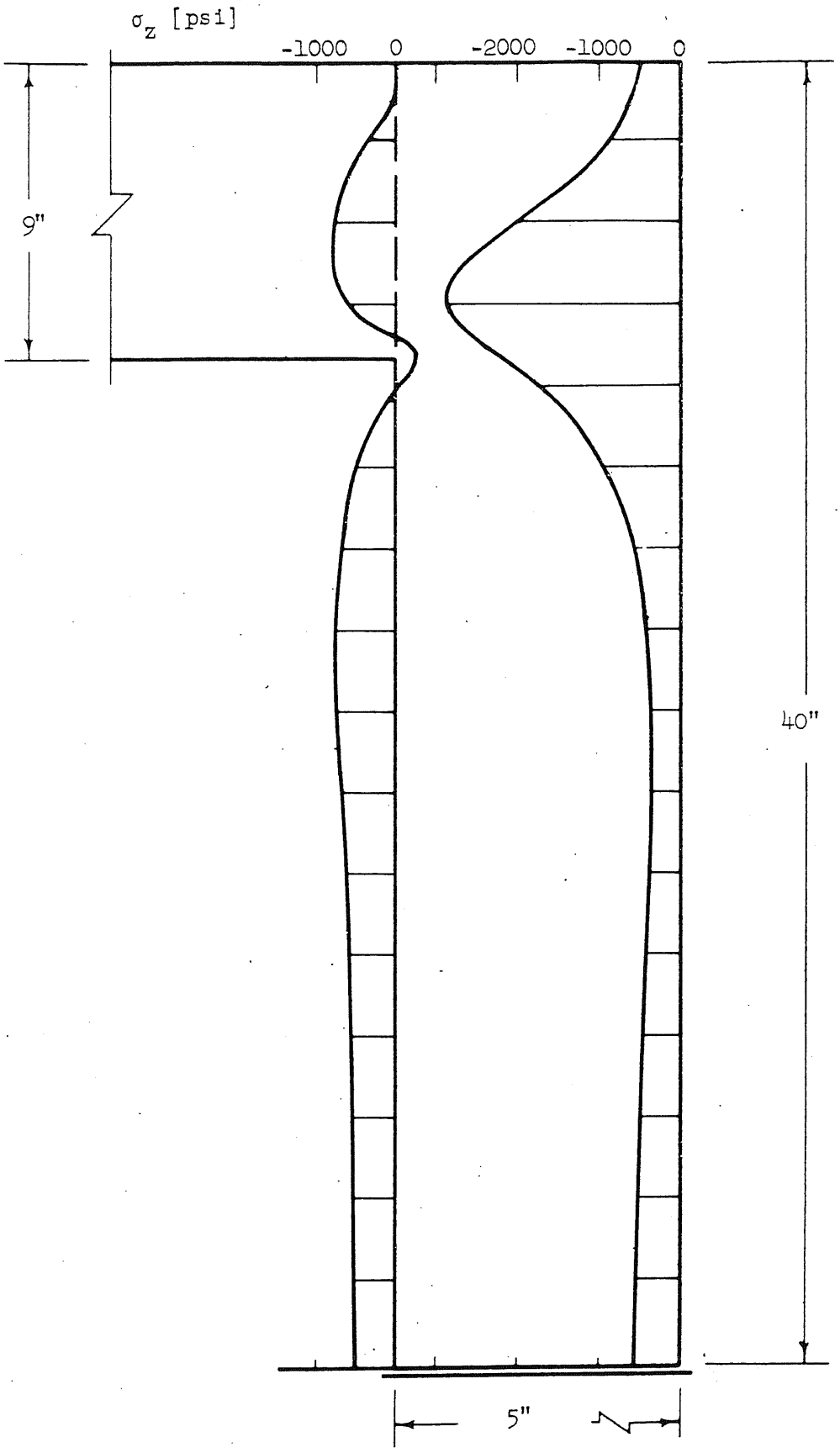

FIG. 36. LONGITUDINAL STRESSES IN THE CYLINDRICAL SIDE WALL FOR PRESSURE OF 666 PSI

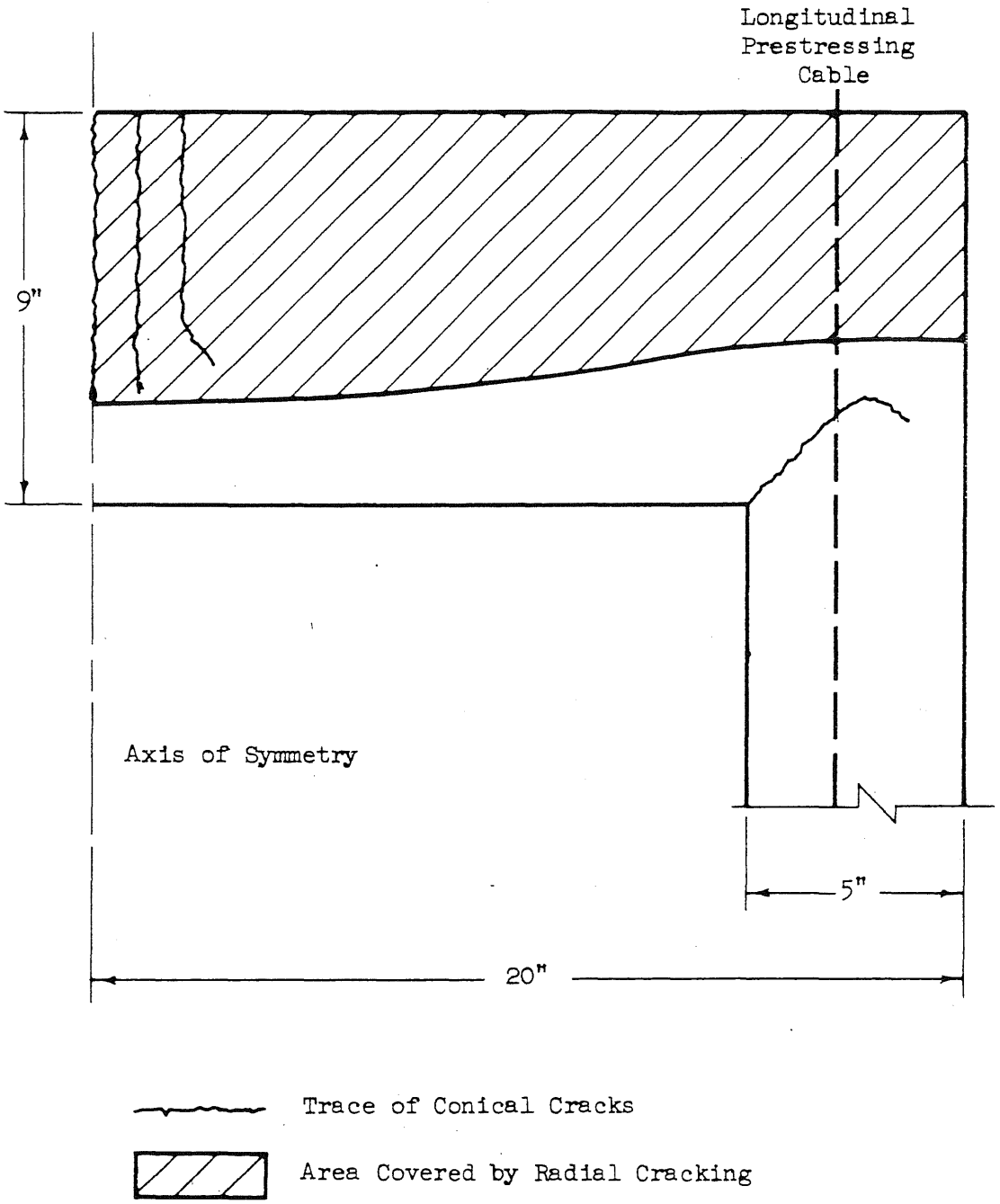

FIG. 37. EXTENT OF CRACKING FOR INTERNAL PRESSURE OF 666 PSI

APPENDIX

EQUILIBRIUM EQUATIONS OPERATORS

The finite difference-type operators presented here characterize the equations of equilibrium for some of the typical mass nodes in the grid. The corresponding equilibrium equations in terms of displacements have been derived according to the procedure outlined in Chapter II. When the numerical analysis is carried out, however, the equilibrium equations are generated within the computer. For the sake of simplicity, the stress nodes involved in these equations are considered to be in the elastic range.

The special notation introduced in the operator shown in Fig. A-5 is as follows,

$$C_c = \frac{1}{\left(\frac{1-\nu}{\lambda_r} + \frac{\nu}{D}\right)}$$

$$A_1 = \frac{1}{2\lambda_r\lambda_z}\left[(1-2\nu) + \frac{\nu^2}{r_i} C_c\right]$$

$$A_2 = \left(\frac{1}{\lambda r} + \frac{1}{2r_i} - \frac{\nu C_c}{2\lambda_r r_i}\right)$$

$$A_3 = - \frac{2E_{st}A_{cp}}{D^2} \frac{A_2}{2r_{i+1}}$$

$$A_4 = - \left(\frac{1}{\lambda_r} - \frac{1}{2r_i}\right)\left(\frac{1-\nu}{\lambda_r} + \frac{\nu}{2r_{i-1}}\right)$$

$$A_5 = - \frac{\nu C_c}{2\lambda_r r_i} \left(\frac{1-\nu}{\lambda_r} - \frac{\nu}{D}\right)$$

The displacement equilibrium equations for the typical interior node are given below for reference.

The equation in the r direction at node (i,j) is:

$$\left[\frac{(1-2\nu)}{2\lambda_z^2}\right] u_{ij+2} + \left\{-\frac{\nu}{2\lambda_z r_i}\right\} w_{ij+2} + \left\{-\frac{1}{2\lambda_z}\left(\frac{1}{\lambda_r} - \frac{\nu}{r_i}\right)\right\} w_{i-1j+1}$$

$$+ \left[\frac{(1-\nu)}{\lambda_r}\left(\frac{1}{\lambda_r} - \frac{1}{2r_i}\right)\right] u_{i-2j} + \left\{\frac{1}{2\lambda_z}\left(\frac{1}{\lambda_r} + \frac{\nu}{r_i}\right)\right\} w_{i+1j+1}$$

$$+ \left[-2\frac{(1-\nu)}{\lambda_r^2} - \frac{(1-\nu)}{r_i^2} - \frac{(1-2\nu)}{\lambda_z^2}\right] u_{ij} + \left\{\frac{1}{2\lambda_z}\left(\frac{1}{\lambda_r} - \frac{\nu}{r_i}\right)\right\} w_{i-1j-1}$$

$$+ \left[\frac{(1-\nu)}{\lambda_r}\left(\frac{1}{\lambda_r} + \frac{1}{2r_i}\right)\right] u_{i+2j} + \left\{-\frac{1}{2\lambda_z}\left(\frac{1}{\lambda_r} + \frac{\nu}{r_i}\right)\right\} w_{i+1j-1}$$

$$+ \left[\frac{(1-2\nu)}{2\lambda_z^2}\right] u_{ij-2} + \left\{\frac{\nu}{2\lambda_z r_i}\right\} w_{ij-2} = 0$$

The equilibrium equation in the z direction at node (i,j) is:

$$\left\{\frac{(1-\nu)}{\lambda_z^2}\right\} w_{ij+2} + \left[-\frac{1}{2\lambda_z}\left(\frac{1}{\lambda_r} - \frac{1}{2r_i}\right)\right] u_{i-1j+1}$$

$$+ \left\{\frac{(1-2\nu)}{2\lambda_r}\left(\frac{1}{\lambda_r} - \frac{1}{2r_i}\right)\right\} + \left[\frac{1}{2\lambda_z}\left(\frac{1}{\lambda_r} + \frac{1}{2r_i}\right)\right] u_{i+1j+1}$$

$$+ \left\{-2\frac{(1-\nu)}{\lambda_z^2} - \frac{(1-2\nu)}{\lambda_r^2}\right\} w_{ij} + \left[\frac{1}{2\lambda_z}\left(\frac{1}{\lambda_r} - \frac{1}{2r_i}\right)\right] u_{i-1j-1}$$

$$+ \left\{\frac{(1-2\nu)}{2\lambda_r}\left(\frac{1}{\lambda_r} + \frac{1}{2r_i}\right)\right\} w_{i+2j} + \left[-\frac{1}{2\lambda_z}\left(\frac{1}{\lambda_r} + \frac{1}{2r_i}\right)\right] u_{i+ij-1}$$

$$+ \left\{\frac{(1-\nu)}{\lambda_z^2}\right\} w_{ij-2} = 0$$

A sample of the equilibrium equations operators is presented in Figs. A-1 through A-8.

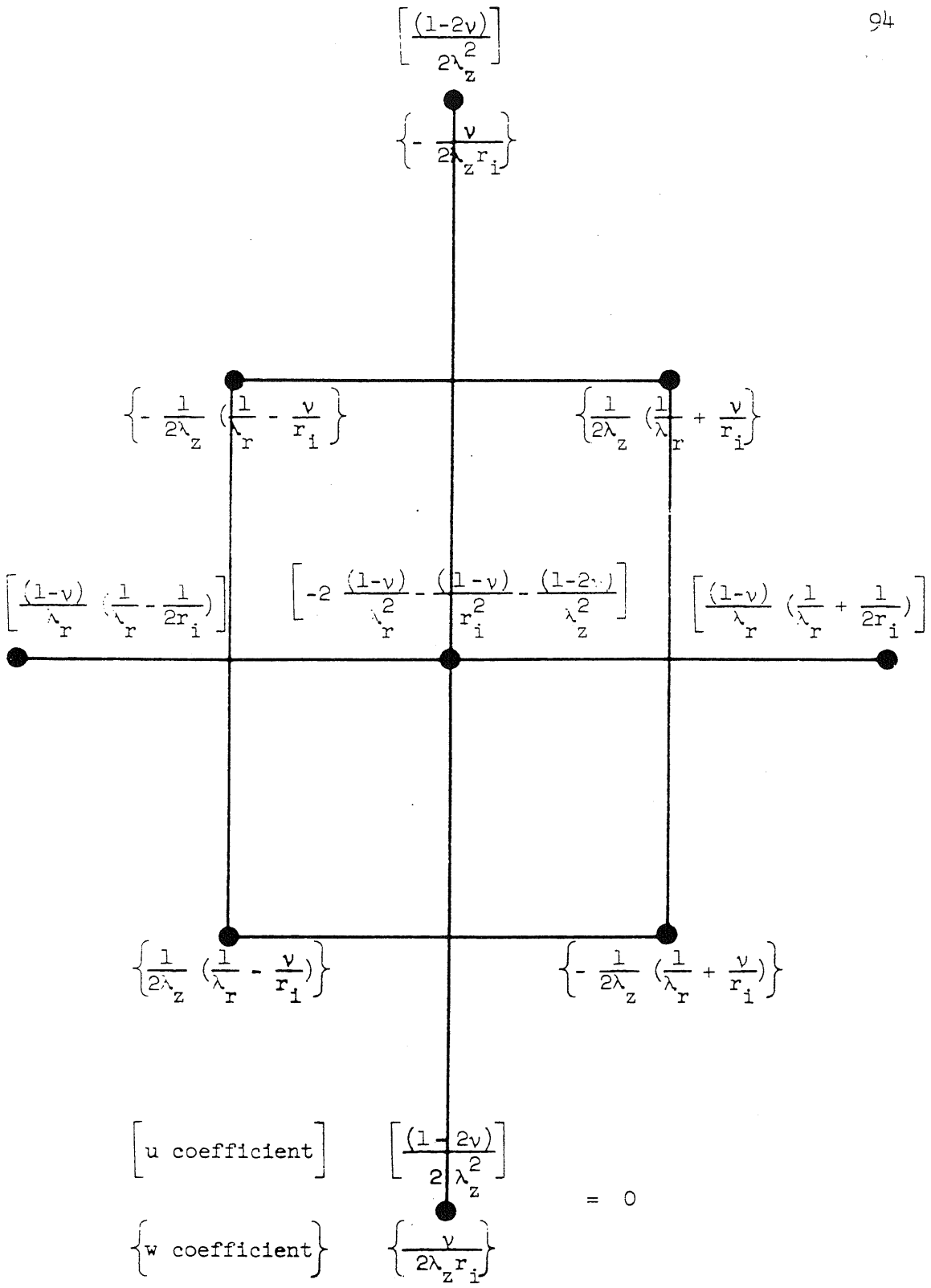

FIG. A-1. R EQUATION OPERATOR FOR A TYPICAL INTERIOR NODE

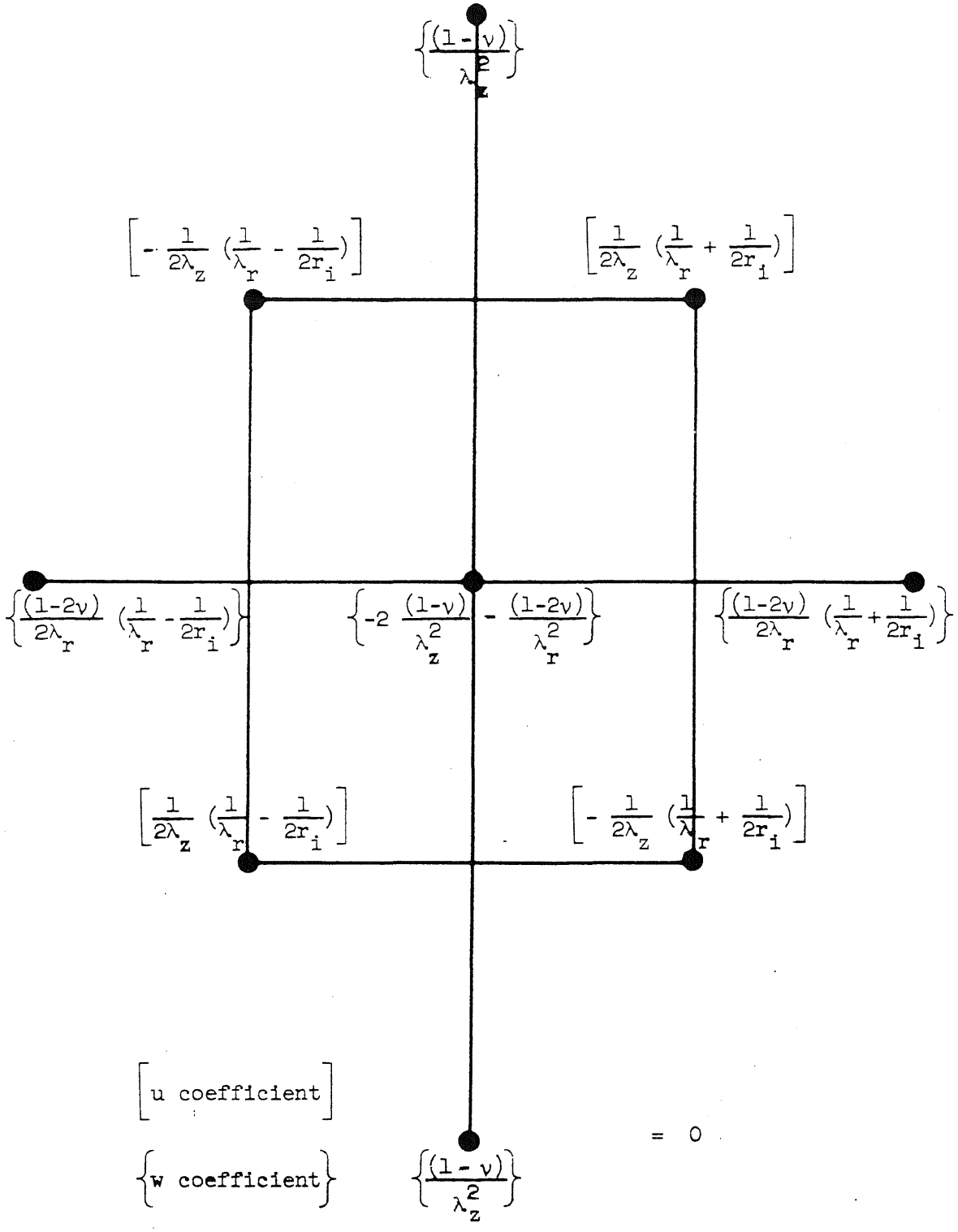

FIG. A-2. Z EQUATION OPERATOR FOR A TYPICAL INTERIOR NODE

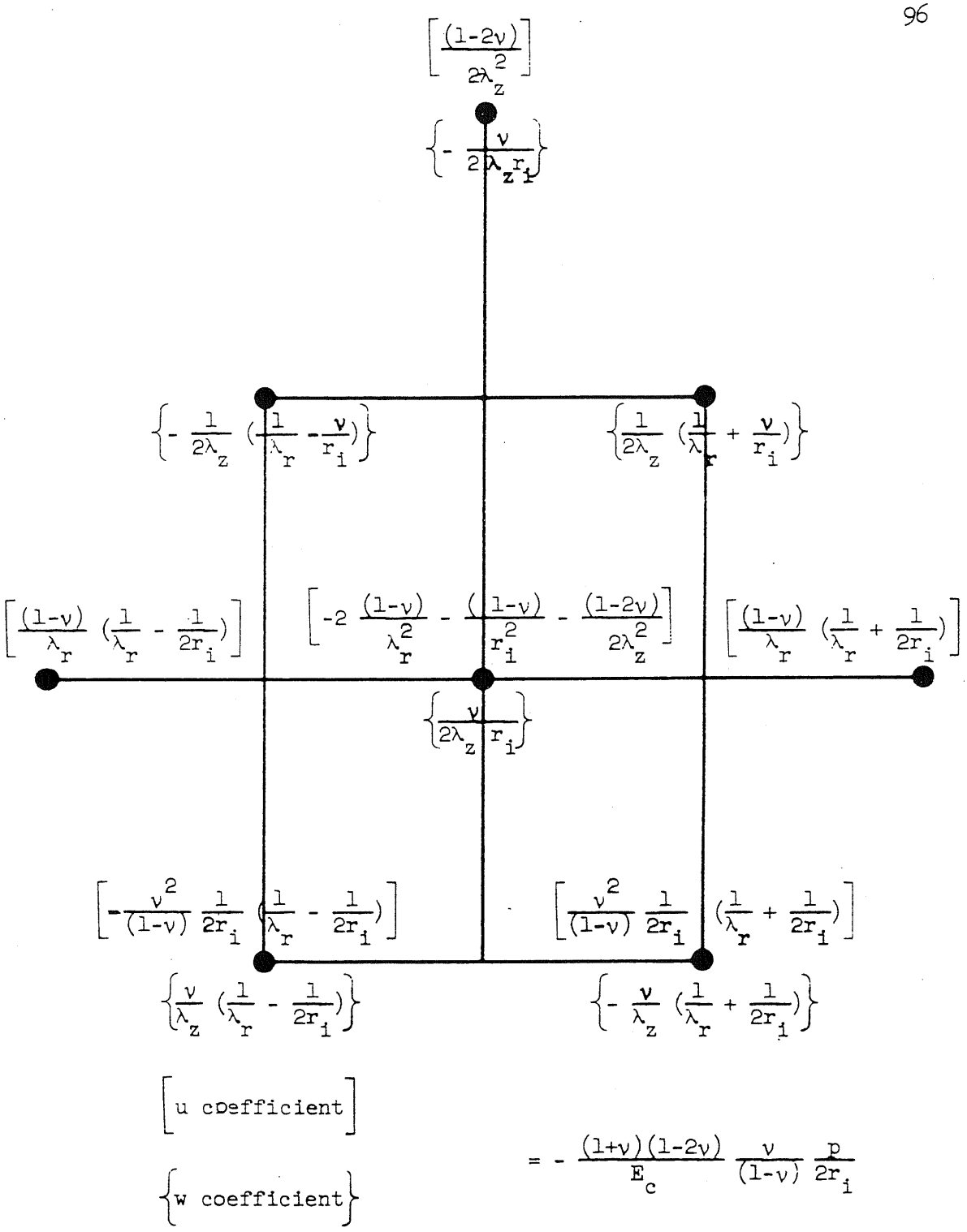

FIG. A-3. R EQUATION OPERATOR FOR A TYPICAL NODE HALF SPACE ABOVE THE LOWER FACE OF THE SLAB

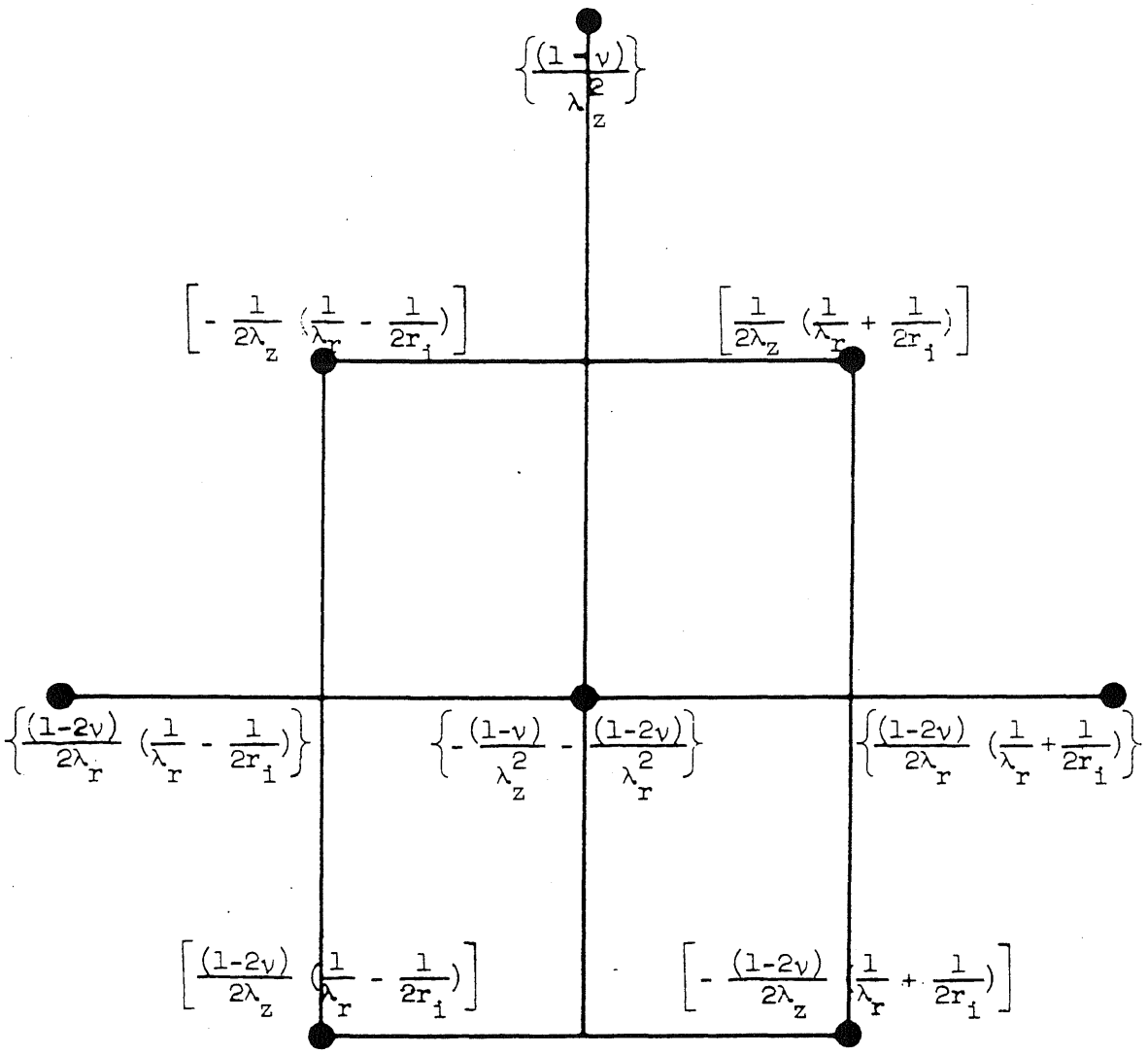

FIG. A-4. Z EQUATION OPERATOR FOR A TYPICAL NODE HALF SPACE ABOVE THE LOWER FACE OF THE SLAB

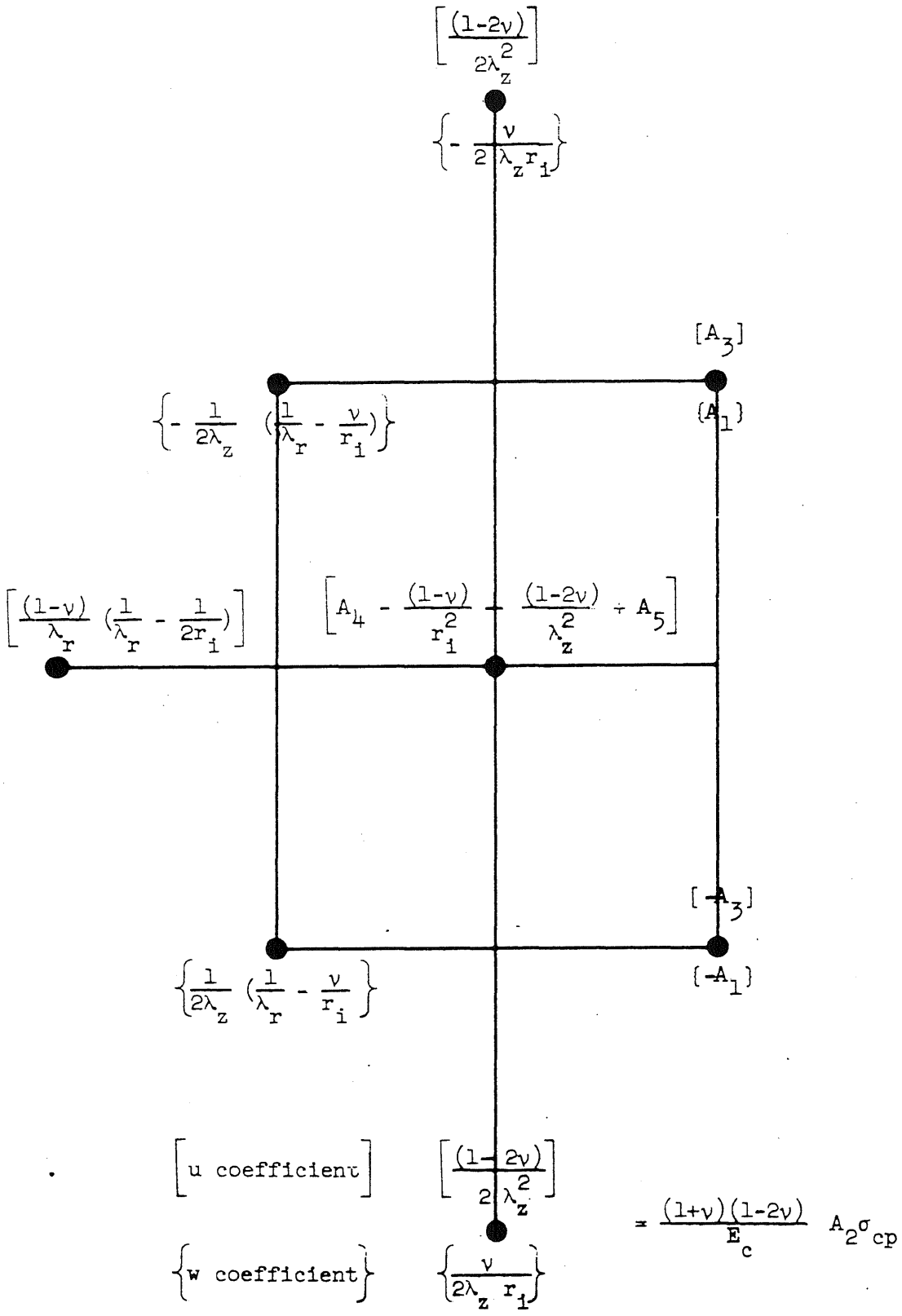

FIG. A-5. R EQUATION OPERATOR FOR A TYPICAL NODE HALF SPACE FROM THE EXTERIOR FACE OF THE WALL

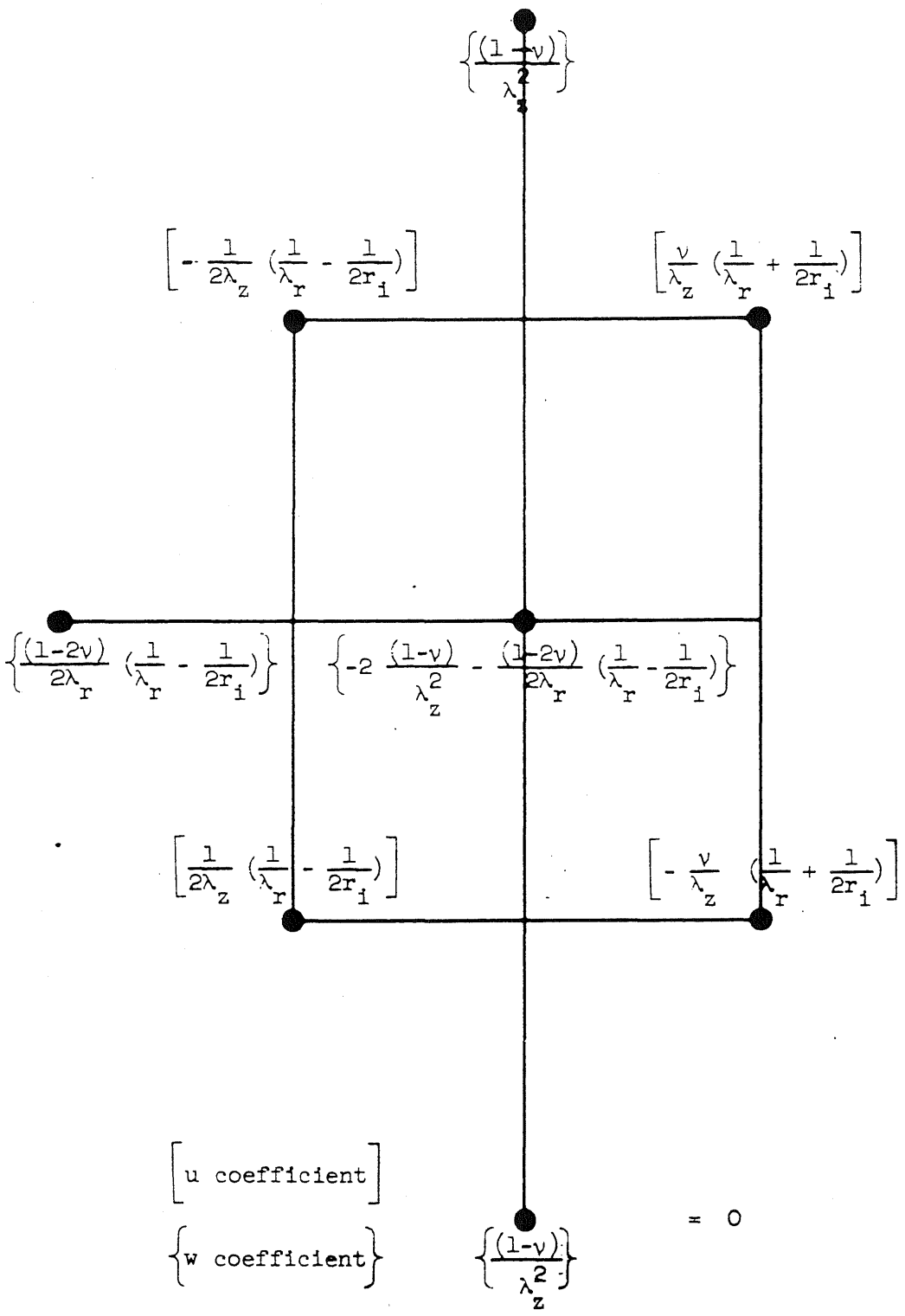

FIG. A-6. Z EQUATION OPERATOR FOR A TYPICAL NODE HALF SPACE FROM THE EXTERIOR FACE OF THE WALL

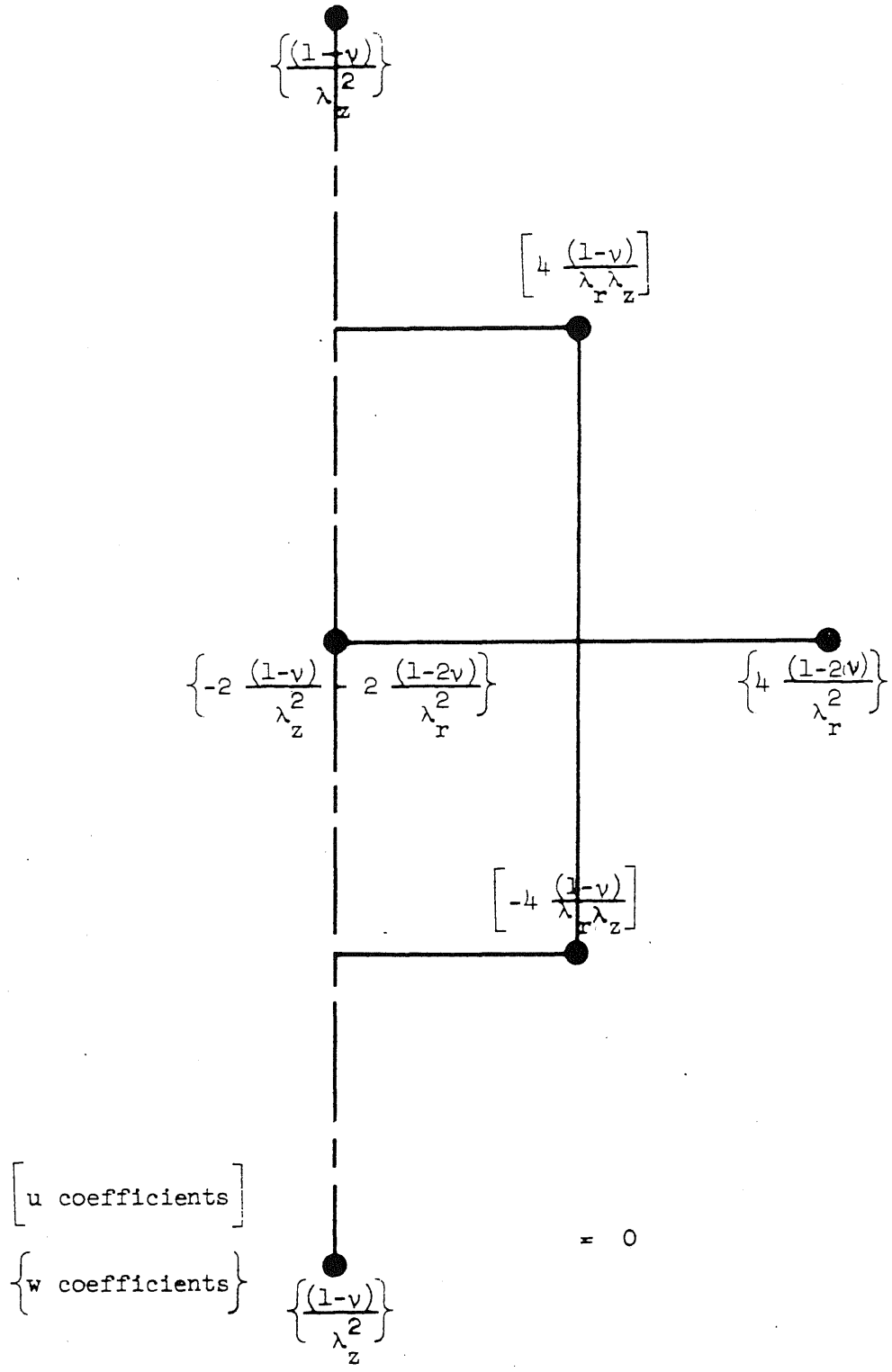

FIG. A-7. Z EQUATION OPERATOR FOR A TYPICAL NODE ON THE AXIS OF SYMMETRY

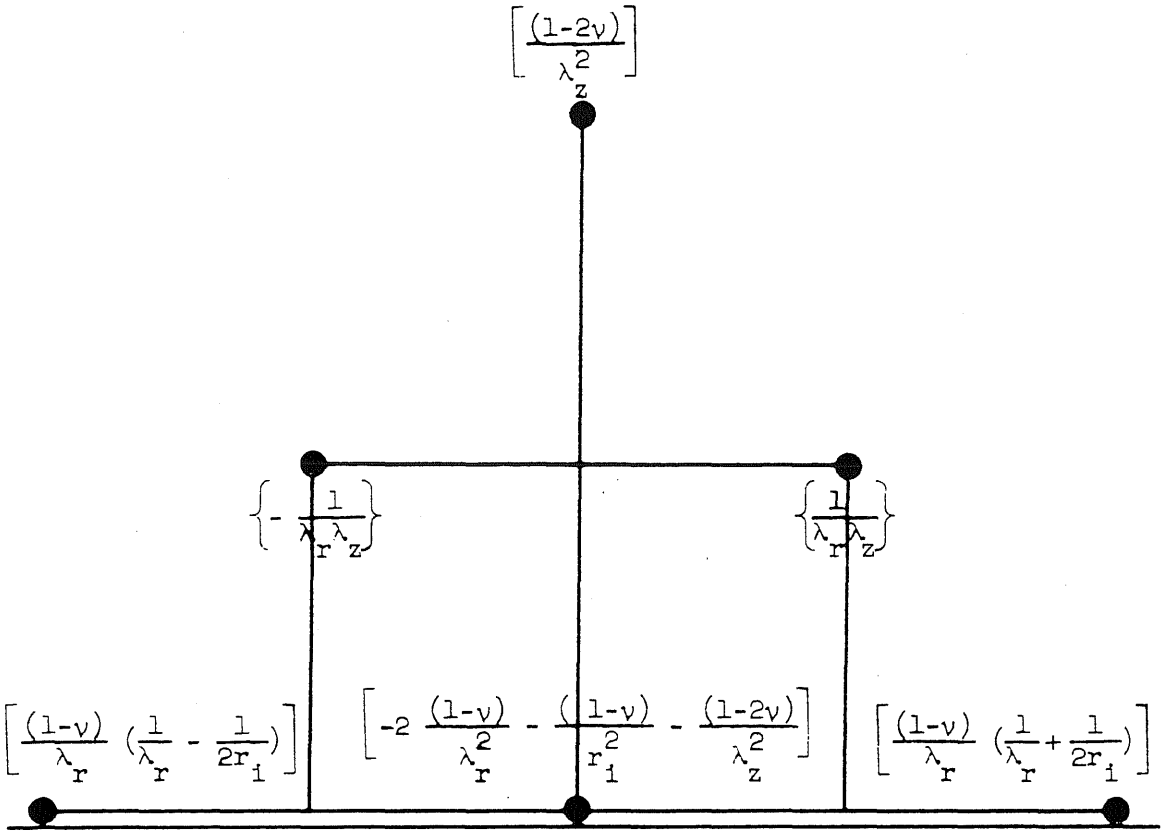

$= 0$

$\left[\text{u coefficient}\right]$

$\left\{\text{w coefficient}\right\}$

FIG. A-8. R EQUATION OPERATOR FOR A TYPICAL NODE AT MID-HEIGHT OF THE VESSEL

arrangement, smaller than the true values since they represent averages over the associated areas.

Figure 17 shows the grid node arrangement around the re-entrant corner. The strain-displacement relations at the corner need not be reformulated. However, some of the equilibrium equations for the neighboring mass elements are affected.

If the radial direction equilibrium equation for mass node 3 is taken as an example, it can be seen that a special situation develops at the face containing stress node b. The typical equilibrium equation in the r direction,

$$\frac{\sigma_r^a - \sigma_r^b}{\lambda_r} + \frac{\tau_{rz}^c - \tau_{rz}^d}{\lambda_z} + \frac{\frac{1}{2}(\sigma_r^a + \sigma_r^b) - \sigma_\theta^{ij}}{r_i} = 0 \qquad (4.15)$$

can still be used provided σ_r^b is redefined, in such a way that the resulting force at face b equals the sum of the resultants of the applied internal pressure p and the stress at b, integrated over the associated areas. In this case, this condition means that σ_r^b, in the preceeding equation, needs to be replaced by:

$$\bar{\sigma}_r^b = \frac{1}{2}(p + \sigma_r^b) \qquad (4.16)$$

because p and σ_r^b each act on half of the face area of node b.

The equilibrium equation in the z direction at mass node 2 is derived in a similar manner.

V. COMPUTATIONAL TECHNIQUE

5.1. The Numerical Problem

The numerical method, used in this study, is based on a discrete model which has been shown to be mathematically consistent with the continuum. This model reduces the continuum to a system which is completely defined by a finite number of variables. The formulation of the problem is obtained directly from the fundamental principles of mechanics and basic behavior of materials. Such a formulation leads to a system of linear algebraic equations which are intuitively meaningful. The solution of such a system of equations can be conveniently obtained by the use of digital computers.

The IBM 360-50/75 system operated by the Department of Computer Science of the University of Illinois has been used both in generating and solving the discrete equations of equilibrium.

Before going into specifics on the utilization of this method, a brief general description of the procedure is given.

5.2. Computational Procedure

Since the full range of vessel behavior includes a nonlinear phase, the solution of the problem is carried out incrementally, in a piecewise linear fashion. This permits a re-evaluation of the stiffness coefficients and load terms each time the discrete system representing the continuum is modified. It becomes necessary to regenerate some of the governing equations when localized cracking is initiated, or when the loading is incremented. Each equilibrium equation is expressed in

terms of displacements, by a sequential substitution of stress-strain and stress-displacement relationships into the original equation.

Concrete at a deformable node is considered to have cracked if the average tensile strain in any direction at that node has reached a certain limiting value. The formation of a crack is followed by a re-evaluation of the stiffness coefficients of the discrete system, in such a way that the material at the cracked node exhibits orthotropical properties consistent with no tensile resistance in a direction perpendicular to the crack.

After the crack has been introduced the energy released from the node at cracking is redistributed throughout the network in order to re-establish the equilibrium of the system. A close surveillance of the strain condition, at the deformable nodes, is kept so that new nodes that may in turn crack as a consequence of previous cracking can be treated in a similar manner before proceeding. This repetitive process is continued until the crack ceases to propagate without increase in load. Once the crack is arrested, the internal pressure is increased until a new node reaches the limiting value assumed as the cracking strain criterion.

5.3. Solution of the Equations

As indicated above, the resulting system of algebraic equilibrium equations in u and w displacements are equivalent to the finite difference discretization of the partial differential equations governing the continuum.

These differential equations can be reduced to two independent, second order, linear, partial differential equations of the elliptic type in u and w. This being the case, and knowing that the exact boundary-value problem possesses a solution, the approximate discrete problem produces results that, as the grid is continually refined, tend to the exact solution.[8,12]

In matrix form, the system of algebraic equations is expressed by:

$$[M]\{d\} = \{P\} \tag{5.1}$$

where {d} is the displacement vector; [M] the coefficient matrix formed by the equilibrium equations, and {P} is the vector corresponding to the load terms.

In expanded form:

$$\begin{bmatrix} & \diagdown & \\ \diagdown & & \diagdown \\ & \diagdown & \end{bmatrix} \begin{Bmatrix} u_1 \\ w_1 \\ u_2 \\ w_2 \\ \vdots \\ u_k \\ w_k \\ \vdots \\ u_n \\ w_n \end{Bmatrix} = \begin{Bmatrix} P_{r1} \\ P_{z1} \\ \vdots \\ P_{rk} \\ P_{zk} \\ \vdots \\ P_{rn} \\ P_{zn} \end{Bmatrix} \tag{5.2}$$

where the subscript on the displacements represents the sequential order of the displacement nodes, n is the number of displacement nodes in the grid, and P_{rk} and P_{zk} are the load terms in the equations for the mass node of location k.

Since only a few displacements, defined at the displacement nodes surrounding the element, are present in each one of the equations, Matrix [M] is a tightly banded matrix. With the L-shaped geometry of the cross section of the vessel, the minimum band width is achieved by employing a diagonal numbering system as opposed to column or row numbering. This reduction decreases considerably the space required for the solution of the equations in the computer. Because the coefficients along the diagonal are dominant, the Gauss-Seidel method of solution is used with advantage.

5.4. Extrapolation to Crack Occurrence

As discussed in Chapter III, two basic types of cracks, radial and conical, can occur in the vessel. The occurrence of cracking is initiated when a principal strain exceeds the cracking criterion.

The condition of axi-symmetry, which results in $\gamma_{r\theta}$ and $\gamma_{\theta z}$ being identically zero, establishes ϵ_θ as one of the principal strains. The other principal strains are obtained from the direct and shear strains in plane rz. The maximum principal strain in plane rz is:

$$\epsilon_1 = \frac{1}{2}\left[\epsilon_r + \epsilon_z + \sqrt{(\epsilon_r-\epsilon_z)^2 + \gamma_{rz}^2}\right] \qquad (5.3)$$

The two strains, ϵ_θ and ϵ_1, indicate whether a stress node is in an elastic or a cracked condition.

After a crack has formed at the location of a stress node, the related stiffness coefficients need to be changed to reflect the presence of the crack.

In order to advance from a certain loading stage to the initiation of a new crack, it is necessary to determine the internal pressure level at which this new crack develops. Let ϵ_r^{pr}, ϵ_z^{pr}, ϵ_θ^{pr} and γ_{rz}^{pr} refer to the strain state at the conclusion of all previous cracking and prior to the new pressure increment and $\Delta\epsilon_r$, $\Delta\epsilon_z$, $\Delta\epsilon_\theta$ $\Delta\gamma_{rz}$ indicate the strain increments caused by an increase Δp of the internal pressure. The elastic strains at the moment of cracking are:

$$\begin{aligned}
\epsilon_r^{cr} &= \epsilon_r^{pr} + F\,\Delta\epsilon_r \\
\epsilon_z^{cr} &= \epsilon_z^{pr} + F\,\Delta\epsilon_z \\
\epsilon_\theta^{cr} &= \epsilon_\theta^{pr} + F\,\Delta\epsilon_\theta \\
\gamma_{rz}^{cr} &= \gamma_{rz}^{pr} + F\,\Delta\gamma_{rz}
\end{aligned} \tag{5.4}$$

where F is the factor that scales the pressure increment Δp to the level that will cause the next crack to form.

If the crack is radial, the cracking condition is:

$$\epsilon_\theta^{cr} = \epsilon_{cr} \tag{5.5}$$

where ϵ_{cr} is the strain value selected as the cracking criterion. In this case F, as found from Eq. 5.5, is given by:

$$F = \frac{\epsilon_{cr} - \epsilon_{\theta}^{pr}}{\Delta\epsilon_{\theta}}$$

On the other hand, if the crack is conical, ϵ_1 is equated to ϵ_{cr} and the following second degree equation in F is obtained:

$$\epsilon_{cr} = \frac{1}{2}\left[(\epsilon_r^{pr} + \epsilon_z^{pr}) + F(\Delta\epsilon_r + \Delta\epsilon_z) + \sqrt{\{(\epsilon_r^{pr}-\epsilon_z^{pr})^2 + F(\Delta\epsilon_r-\Delta\epsilon_z)\}^2 + (\gamma_{rz}^{pr} + F\,\Delta\gamma_{rz})^2}\right] \tag{5.6}$$

The roots from this equation are evaluated according to the particular strain situation existing at the node being investigated.

Scaling factors F are computed at all the stress nodes in the network that remain in elastic condition in either one or both of the principal directions in which the node can crack. The lowest F value corresponds to the initiation of the next crack.

5.5. Crack Propagation

The formation of a crack is accompanied by a local release of elastic energy. The energy is absorbed by the rest of the continuum through a natural process of redistribution of stresses and strains.

This natural process is simulated in the model by reanalyzing the modified discrete system that includes the new crack. Once the balance of energy is re-established, it is necessary to review the strain state throughout the vessel. If additional cracking is in evidence, i.e., if the crack has propagated without an increase in

loading the artificial redistribution process is repeated. This procedure is continued until the crack ceases to propagate.

In the early stages of loading, crack propagation is not likely to occur. The load is increased incrementally from the formation of one crack to the next. But, when cracking has become wide spread, a succession of cracks forms nearly every time the internal pressure is increased.

VI. NUMERICAL RESULTS

6.1. General Remarks

A sample problem chosen to demonstrate the applicability of the lumped parameter model is presented and discussed in this chapter. This sample problem corresponds to one of the small-scale vessels tested at the Structural Laboratory of the University of Illinois. The analytical results obtained here are compared with the experimental data.

Four stages of loading have been selected to illustrate the behavior of the sample vessel throughout the loading process. They correspond to: (a) prestressing alone (zero internal pressure), (b) the state just prior to the formation of the first crack, (c) an intermediate stage in the inelastic range and (d) the load level at the time the analysis was terminated. The case of the unprestressed vessel subjected to internal pressure is also included and presented for reference.

6.2. The Sample Problem

The dimensions, prestressing conditions, and material properties assumed for the sample problem were chosen to correspond to the dimensions and properties of one of the vessels tested at the University of Illinois. The vessel's external diameter, D, is 3 ft. 4 in. and its total height, H, is 6 ft. 8 in. The slab has a depth, t_s, of 9 inches. The cylinder has a wall thickness, t_c, of 5 inches.

The vessel is prestressed longitudinally by 30 high-strength steel ungrouted cables, 0.151 sq. in. in cross-sectional area, loaded

initially with 25.2 kips each. These ungrouted prestressing cables are placed at a distance of 3 in. from the outside surface of the wall. The circumferential prestressing is provided by a single cable with a cross-sectional area of 0.029 sq. in. The cable is helically wrapped around the cylindrical body at a spacing of 0.333 in.

The elastic constants for the materials have been determined experimentally. The Young's modulus and Poisson's ratio of the concrete are $E_c = 4.3 \times 10^6$ psi and $\nu = 0.15$, and the Young's modulus of the steel is $E_{st} = 28 \times 10^6$. There is a scarcity of information pertinent to the cracking strain of concrete under multiaxial states of stress. The value adopted for the cracking strain criterion, $\epsilon_{cr} = 0.00015$, was selected on the basis of the strains measured during the test of the small scale vessel.

A 6 x 41 grid is used to represent the cylindrical wall, while a 9 x 16 grid is employed to approximate the slab. Since the analysis is continued until a substantial portion of the vessel is in cracked state, the grid layout was selected to place a stress node at the re-entrant corner.

6.3. Behavior of the Vessel

The significant behavior of the pressure vessel, its ductility, is best discussed with the aid of a load-displacement diagram, Fig. 18. This figure shows the relationship of the longitudinal displacement at the center of the slab versus pressure. The center displacement is measured on the upper face of the slab at the axis of symmetry. The displacements shown are measured from the vessel already deformed by

the prestressing forces. That is, the origin represents the case of a fully prestressed vessel under zero internal pressure. The rationale for this choice is that the experimental tests have the fully pre-stressed vessel as their origin.

The vessel behaves linearly as the internal pressure is increased from 0 to 450 psi. Point B identifies the formation of the first crack as detected in the lumped parameter model. The first crack is a conical crack at the re-entrant corner. Since the stresses at the re-entrant corner of the vessel are highly concentrated while the stresses and strains that the model computes are average values, it is clear that in the actual vessel this corner crack is initiated slightly earlier in the loading process. Because the stiffness loss due to an incipient crack at the re-entrant corner is very small, the analytical and experimental results appear in perfect agreement at this point.

From point B on, new cracks form in succession as the internal pressure is increased. Associated with the spreading of cracking the general stiffness of the vessel decreases and the straight line that characterizes elastic behavior transforms into a curve of decreasing slope.

The analytical broken line extending from B to D is composed of slanted and horizontal segments. A slanted segment corresponds to the linear behavior of the modified network nodal system which includes all those cracks that have formed up to that time. This linear behavior prevails until a new crack forms. When the new crack is incorporated and the energy released is redistributed into the system a larger deformation corresponds to the same load level. The line joining the

points that represent the deformations of the system just before and just after the new crack is, then, horizontal. This horizontal line becomes automatically extended when additional new cracks are formed solely as a consequence of the energy released from the last node to crack.

This terrace pattern is obviously due to the finite piece-wise approach to the problem of cracking. The heavy line traced from B to D provides an approximation to the continuous behavior of the structure.

A dashed line has been traced through the experimental data points plotted. A comparison between the analytical and experimental results reveals that although there is excellent agreement in the elastic and early inelastic zones, the analytical curve departs from the experimental curve as cracking progresses. The small discrepancy is in part the product of the selection of the cracking criterion. Conceivably, the two curves can be brought into near coincidence by adjusting the cracking criterion to a slightly higher value. Nevertheless, the similarity between the slopes or these two curves is highly significant in assessing the usefulness and potentials of the method of analysis.

Figure 19 provides a comparison between the longitudinal displacements computed across the upper face of the slab for three levels of loading and the corresponding experimental values. At $p = 450$ psi, when the first crack develops, there is a perfect agreement at the center; little can be said about the rest of the values because of the limitations of the experimental equipment when dealing with very

small deformations. A much better general agreement can be observed between the other two pairs of curves. Because of the uncertainty in the cracking criterion adopted the analytical values for p = 580 psi and p = 666 psi are compared to the "equivalent" experimental results for p = 600 psi and p = 700 psi.

Figures 20 through 22 illustrate the state of stress that would be caused by the application of internal pressure to an unprestressed vessel. For this purpose, the material is considered to behave elastically. Figure 20 shows the radial stresses prevailing at the levels of the upper and lower faces of the slab. Similarly, the longitudinal stresses along the external and internal surfaces of the cylinder are presented in Fig. 22. The circumferential stresses in both the slab and the cylinder are given in Fig. 21. The concentration of high tensile stresses and strains at the re-entrant corner is clearly visible in all the figures. Other regions of interest are the central portions of the slab, both near the upper and the lower surfaces. In the upper region, tensile stresses prevail in the radial and circumferential directions. The compressive stresses in the lower region, that result from bending of the slab, are greatly increased when the vessel is subjected to the compression field produced by the prestressing systems.

As mentioned above, the first crack is formed at the re-entrant corner. Figures 23 through 27 illustrate the state of stresses and strains that determine the initiation of such a crack. Especially significant are the maximum strain trajectories in rz plane.

The cracks that develop after the corner crack are mainly radial. Some conical cracks naturally form in the neighborhood of the axis of symmetry. All this subsequent cracking occurs in the central upper region of the slab. As the load increases, the radial cracks extend rather quickly toward the outside of the cylinder, and more slowly downward from the upper face of the slab. After the radial cracking in the upper region of the slab has become widespread, the crack at the re-entrant corner propagates toward the outside of the wall. This conical crack, which initiates at approximately 45° from the horizontal, flattens out slowly as it progresses toward the longitudinal prestressing cables. Figures 28 through 33 characterize the vessel at this cracking stage. Figure 33, in particular, describes graphically the extent and nature of cracking. Since the radial cracks have propagated from the axis of symmetry all the way to the external surface of the cylinder, the circumferential stresses at the upper surface of the slab are zero. This is shown in Fig. 29.

If the pressure continues to be increased, the radial cracks continue propagating downward toward the bottom of the slab. The conical crack at the re-entrant corner, after crossing the longitudinal prestressing tendon, changes to a negative slope and continues to develop toward the external surface of the wall. The analysis is terminated when the failure mechanism appears clearly defined. For the sample vessel under study, this occurs at $p = 670$ psi. Figures 34 through 37 illustrate the stress and strain states at the stage when the analysis was stopped. Since cracking is general throughout better than the upper 60 percent of the slab and the crack at the re-entrant corner

separates the wall from the slab, the load is being carried primarily by an inverted highly compressed dome supported essentially by the longitudinal prestressing cables at the distribution plates. This situation is depicted quite clearly by the various figures that characterize this loading state.

The final failure mechanism can be readily identified from the analysis of the state of cracking illustrated by Fig. 37. As the crack initiated at the re-entrant corner propagates toward the outside of the wall, the amount of rotational constraint of the slab decreases. The slab finally fails in bending as a simply supported circular concrete plate. Pie-shaped sectors open up when the radial cracks reach the bottom of the slab. These sectors rotate about the crack across the wall.

VII. CONCLUSIONS AND RECOMMENDATIONS FOR FURTHER STUDY

A discrete element method for the elastic and inelastic analysis of cylindrical prestressed concrete reactor vessels has been developed. This method utilizes a lumped parameter model based on the theory of finite differences. The model provides good estimates of the displacements, stresses and strains that result throughout the body of the vessel at the various stages in loading, beginning with the prestressing and continuing to near final failure of the vessel.

The results obtained from the analysis indicate that an elastic-fracture approach to the inelastic properties of concrete is sufficient to predict the mode of failure of a cylindrical prestressed concrete pressure vessel with flat ends. Although considerations of plasticity can in principle be included, there is evidence that by so doing no major gain is obtained in describing the behavior of the vessel. For the sake of completeness, it is desirable to incorporate a general failure theory of concrete at the appropriate time in the future when such a theory has been developed.

This lumped parameter method can be employed to determine which mode of failure results for a vessel with a given combination of parameters, general dimensions and prestress. From this view point, the method is an invaluable tool for the design of PCRV's, where a ductile mode of failure is required.

The analytical results obtained by the use of the method compare favorably with experimental results obtained from tests on small-scale vessels at the University of Illinois.

The lumped parameter study presented here represents in effect the equivalent to an experimental test of the vessel. When interacted with the actual experimental study the combination provides a much clearer explanation of the actual behavior of the vessel.

Pressure vessels with openings can be investigated by means of a three-dimensional discrete model. The lumped parameter model used here is implicitly a three-dimensional system. With the conditions of axi-symmetry present in the problem it was possible to reduce the model to a two-dimensional network. Although a major programming effort would be involved in employing the model in its three-dimensional form, the basic approach employed here does not need to be altered in order to make such an extension.

The effect of thermal gradients across the walls of a vessel is an important problem that can be investigated in connection with nuclear reactor technology.

As investigations develop the behavior of concrete under a multiaxial state of stress, their results should be incorporated in the analysis of PCRV's. There is a particularly urgent need for information pertaining to the cracking of concrete under biaxial and triaxial states of stress. Until such investigations are conducted, the influence of various assumptions on concrete behavior can be studied with the model. From this study, it can be determined how sophisticated a failure theory need to be to provide an accurate approximation to the behavior of prestressed concrete pressure vessels.

LIST OF REFERENCES

1. Ang, A. H. S. and Rainer, J. H., "Model for Wave Propagation in Axi-Symmetric Solids," Journal of the Engineering Mechanics Division, ASCE, Vol. 90, No. EM2, April 1964.

2. Bresler, B. and Pister, K. S., "Strength of Concrete Under Combined Stresses," Proceedings of the American Concrete Institute, Vol. 55, No. 3, September 1958.

3. Brown, A. H. et al., "The Design and Construction of Prestressed Concrete Pressure Vessels with Particular Reference to Oldbury Nuclear Power Station," Proceedings of the Third International Conference on the Peaceful Uses of Atomic Energy, Geneva, Vol. 8, United Nations, New York, 1964.

4. Chang, G. C., "Interaction of Plane Stress Waves with Lined or Unlined Tunnels in Elastic-Perfectly Plastic Media," Ph.D. Thesis, University of Illinois, 1966.

5. Chinn, J. and Zimmerman, R. M., "Behavior of Plain Concrete Under Various High Triaxial Compression Loading Conditions," Technical Report No. WL TR 64-163, Air Force Weapons Laboratory, Kirtland Air Force Base, New Mexico.

6. Crose, J. G. and Ang, A. H. S., "A Large Deflection Analysis Method for Elastic-Perfectly Plastic Plates," Civil Engineering Studies, Structural Research Series No. 323, University of Illinois, June 1967.

7. Fedorkiw, J. P., "Analysis of Reinforced Concrete Frames with Filler Walls," Ph.D. Thesis, University of Illinois, 1968.

8. Forsythe, G. E. and Wasow, W. R., "Finite Difference Methods for Partial Differential Equations," John Wiley and Sons, New York, 1960.

9. Gamble, W. L., et al, "A Study of Launch Facility Closures," SAMSO-TR-67-15, U.S.Air Force Contract No. AF04(694)-796, University of Illinois, November 1967.

10. Gaus, M. P., "A Numerical Solution for the Transient Strain Distribution in a Rectangular Plate with a Propagating Crack," Civil Engineering Studies, Structural Research Series No. 182, September 1959.

11. Harper, G. N. and Ang, A. H. S., "A Numerical Procedure for the Analysis of Contained Flow Problems," Civil Engineering Studies, Structural Research Series No. 266, University of Illinois, June 1963.

12. Hildebrandt, F. B., Methods of Applied Mathematics, 4th ed., Prentice Hall, New Jersey, 1958.

13. Marsh, R. O. and Rockenhauser, W., "Prestressed Concrete Structures for Large Power Reactors," Mechanical Engineering, ASME, Vol. 88, No. 7, July 1966.

14. Martinez-Marquez, A., "General Theory for Thick Shell Analysis," Journal of the Engineering Mechanics Division, ASCE, Vol. 92, No. EM2, December 1966.

15. Mohraz, B. and Schnobrich, W. C., "The Analysis of Shallow Shells by a Discrete Element System," Civil Engineering Studies, Structural Research Series No. 304, University of Illinois, March 1966.

16. Newman, K., "Criteria for the Behavior of Plain Concrete Under Complex State of Stress," International Conference on the Structure of Concrete, Paper F1, September 1965.

17. Otter, J. R. H., Cassell, A. C. and Hobbs, R. E., "Dynamic Relaxation," Proceedings of the Institution of Civil Engineers, Vol. 35, December 1966.

18. Otter, J. R. H., "Computations for Prestressed Concrete Reactor Pressure Vessels Using Dynamic Relaxation," Nuclear Structural Engineering, Vol. 1, No. 1, 1965.

19. Rashid, Y. R., "Analysis of Asymmetric Composite Structures by the Finite Element Method," Short Course on Prestressed Concrete Nuclear Reactor Structures, Engineering Extension and the College of Engineering, University of California, Berkeley, March 1968.

20. Rashid, Y. R. and Rockenhauser, W., "Pressure Vessel Analysis by Finite Element Techniques," United States Report GA-7810, General Atomic, February 1967.

21. Richart, F. E., Brandtzaeg, A. and Brown, R. L., "A Study of the Failure Mechanism of Concrete Under Combined Stresses," Civil Engineering Studies, Structural Research Series No. 185, 1928.

22. Schnobrich, W. C., "A Physical Analogue for the Analysis of Cylindrical Shells," Ph.D. Thesis, University of Illinois, 1962.

23. Shoeb, N. A. and Schnobrich, W. C., "The Analysis of Elasto-Plastic Shell Structures," Civil Engineering Studies, Structural Research Series No. 324, University of Illinois, August 1967.

24. Tan, P. T., "Prestressed Concrete in Nuclear Pressure Vessels: A Critical Review of Current Literature," ORNL-4227, Oak Ridge National Laboratory, U. S. Atomic Energy Commission, May 1968.

25. Timoshenko, S. and Goodier, J. N., Theory of Elasticity, 2nd ed., McGraw-Hill Co., New York, 1951.

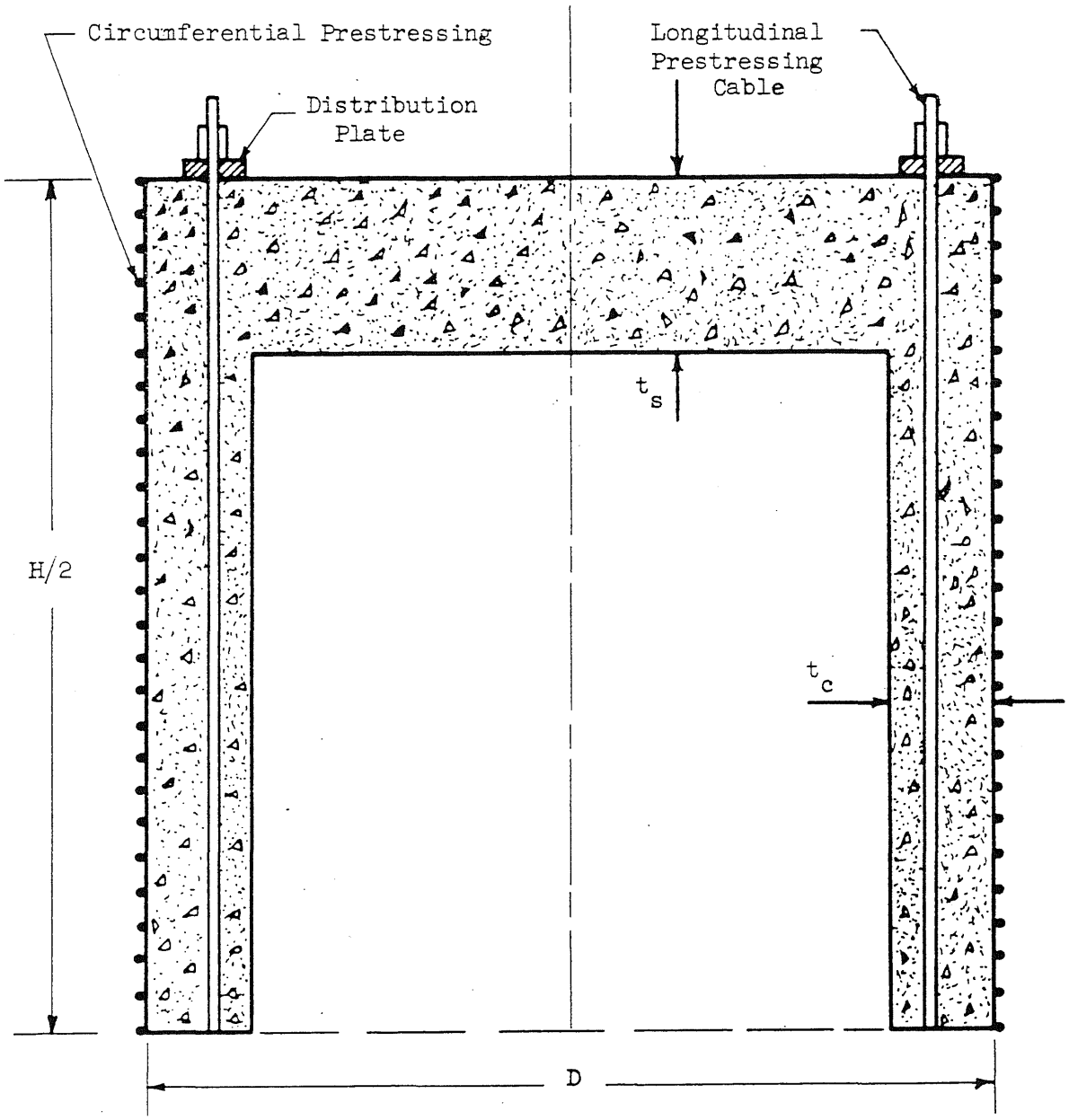

FIG. 1. LONGITUDINAL SECTION THROUGH HALF OF THE VESSEL

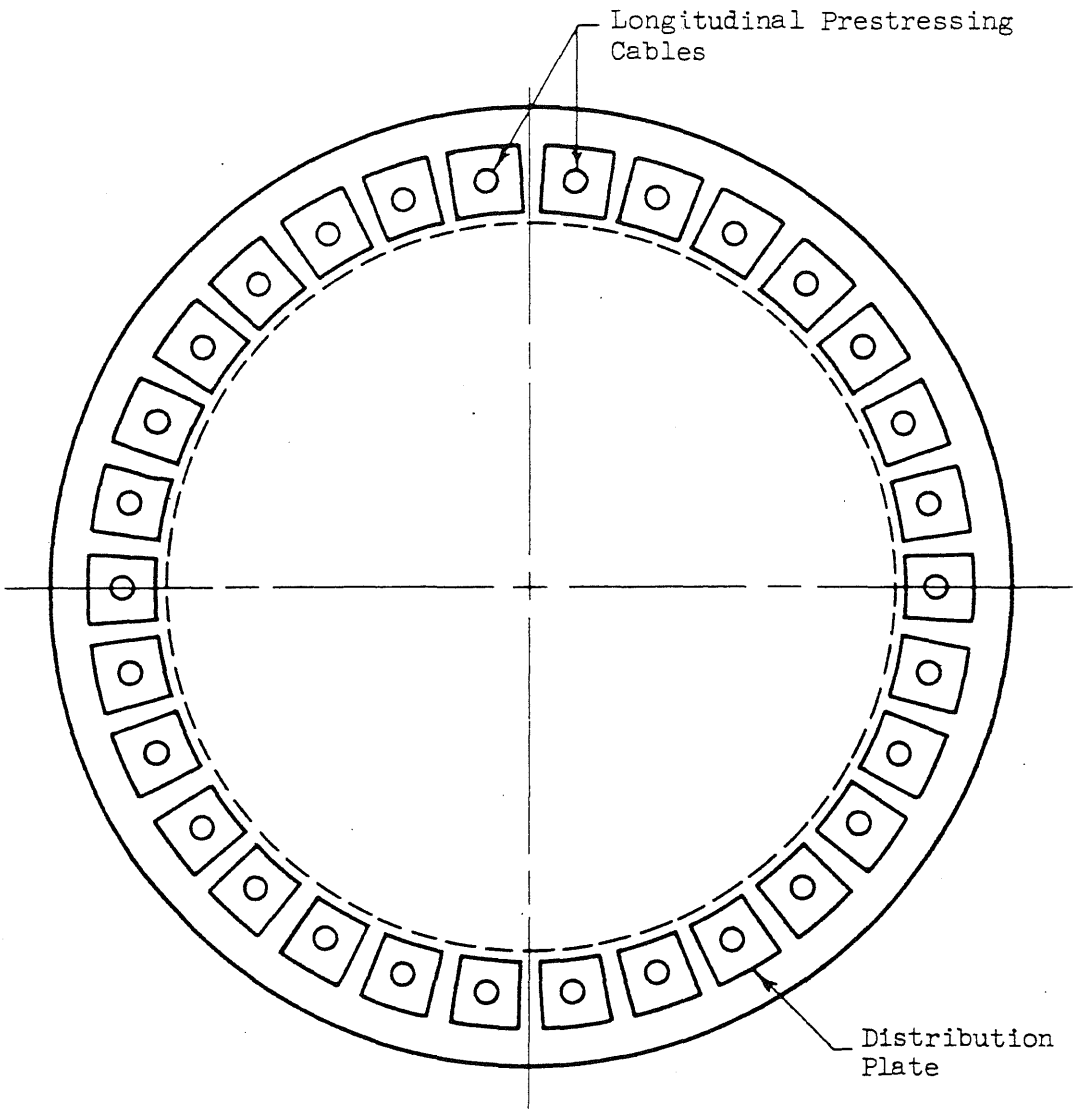

FIG. 2. PLAN VIEW OF END SLAB

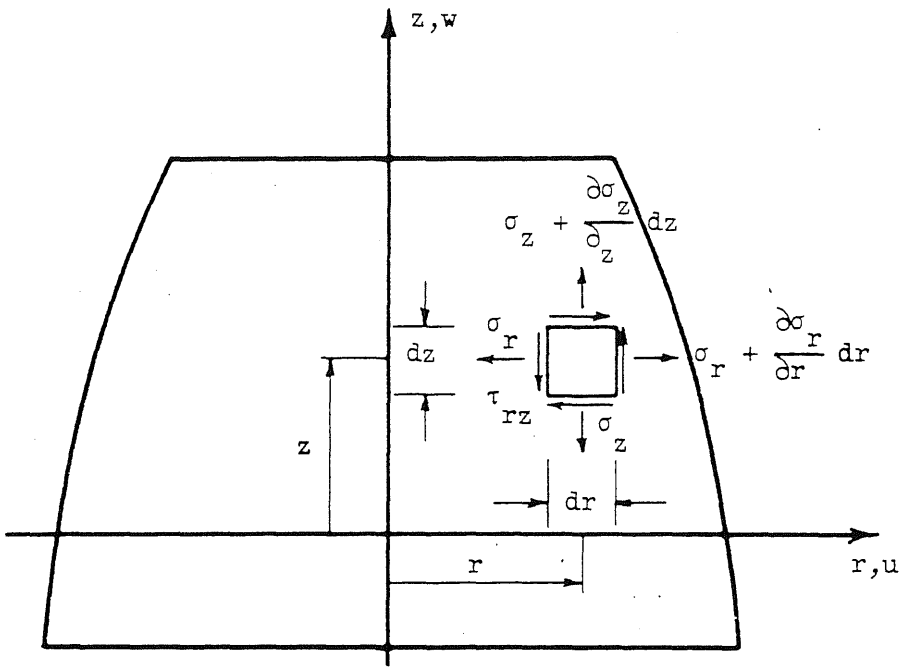

a. Longitudinal Cross Section

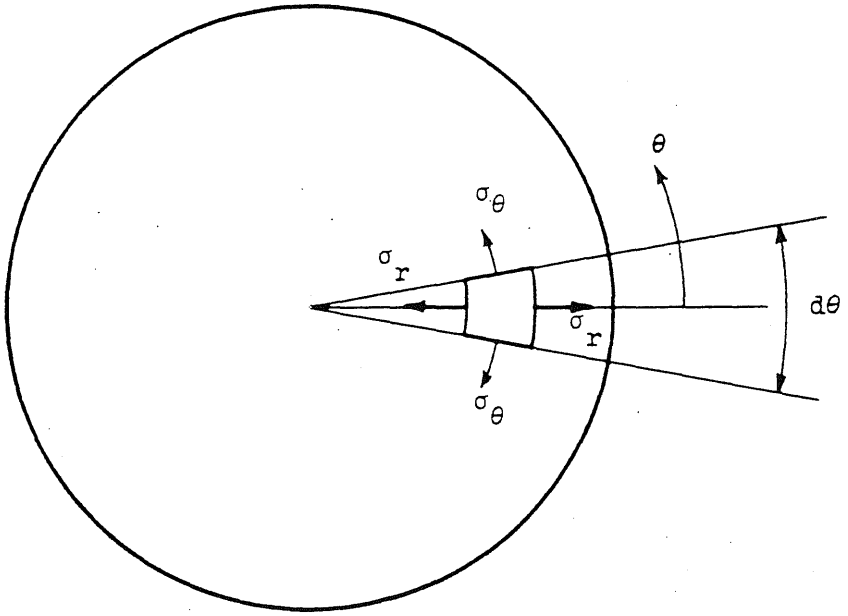

b. Horizontal Cross Section

FIG. 3. AXIALLY SYMMETRIC BODY

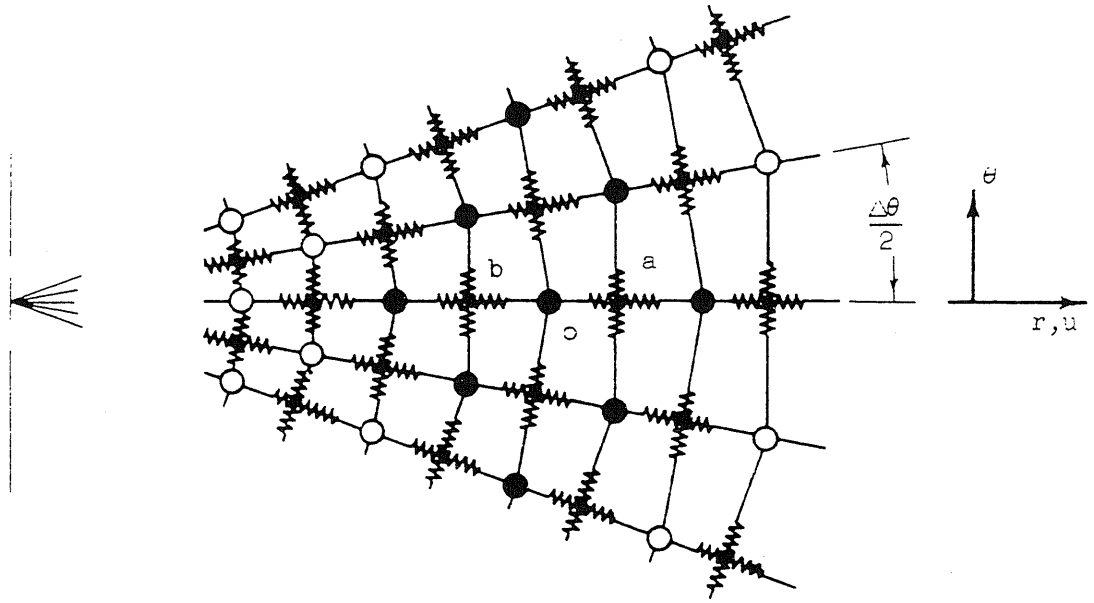

a. Plan View

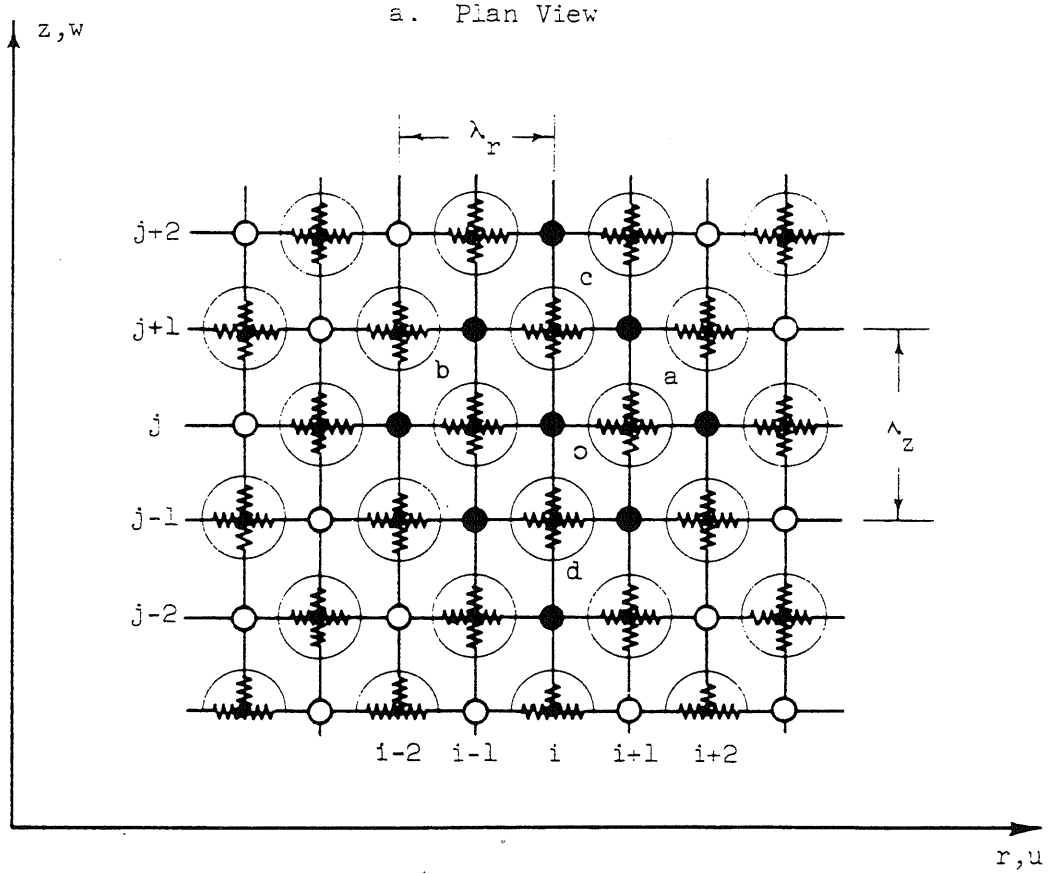

b. Radial Section ($\theta=0^{\circ}$)

FIG. 4. THE LUMPED PARAMETER MODEL

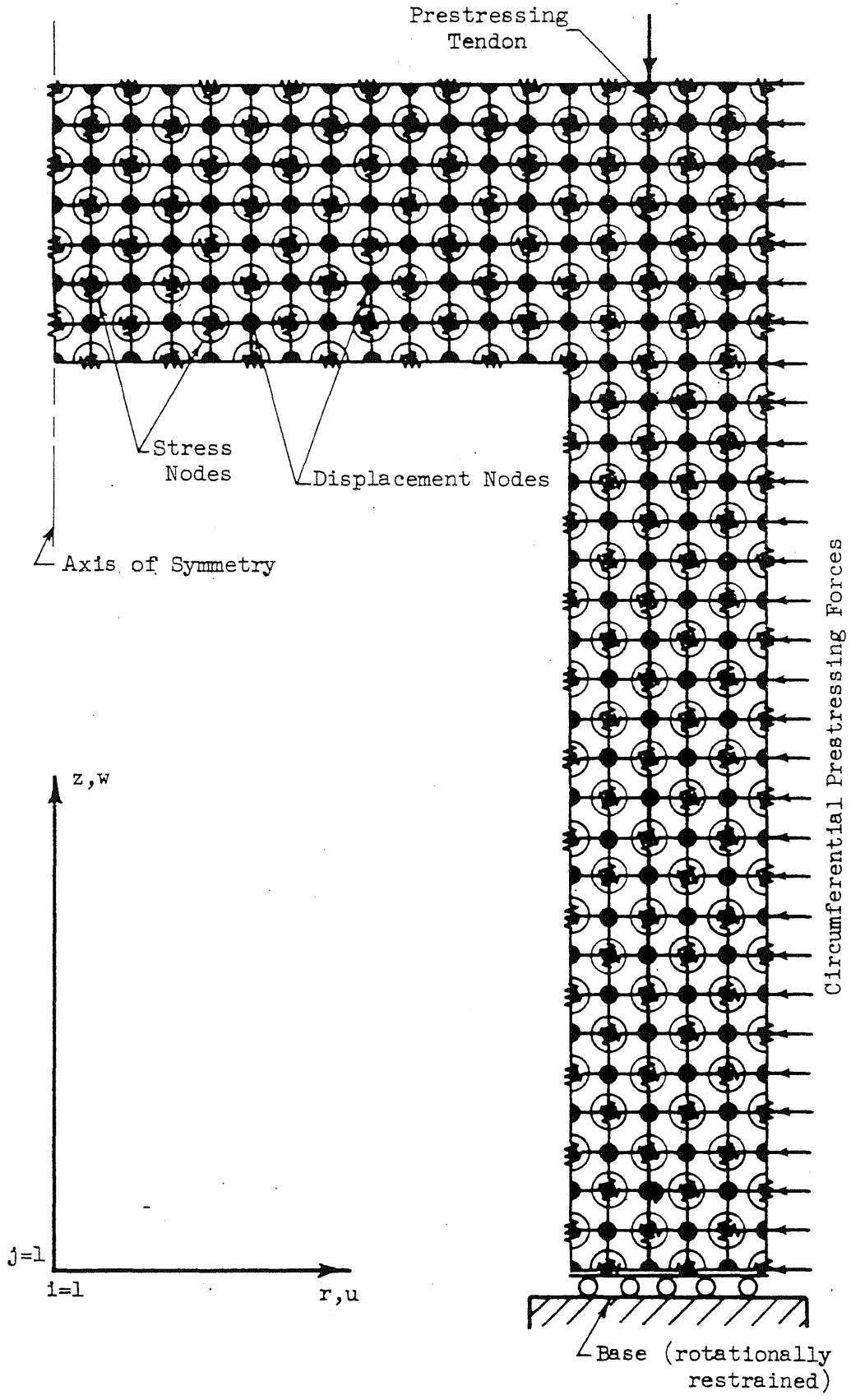

FIG. 5. LUMPED PARAMETER REPRESENTATION OF THE PRESSURE VESSEL

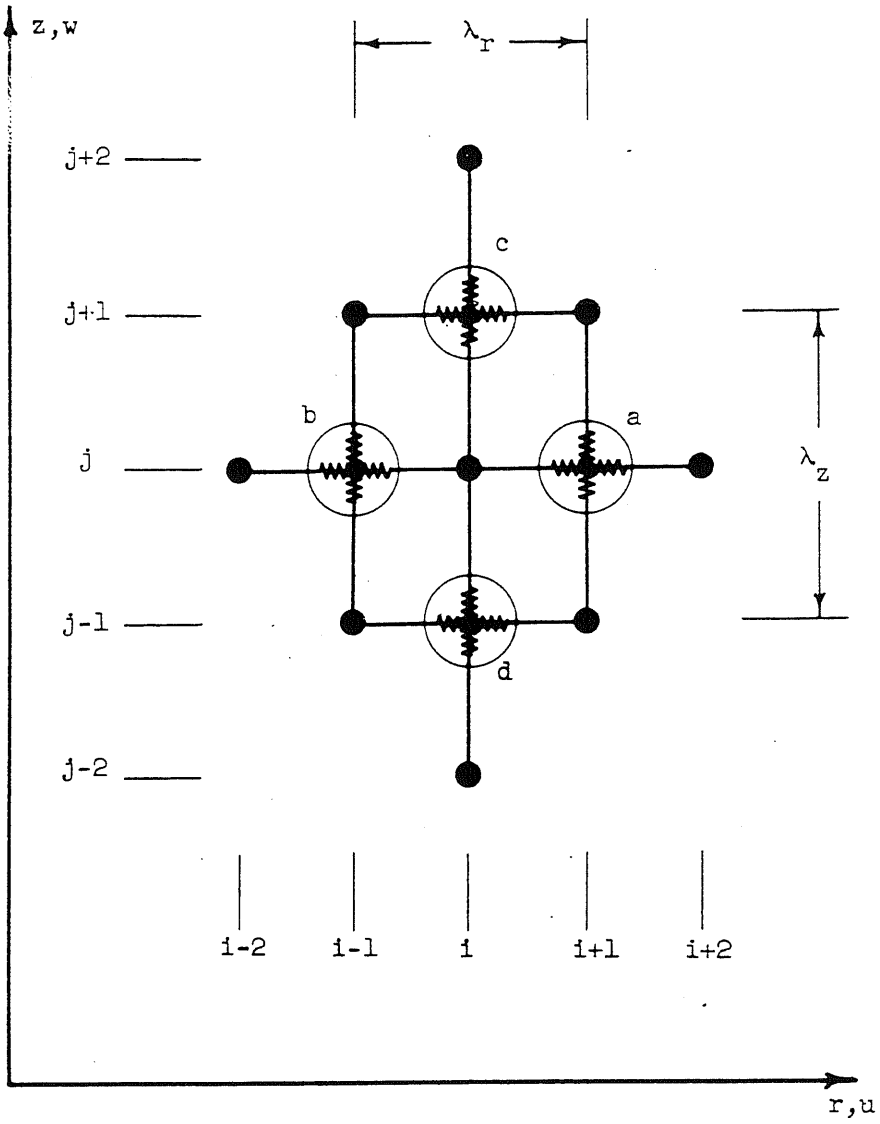

FIG. 6. MODEL ANALOGUE OF TYPICAL MASS ELEMENT

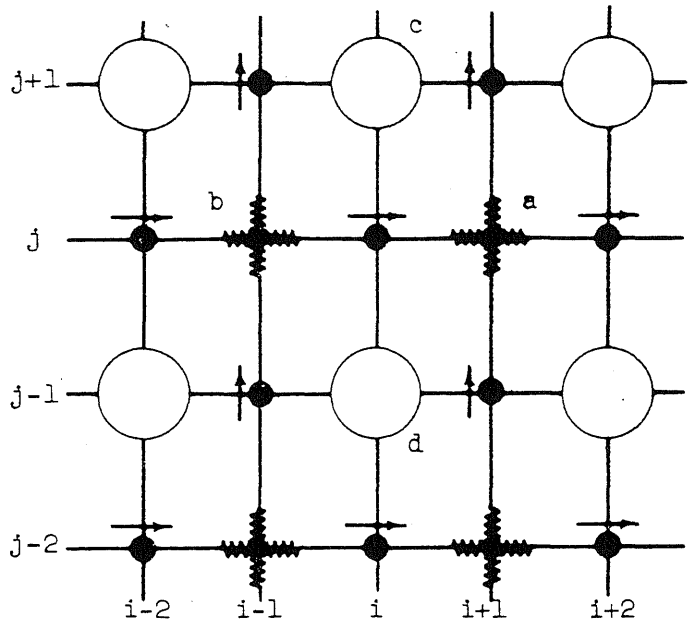

a. Grid 1

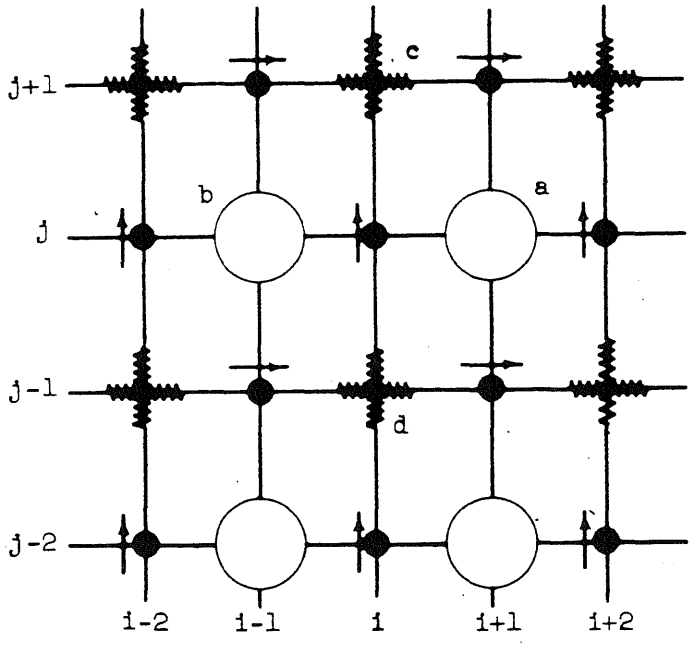

b. Grid 2

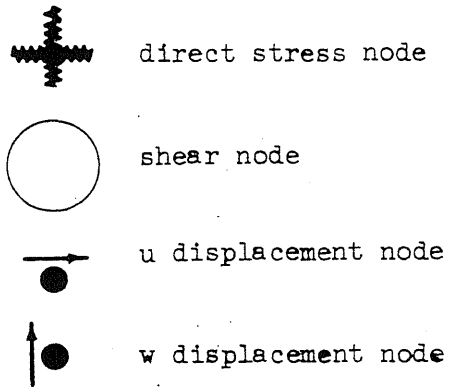

FIG. 7. COMPONENT GRIDS

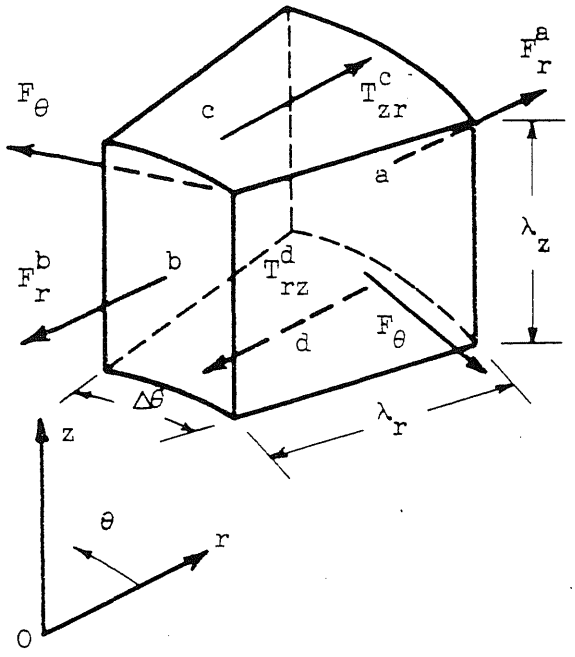

$$F_r^a = \sigma_r^a \, r_{i+1} \, \Delta\theta \, \lambda_z$$

$$F_r^b = \sigma_r^b \, r_{i-1} \, \Delta\theta \, \lambda_z$$

$$T_{rz}^c = \tau_{rz}^c \, r_i \, \Delta\theta \, \lambda_r$$

$$T_{rz}^d = \tau_{rz}^d \, r_i \, \Delta\theta \, \lambda_r$$

$$F_\theta = \sigma_\theta \, \lambda_r \lambda_z$$

FIG. 8. R EQUATION FORCES ACTING ON TYPICAL MASS ELEMENT

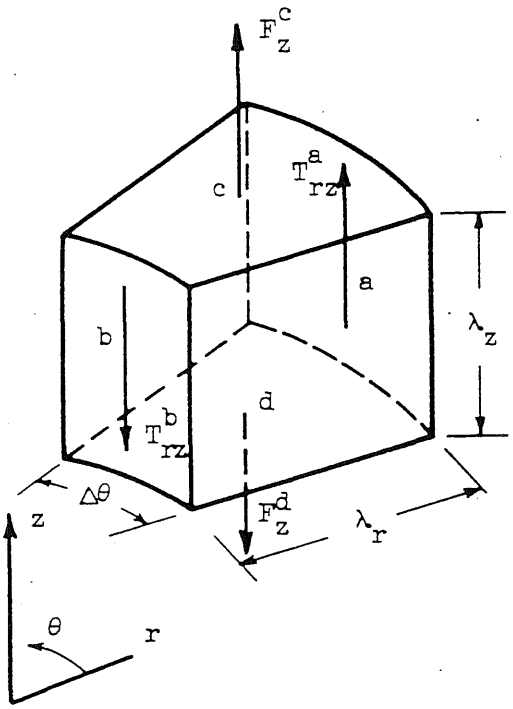

$$F_z^c = \sigma_z^c \, r_i \, \Delta\theta \, \lambda_r$$

$$F_z^d = \sigma_z^d \, r_i \, \Delta\theta \, \lambda_r$$

$$T_{rz}^a = \tau_{rz}^a \, r_{i+1} \, \Delta\theta \, \lambda_z$$

$$T_{rz}^b = \tau_{rz}^b \, r_{i-1} \, \Delta\theta \, \lambda_z$$

FIG. 9. Z EQUATION FORCES ACTING ON TYPICAL MASS ELEMENT

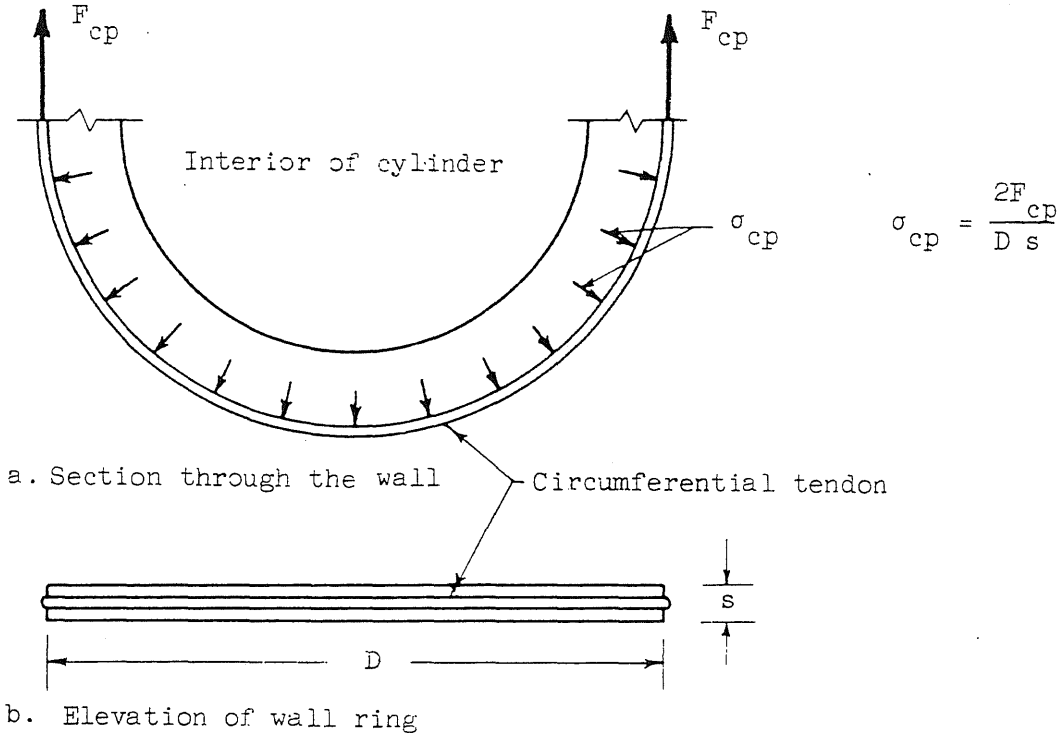

FIG. 10. NORMAL PRESSURE EQUIVALENT OF CIRCUMFERENTIAL PRESTRESSING

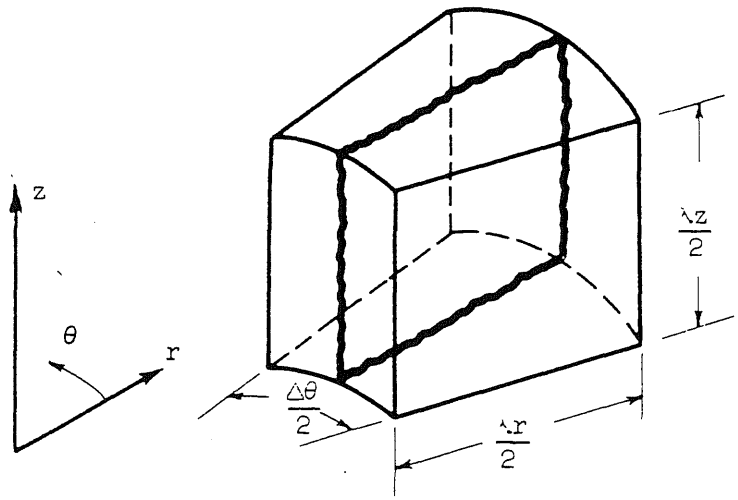

FIG. 11. RADIAL CRACK PLANE

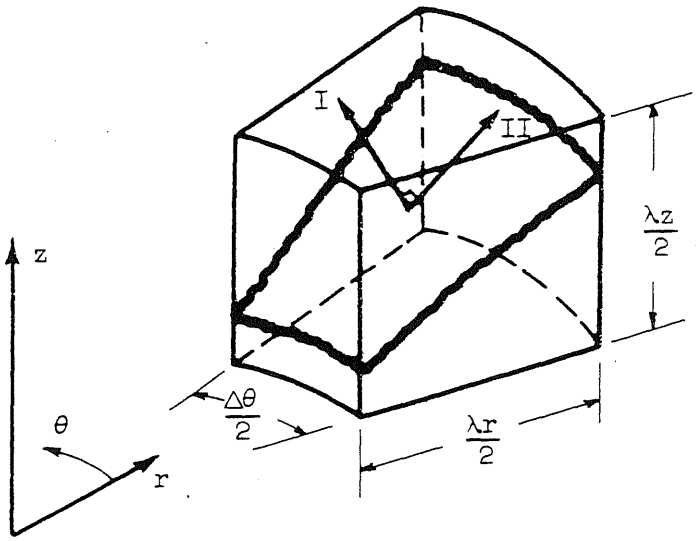

FIG. 12. CONICAL CRACK SURFACE

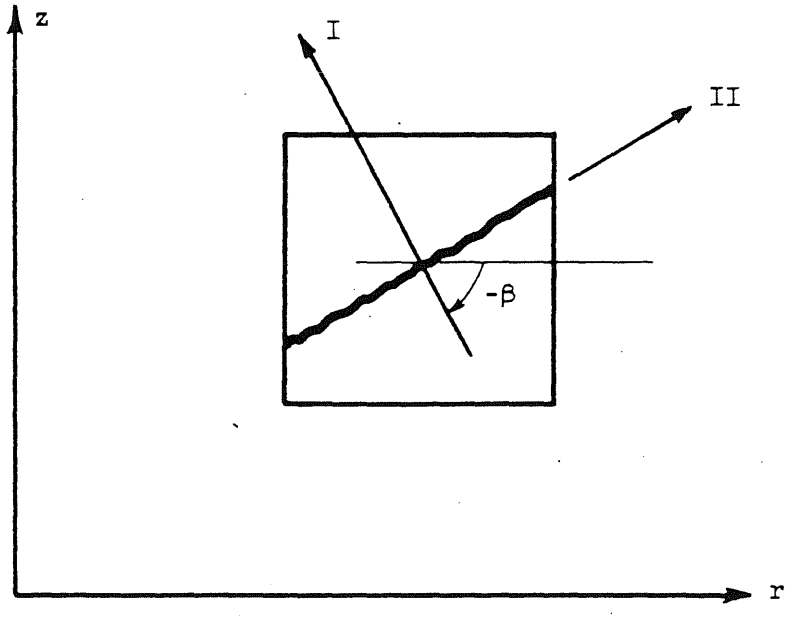

FIG. 13. CONICAL CRACK TRACE ON A RADIAL PLANE

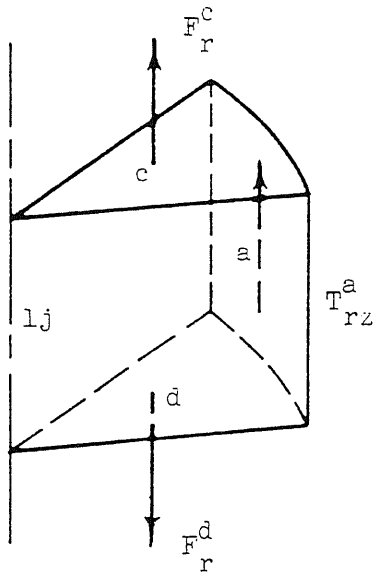

a. Mass Element

Equilibrium Equations:

r direction:

$$u_{lj} = 0$$

z direction:

$$\frac{\sigma_z^c - \sigma_z^d}{\Delta z} + 4 \frac{\tau_{rz}^a}{\Delta r} = 0$$

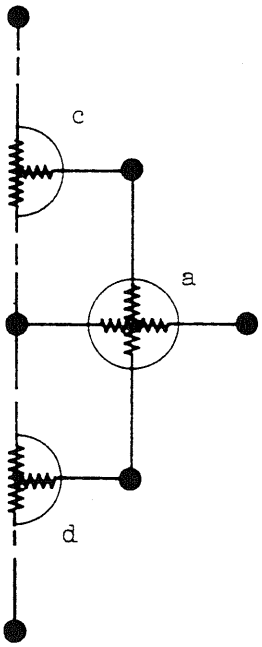

b. Grid Representation

Strain-displacement relations:

$$\epsilon_r^c = 2 \frac{u_{2j+1}}{\Delta r}$$

$$\epsilon_\theta^c = \epsilon_r^c$$

$$\gamma_{rz}^c = 0$$

FIG. 14. BOUNDARY CONDITIONS AT THE AXIS OF SYMMETRY

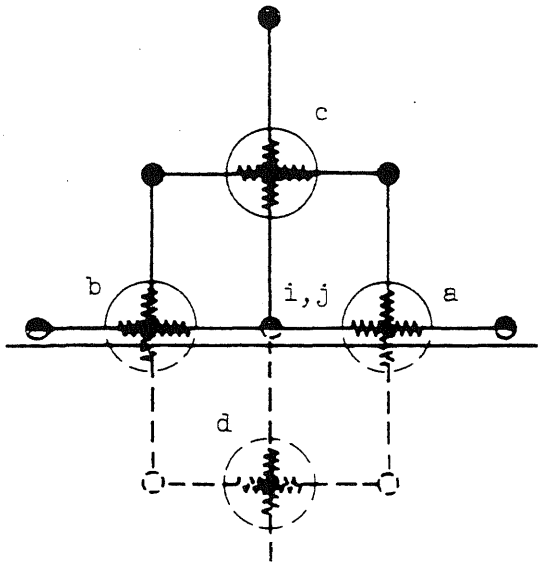

Equilibrium Equations:

r direction:

$$\frac{\sigma_r^a - \sigma_r^b}{\lambda_r} + 2\frac{\tau_{rz}^b}{\lambda_z} + \frac{\frac{1}{2}(\sigma_r^a + \sigma_r^b) - \sigma_\theta}{r_i} = 0$$

z direction:

$$w_{i1} = 0$$

$$\epsilon_z^a = 2\frac{w_{i+1,1}}{\lambda_z}$$

FIG. 15. BOUNDARY CONDITIONS AT MID-HEIGHT

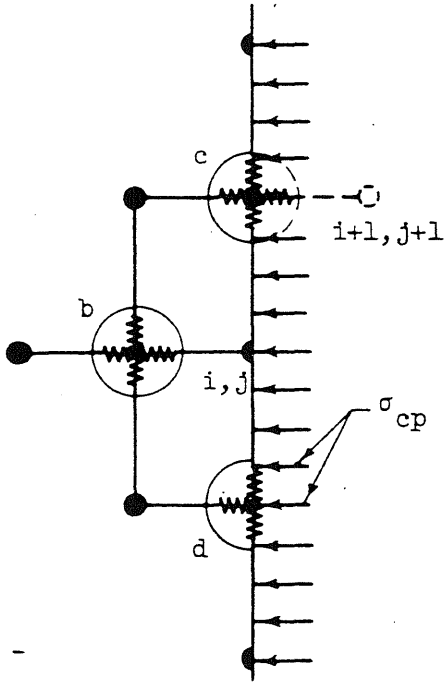

Equilibrium Equations:

r direction:

$$-2\frac{\sigma_{cp} + \sigma_r^b}{\lambda_r} + \frac{\sigma_r^b - \sigma_\theta}{r_i} = 0$$

z equation:

$$\frac{\sigma_z^c - \sigma_z^d}{\lambda_z}\left(1 - \frac{\lambda_r}{4r_i}\right) - 2\frac{\tau_{rz}^b}{\lambda_r} + \frac{\tau_{rz}^b}{r_i} = 0$$

FIG. 16. BOUNDARY CONDITIONS AT EXTERIOR WALL SURFACE

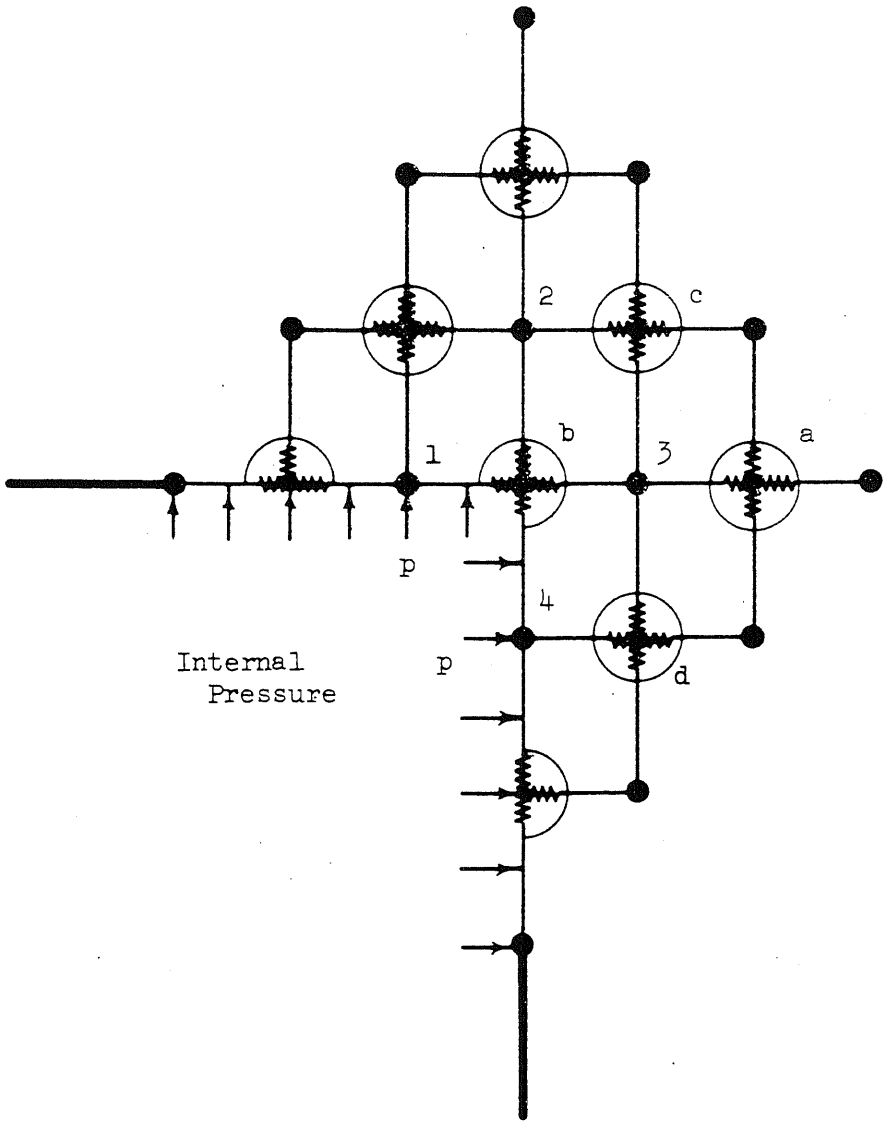

FIG. 17. GRID REPRESENTATION OF RE-ENTRANT CORNER

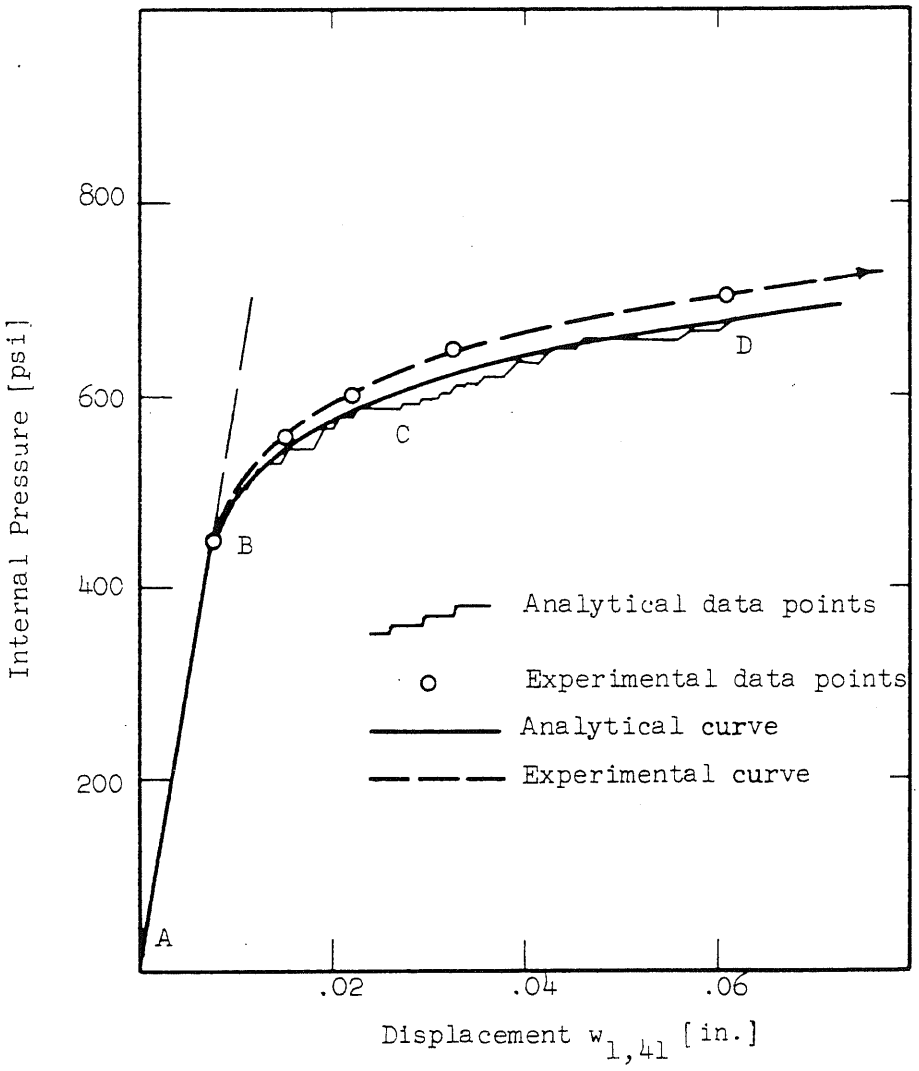

FIG. 18. LOAD-DEFORMATION DIAGRAM FOR THE SAMPLE VESSEL

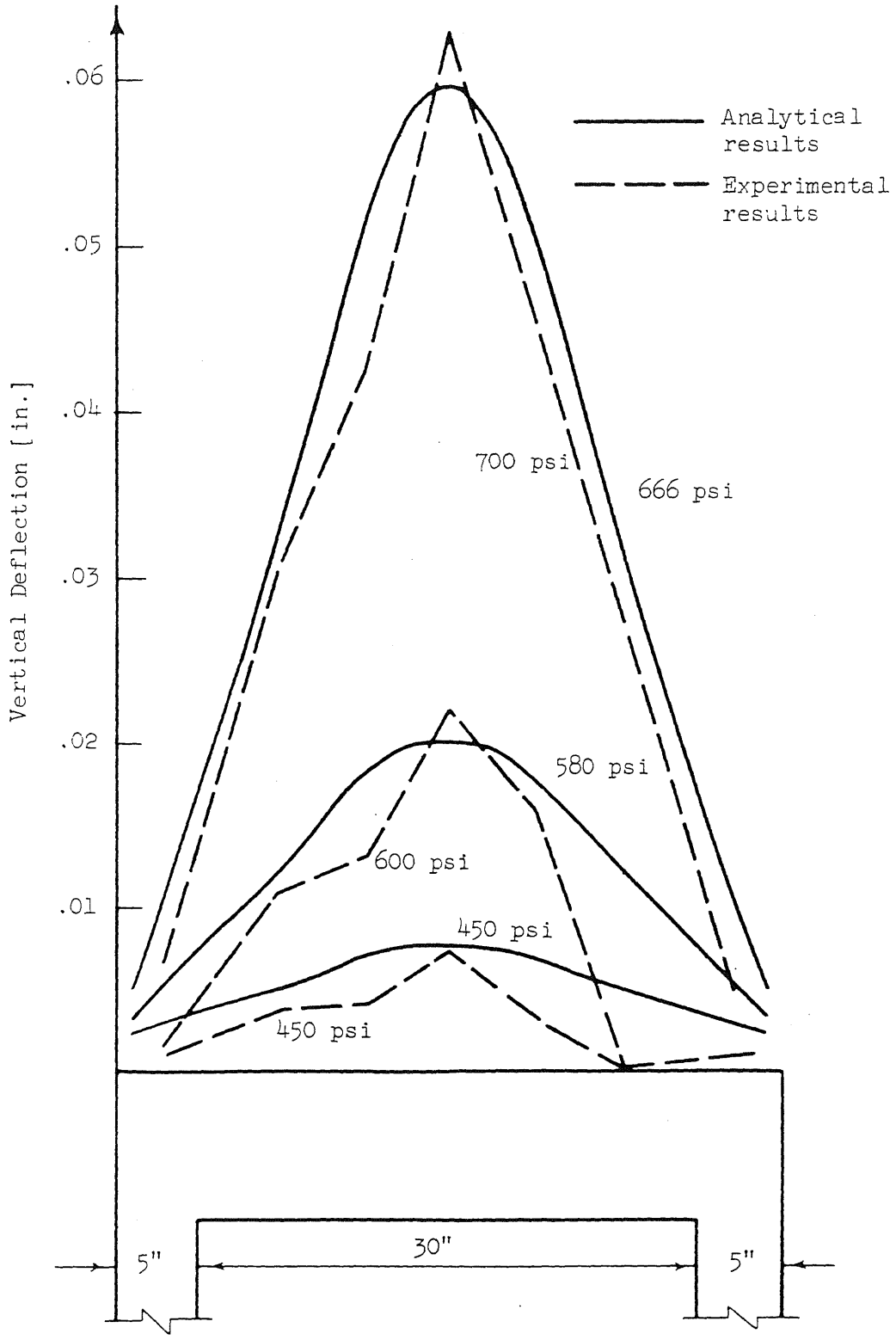

FIG. 19. DEFLECTION PROFILES OF THE END SLAB

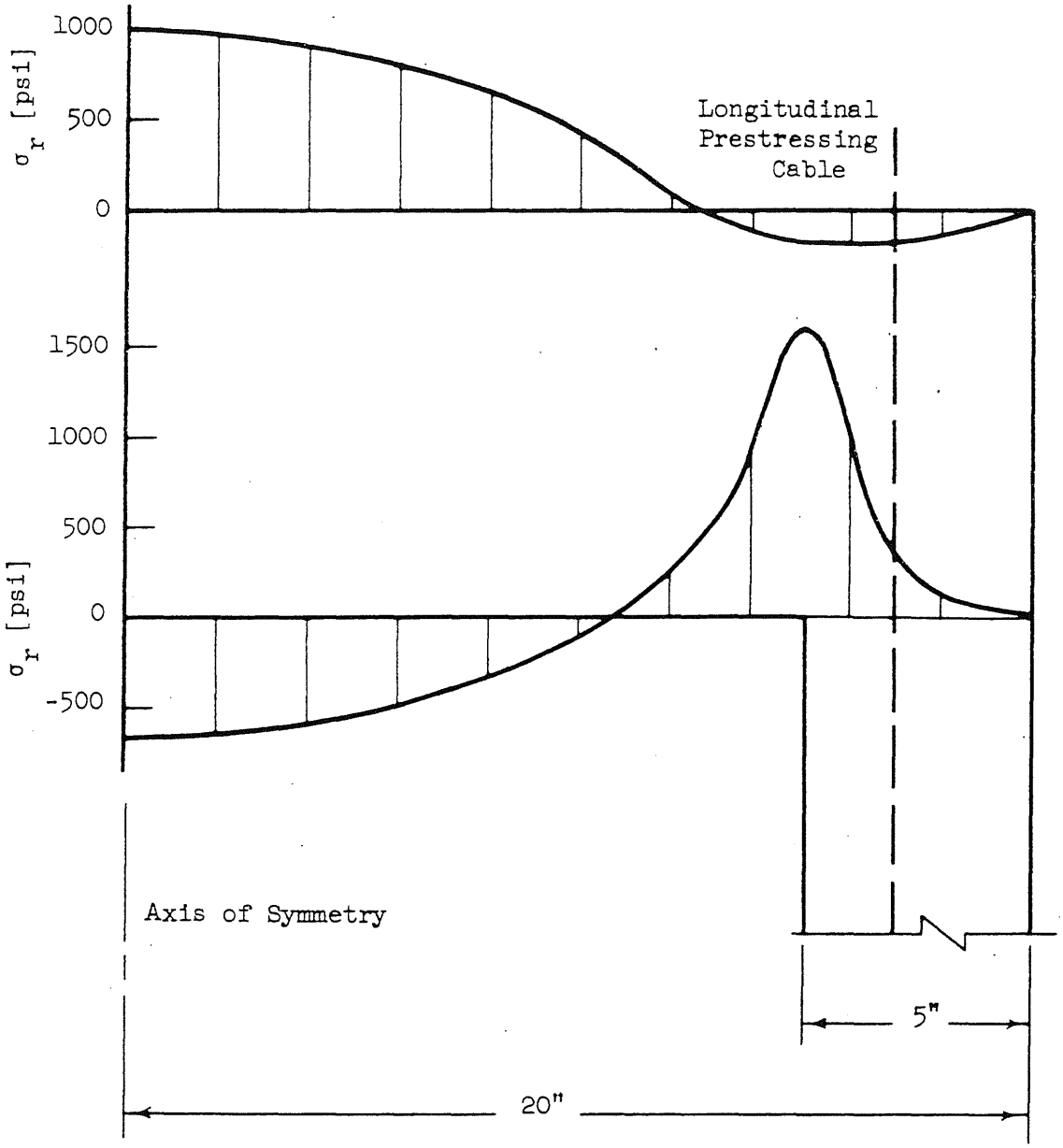

FIG. 20. RADIAL STRESSES IN THE SLAB UNDER INTERNAL PRESSURE OF 450 PSI AND ZERO PRESTRESS

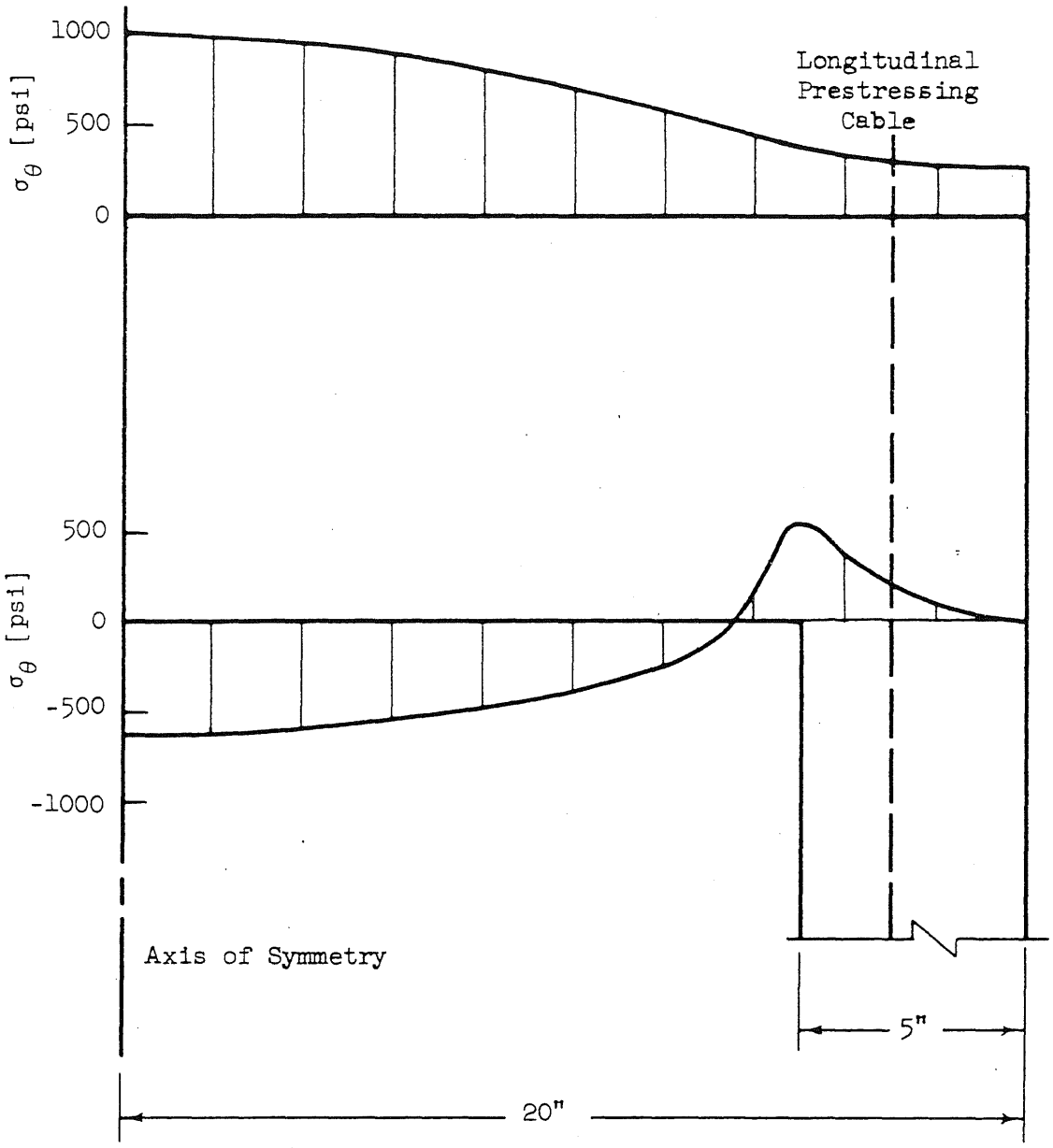

FIG. 21. CIRCUMFERENTIAL STRESSES IN THE SLAB UNDER INTERNAL PRESSURE OF 450 PSI AND ZERO PRESTRESS

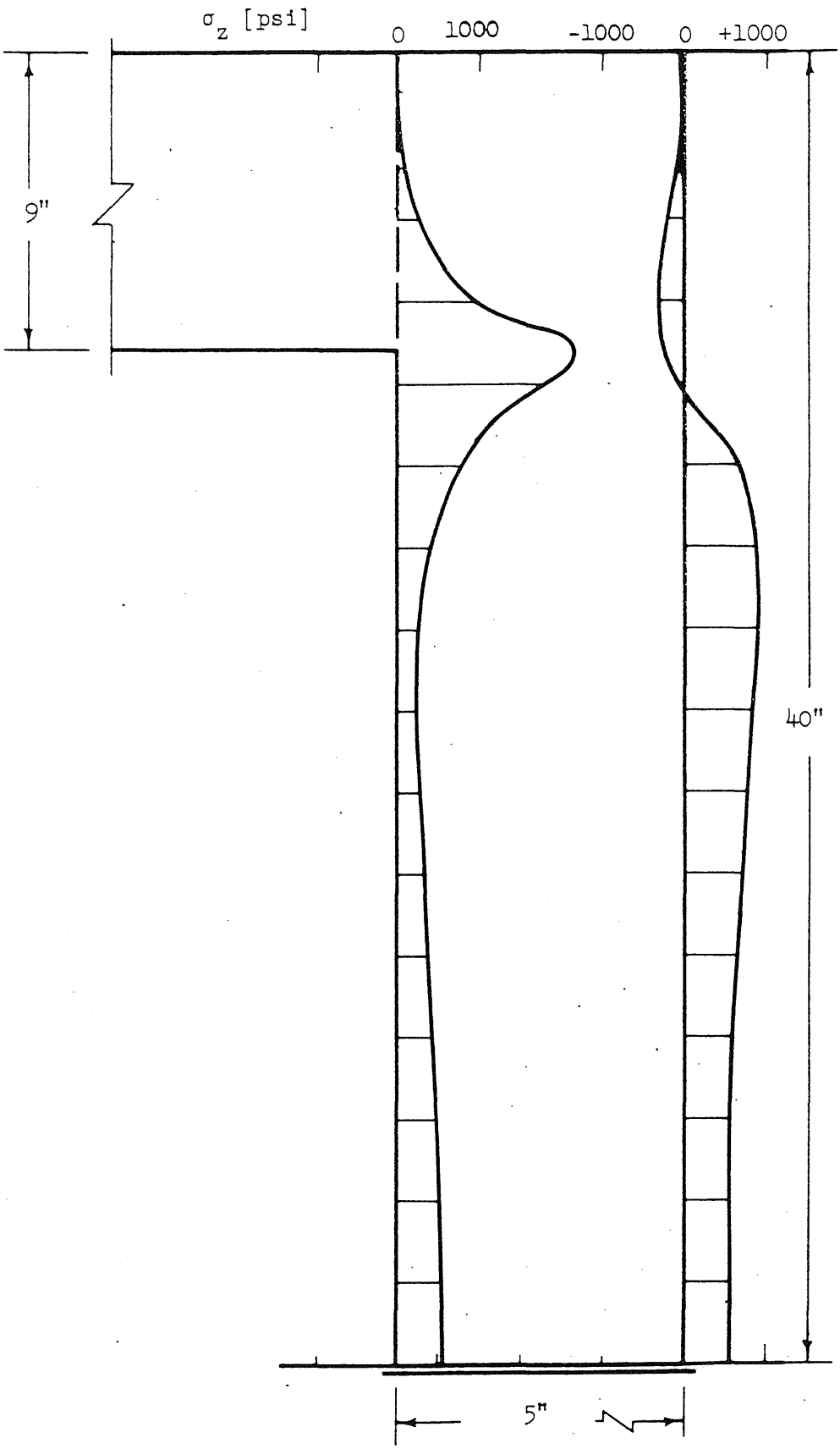

FIG. 22. LONGITUDINAL STRESSES IN THE CYLINDRICAL SIDE WALL UNDER INTERNAL PRESSURE OF 450 PSI AND ZERO PRESTRESS

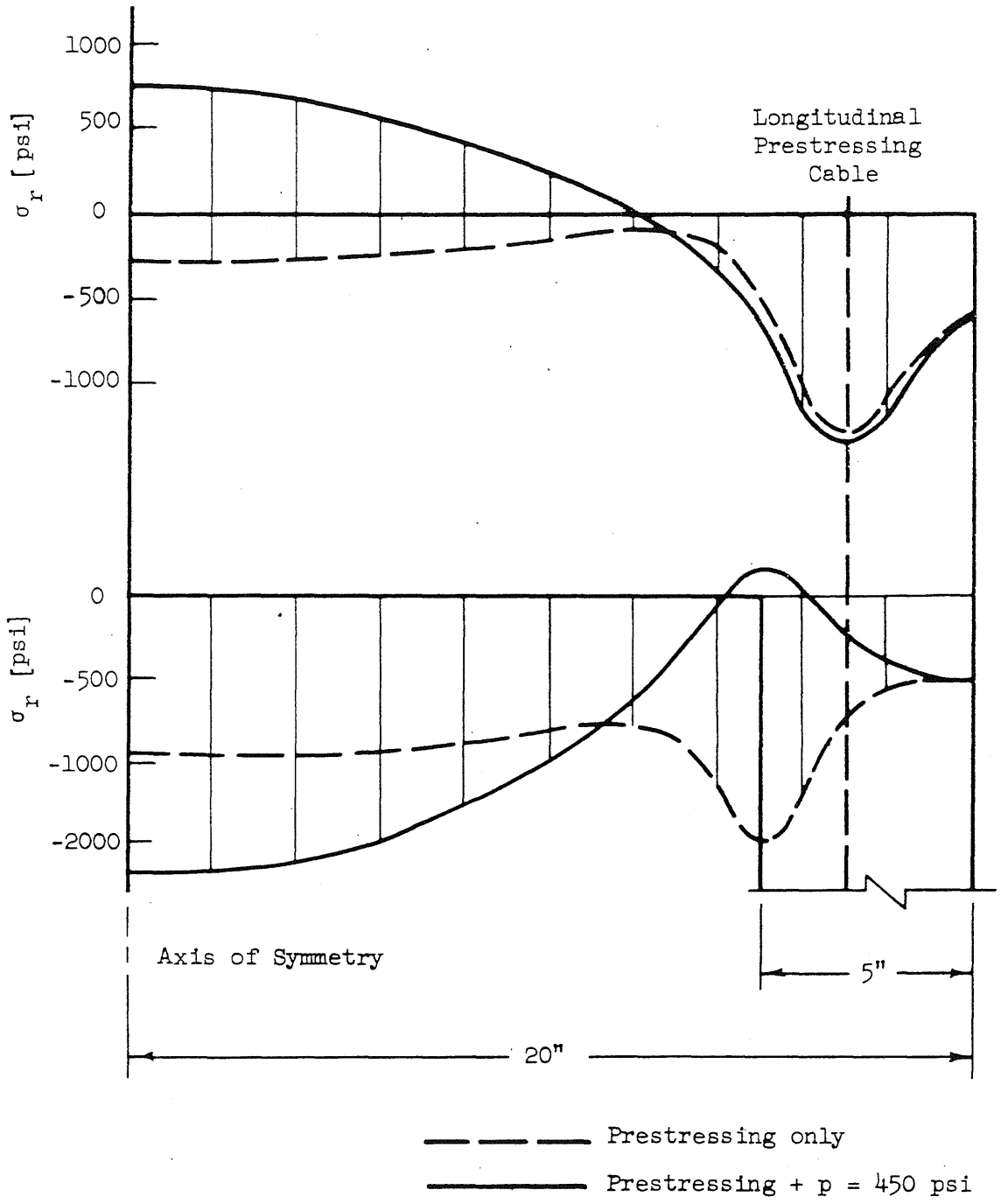

FIG. 23. RADIAL STRESSES IN THE SLAB FROM PRESTRESS AND PRESTRESS PLUS 450 PSI INTERNAL PRESSURE

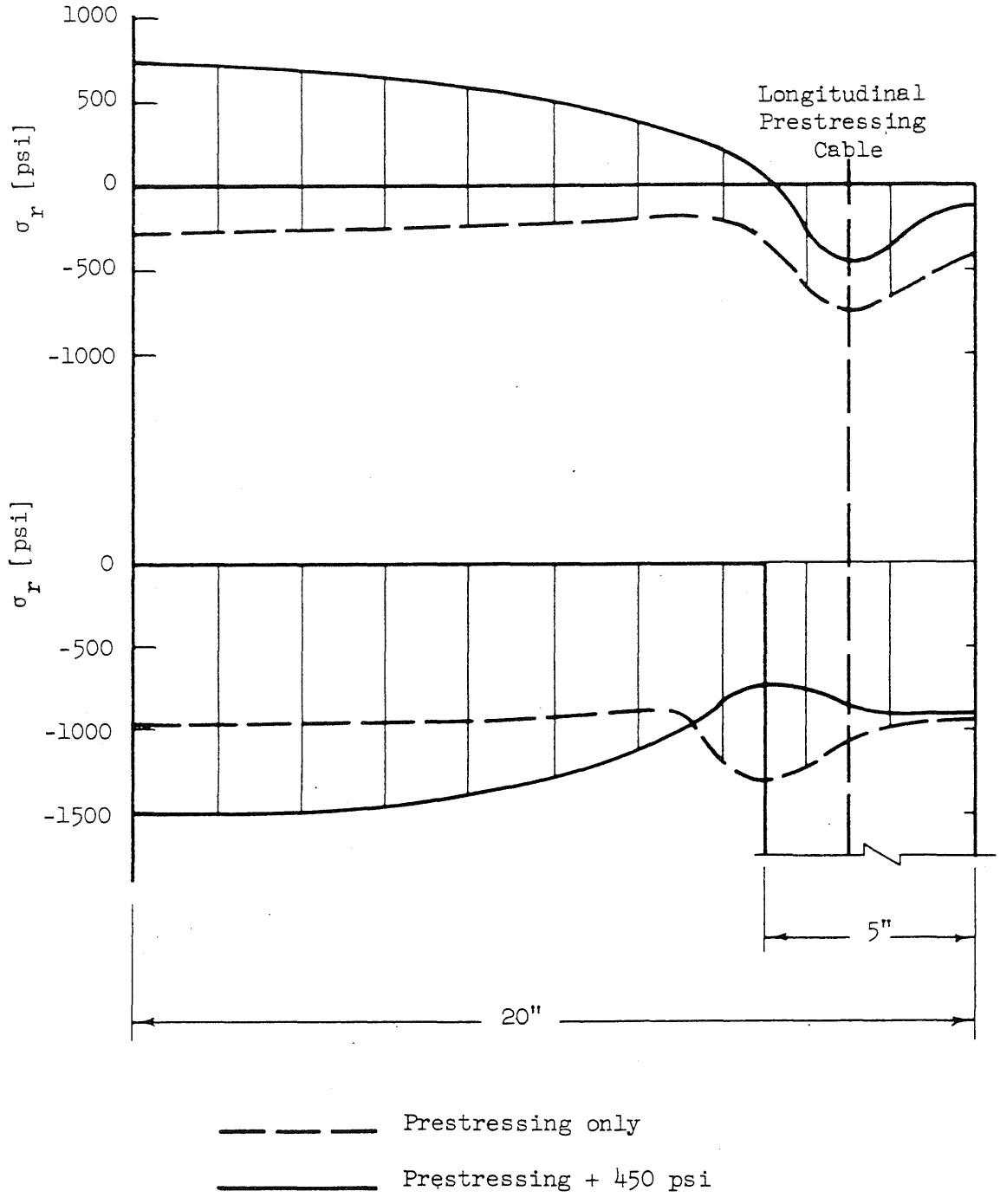

FIG. 24. CIRCUMFERENTIAL STRESSES IN THE SLAB FROM PRESTRESS AND PRESTRESS PLUS 450 PSI INTERNAL PRESSURE

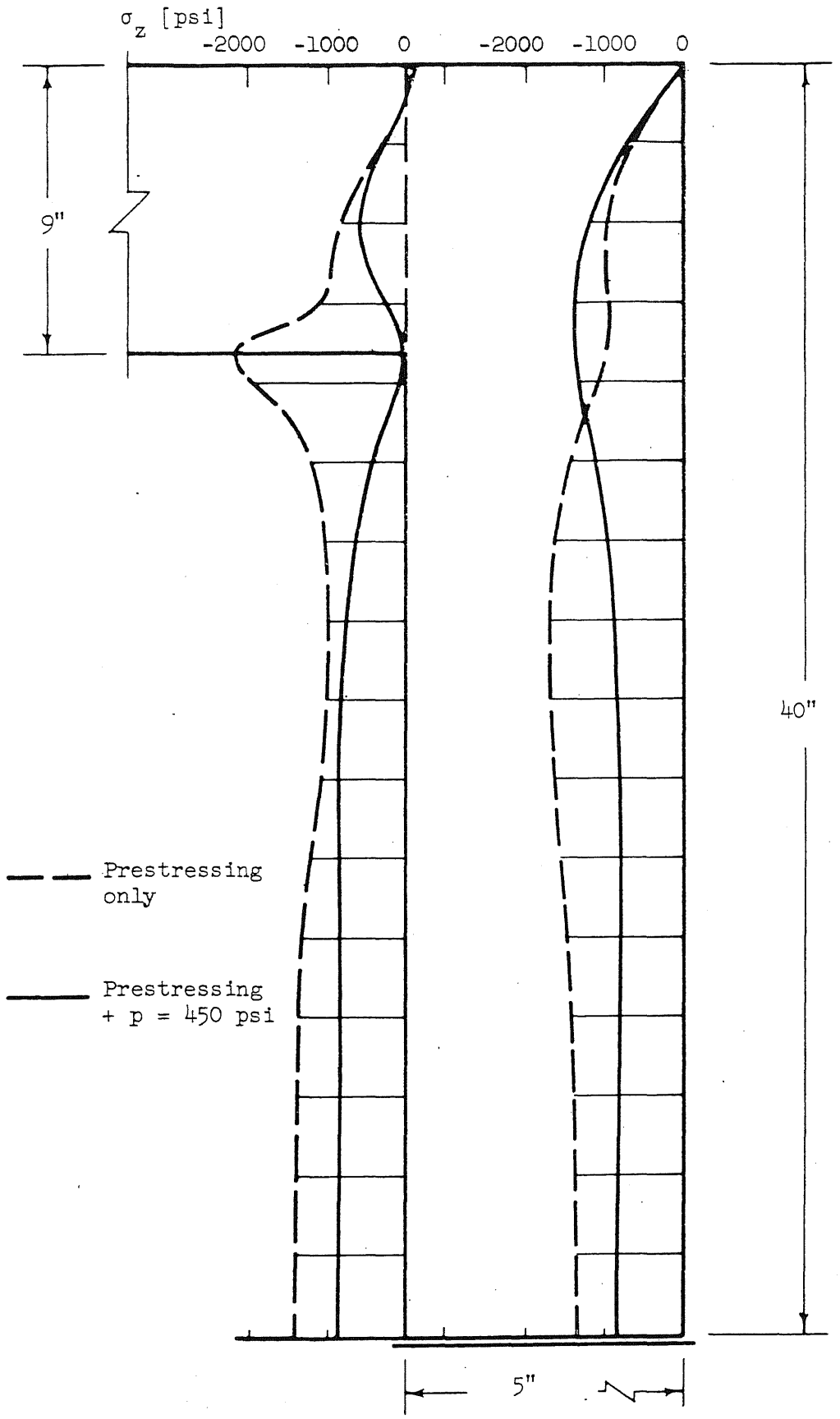

FIG. 25. LONGITUDINAL STRESSES IN THE CYLINDRICAL SIDE WALL FROM PRESTRESS AND PRESTRESS PLUS 450 PSI INTERNAL PRESSURE

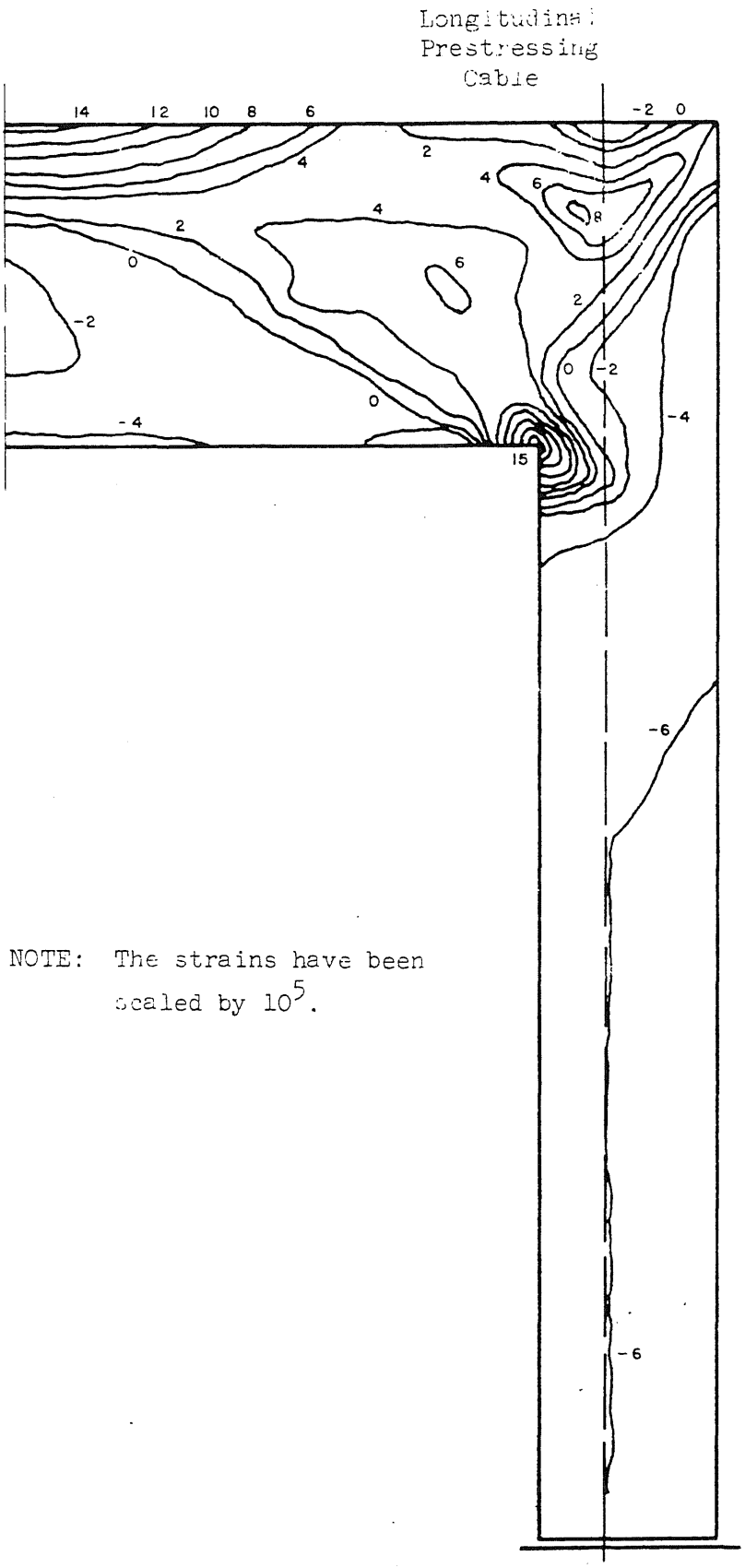

NOTE: The strains have been scaled by 10^5.

FIG. 26. MAXIMUM PRINCIPAL rz PLANE STRAIN TRAJECTORIES FOR PRESSURE OF 450 PSI

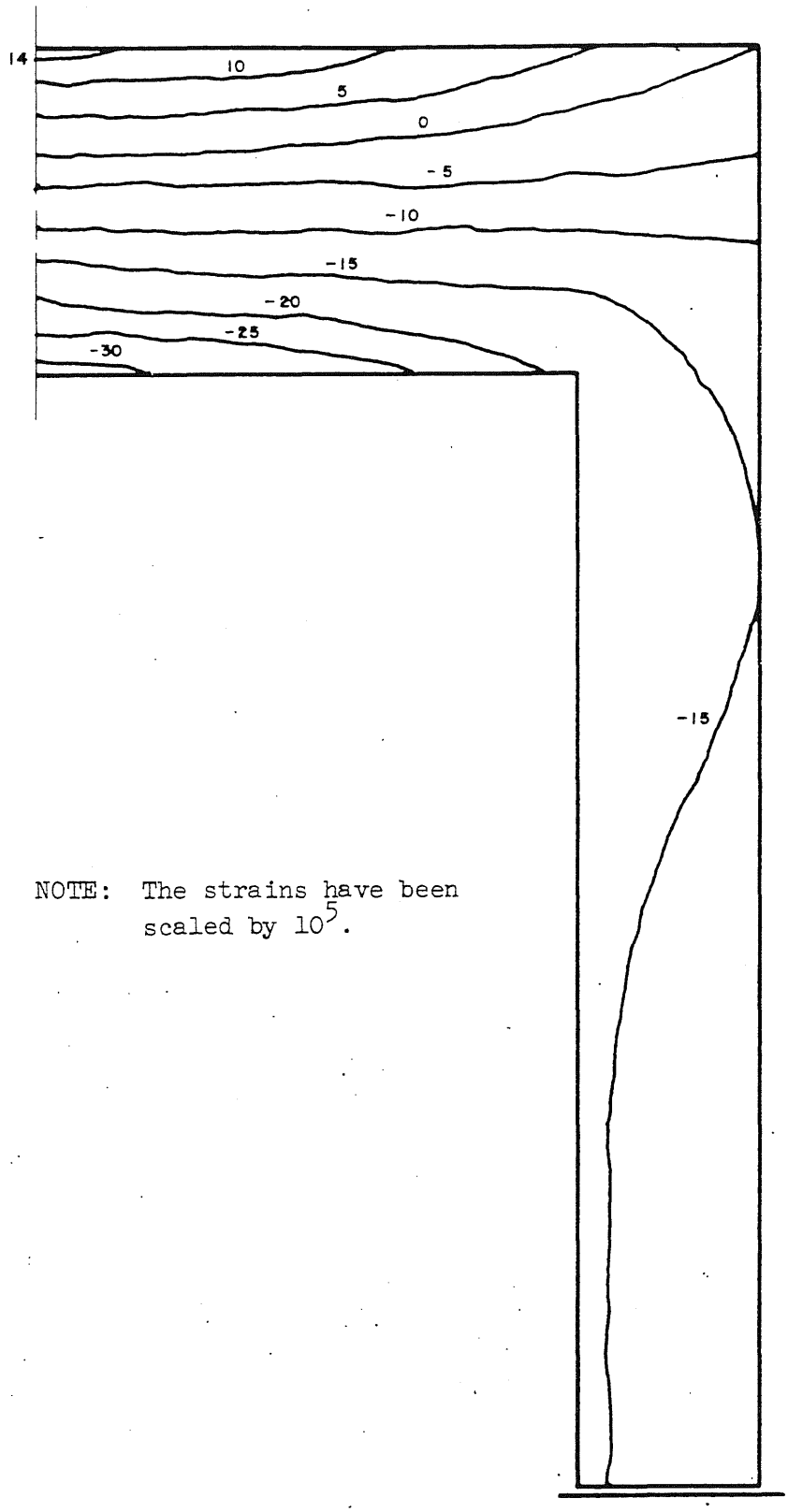

FIG. 27. CIRCUMFERENTIAL STRAIN TRAJECTORIES FOR PRESSURE OF 450 PSI

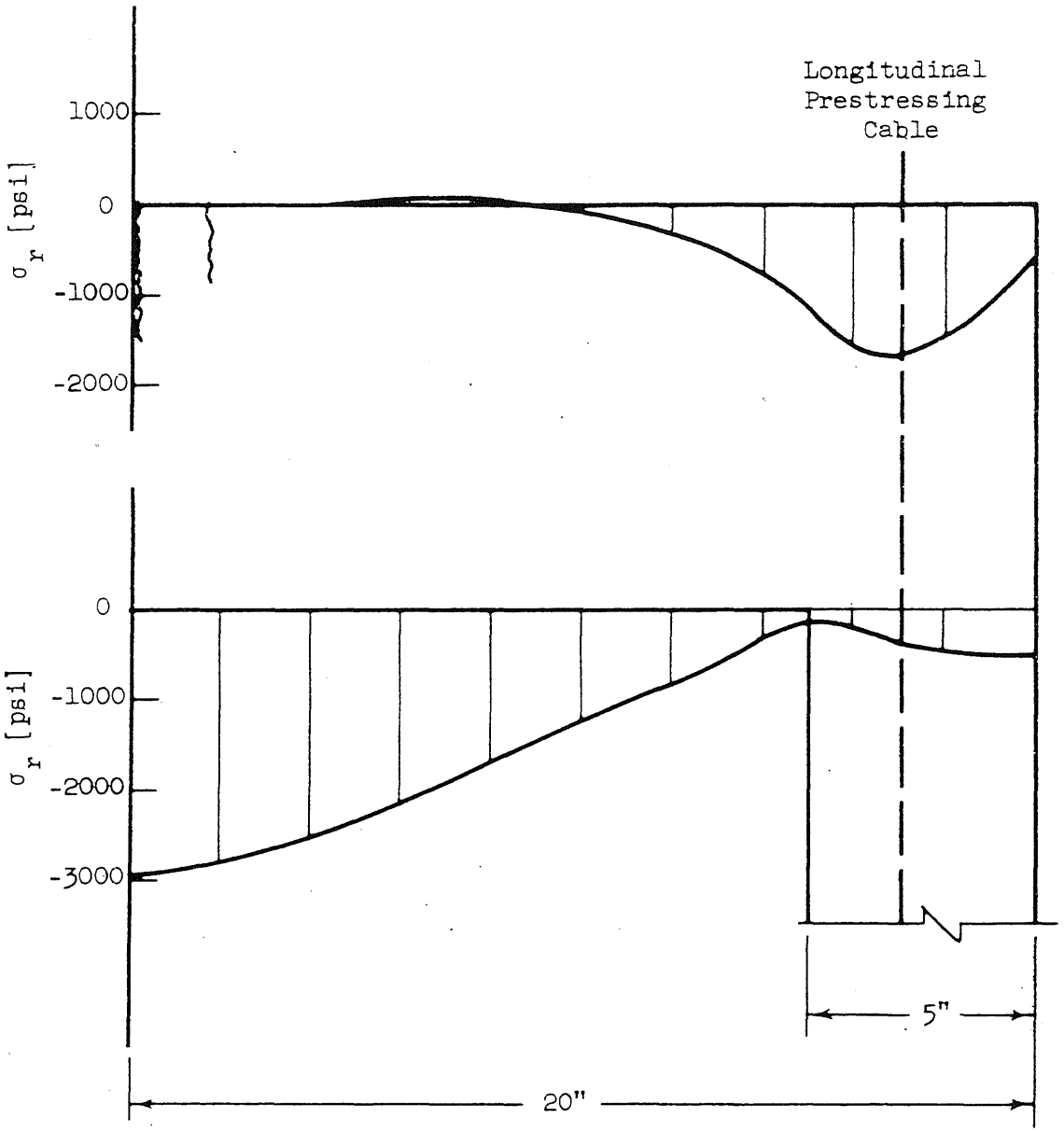

FIG. 28. RADIAL STRESSES IN THE SLAB FOR PRESSURE OF 580 PSI

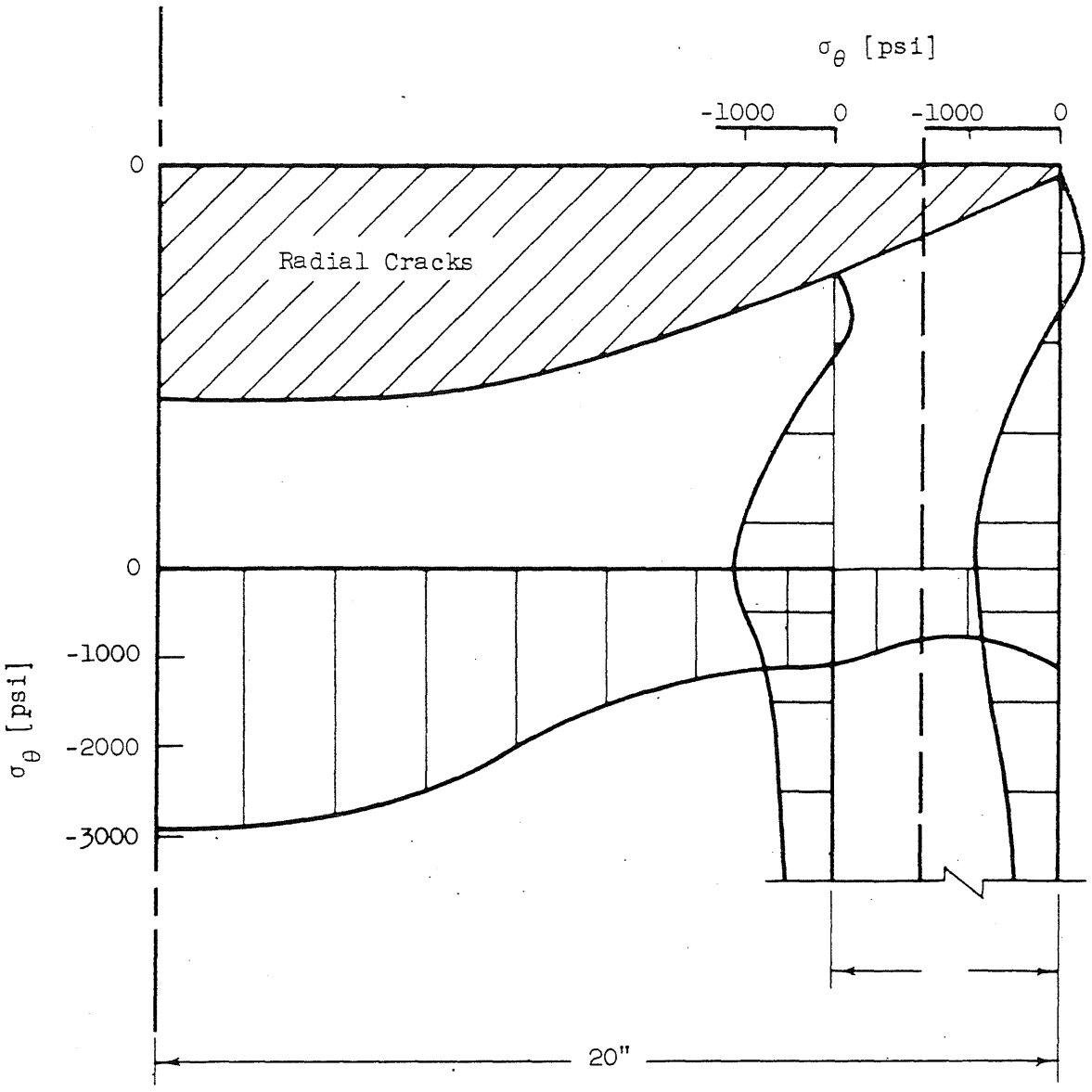

FIG. 29. CIRCUMFERENTIAL STRESSES IN THE SLAB AND CYLINDRICAL SIDE WALL FOR PRESSURE OF 580 PSI

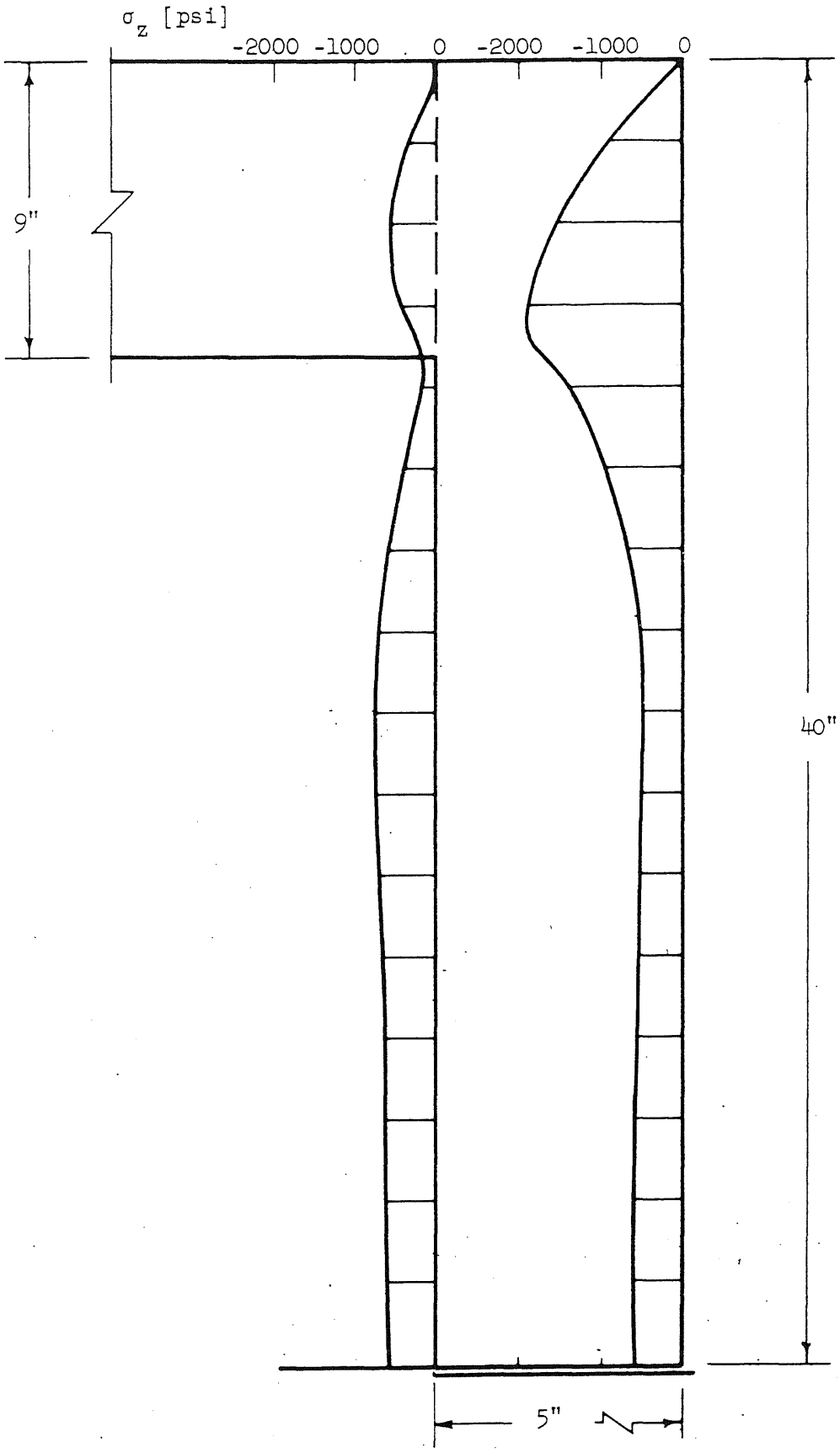

FIG. 30. LONGITUDINAL STRESSES IN THE CYLINDRICAL SIDE WALL FOR PRESSURE OF 580 PSI

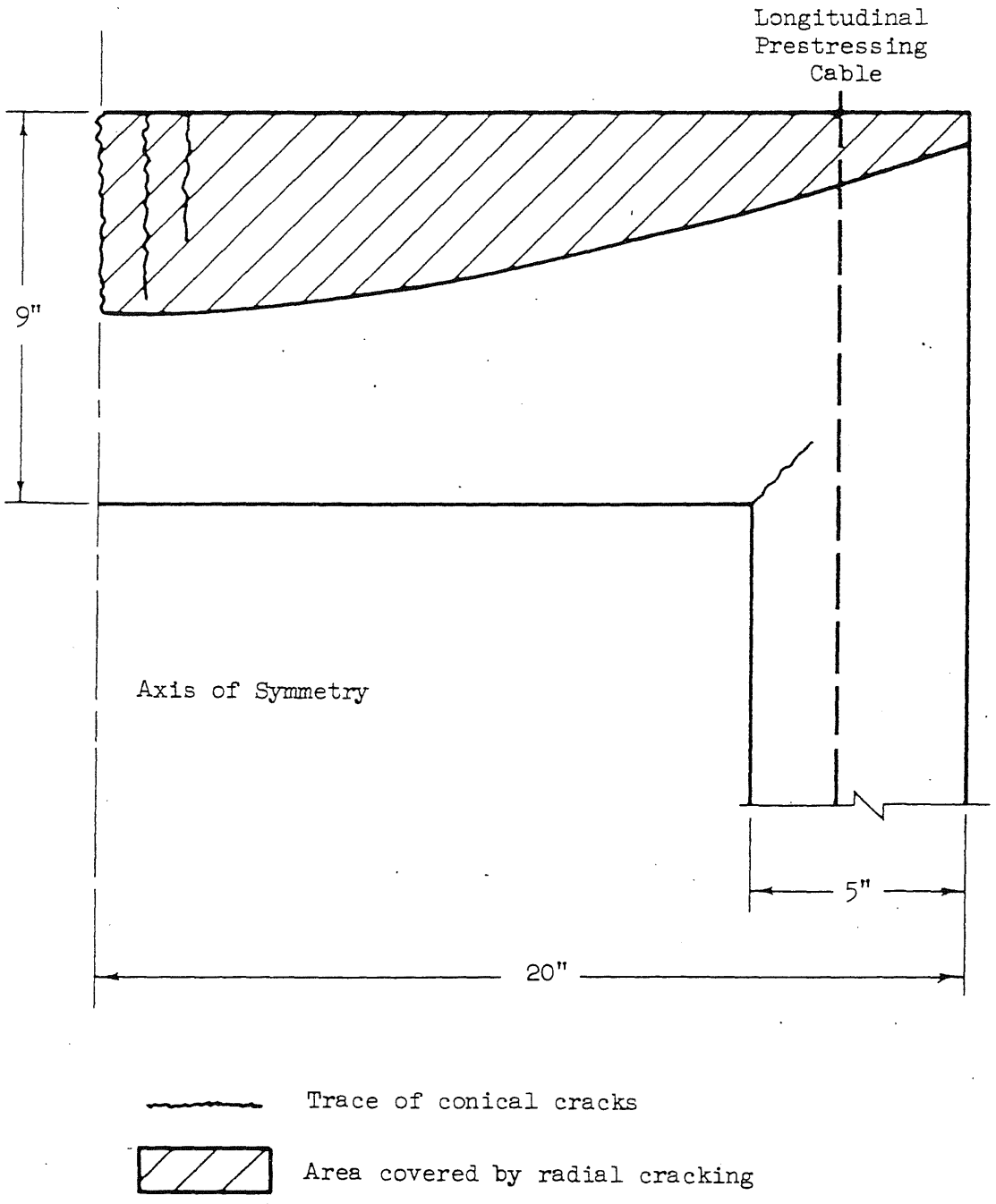

FIG. 31. EXTENT OF CRACKING FOR PRESSURE OF 580 PSI

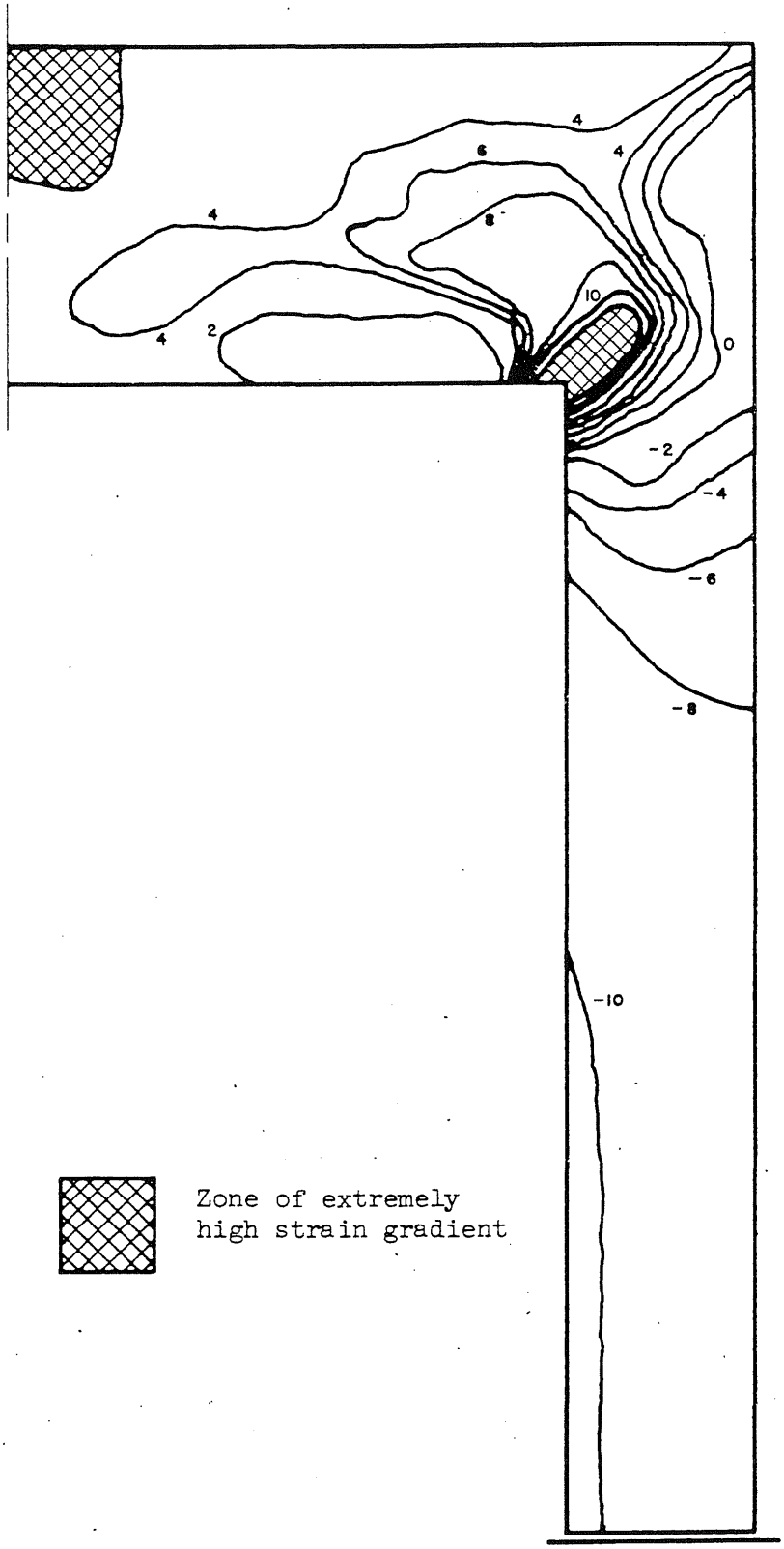

FIG. 32. MAXIMUM PRINCIPAL rz PLANE STRAIN TRAJECTORIES FOR PRESSURE OF 580 PSI

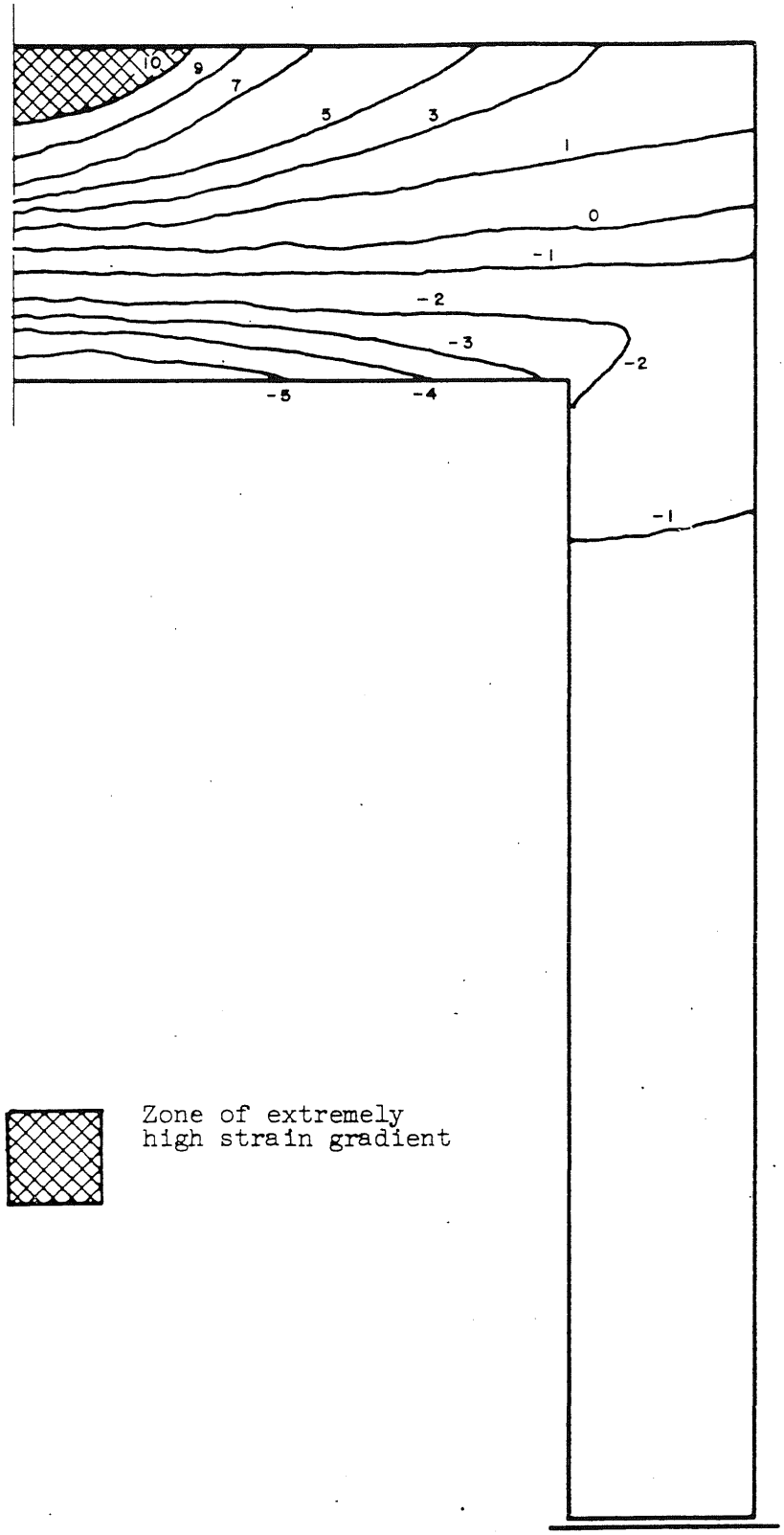

FIG. 33. CIRCUMFERENTIAL STRAIN TRAJECTORIES FOR PRESSURE OF 580 PSI

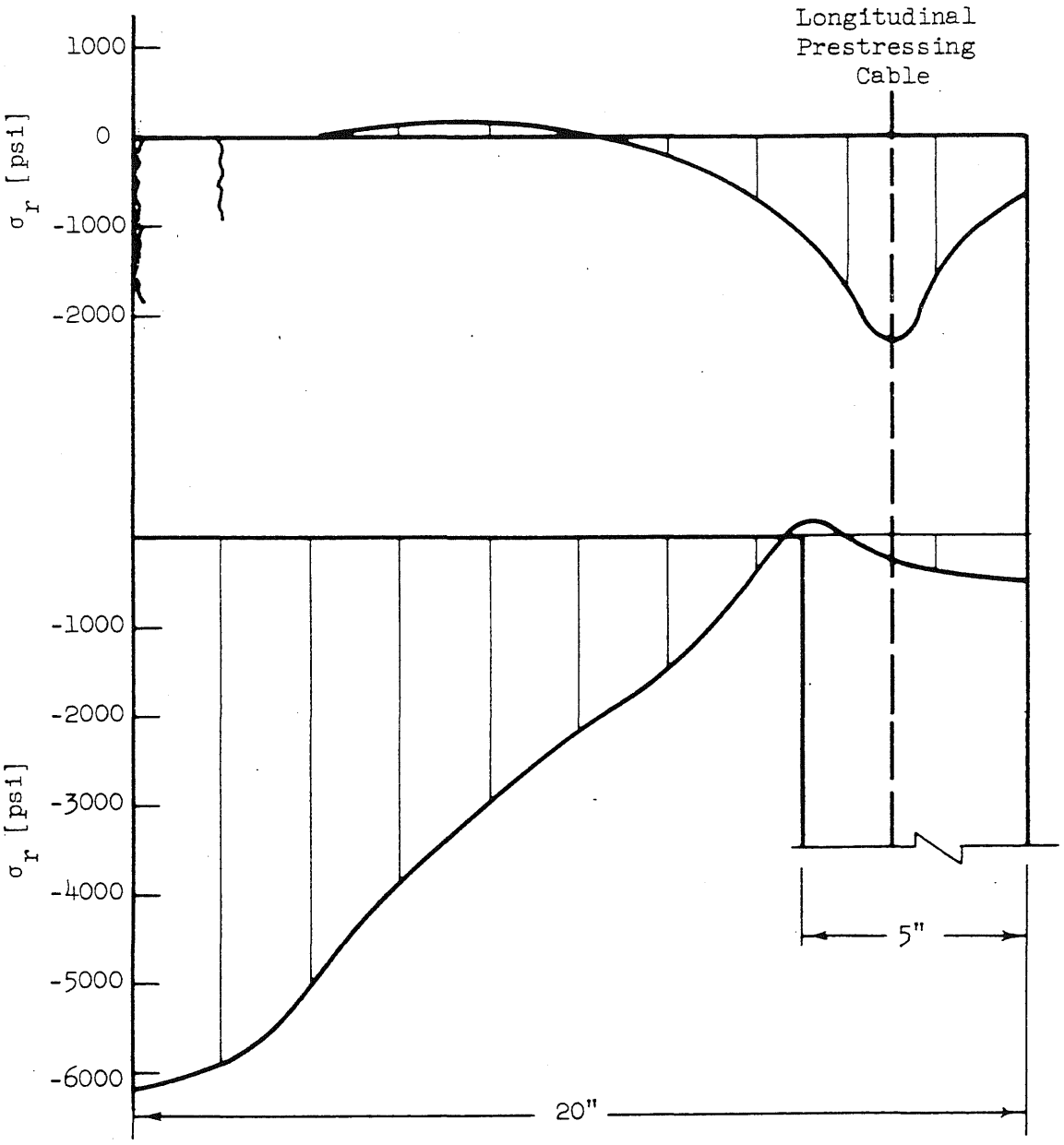

FIG. 34. RADIAL STRESSES IN THE SLAB FOR 666 PSI INTERNAL PRESSURE

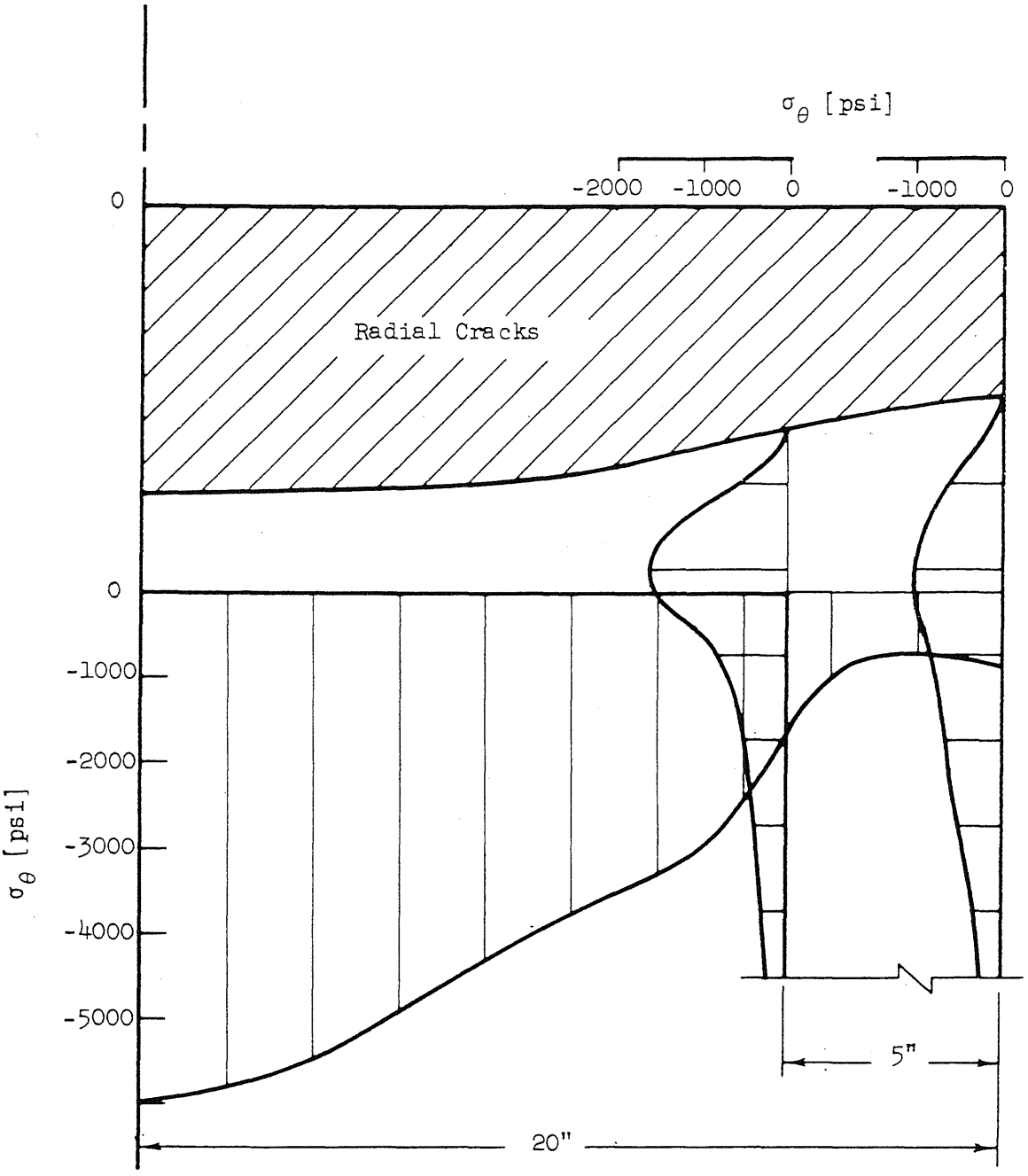

FIG. 35. CIRCUMFERENTIAL STRESSES IN THE SLAB AND CYLINDRICAL SIDE WALL FOR PRESSURE OF 666 PSI

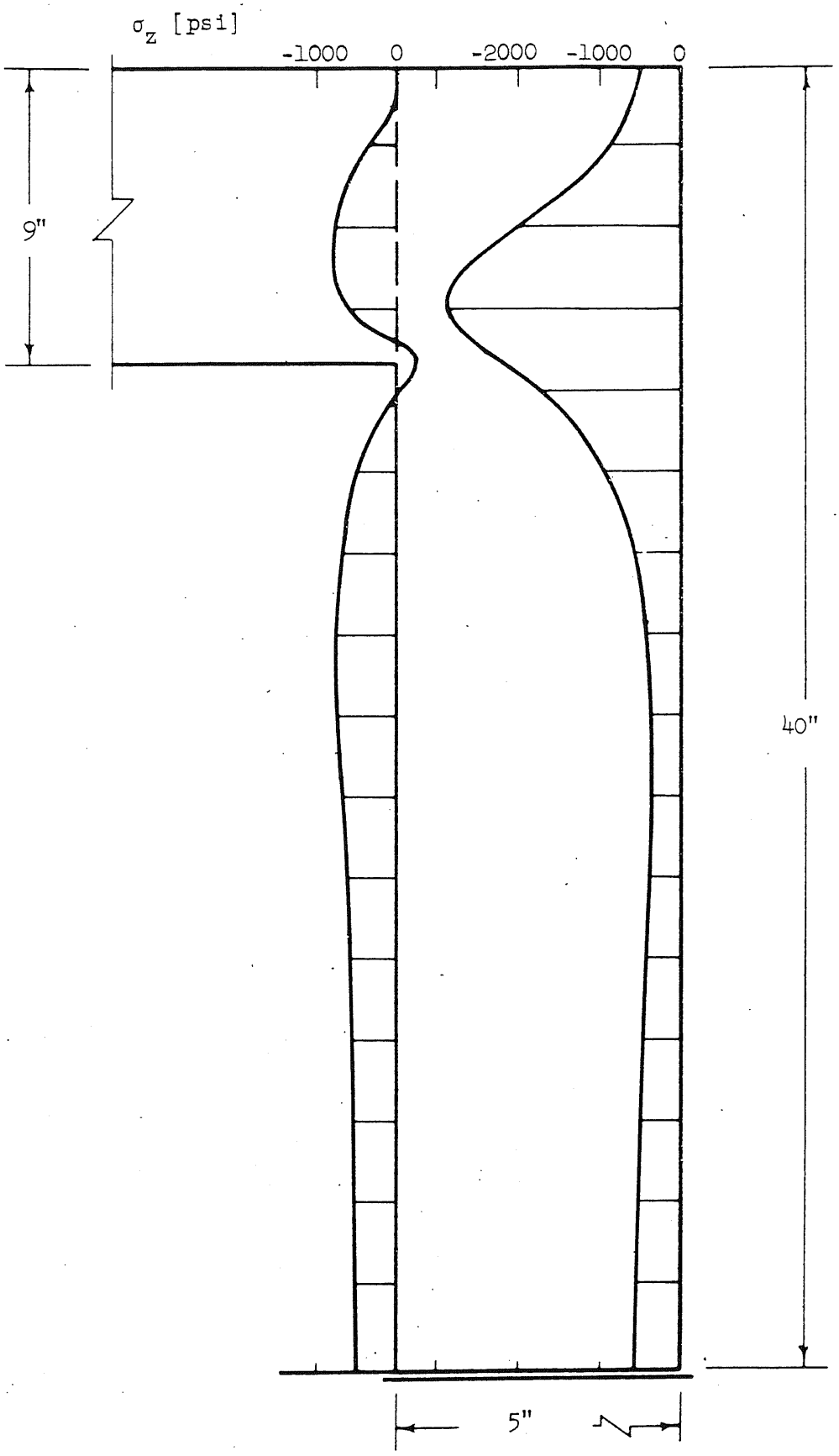

FIG. 36. LONGITUDINAL STRESSES IN THE CYLINDRICAL SIDE WALL FOR PRESSURE OF 666 PSI

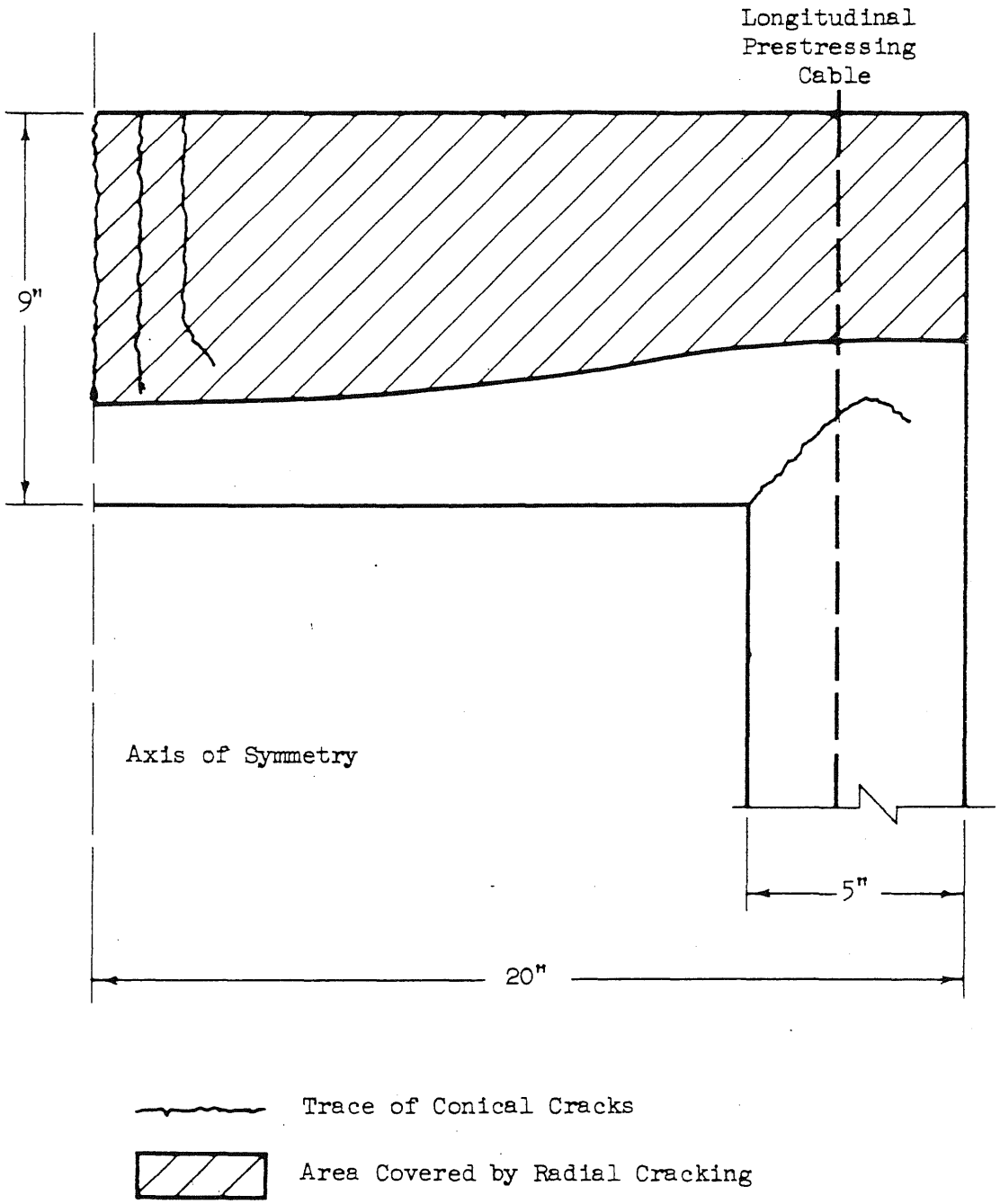

FIG. 37. EXTENT OF CRACKING FOR INTERNAL PRESSURE OF 666 PSI

APPENDIX

EQUILIBRIUM EQUATIONS OPERATORS

The finite difference-type operators presented here characterize the equations of equilibrium for some of the typical mass nodes in the grid. The corresponding equilibrium equations in terms of displacements have been derived according to the procedure outlined in Chapter II. When the numerical analysis is carried out, however, the equilibrium equations are generated within the computer. For the sake of simplicity, the stress nodes involved in these equations are considered to be in the elastic range.

The special notation introduced in the operator shown in Fig. A-5 is as follows,

$$C_c = \frac{1}{\left(\frac{1-\nu}{\lambda_r} + \frac{\nu}{D}\right)}$$

$$A_1 = \frac{1}{2\lambda_r\lambda_z}\left[(1-2\nu) + \frac{\nu^2}{r_i} C_c\right]$$

$$A_2 = \left(\frac{1}{\lambda r} + \frac{1}{2r_i} - \frac{\nu C_c}{2\lambda_r r_i}\right)$$

$$A_3 = -\frac{2E_{st}A_{cp}}{D^2}\frac{A_2}{2r_{i+1}}$$

$$A_4 = -\left(\frac{1}{\lambda_r} - \frac{1}{2r_i}\right)\left(\frac{1-\nu}{\lambda_r} + \frac{\nu}{2r_{i-1}}\right)$$

$$A_5 = -\frac{\nu C_c}{2\lambda_r r_i}\left(\frac{1-\nu}{\lambda_r} - \frac{\nu}{D}\right)$$

The displacement equilibrium equations for the typical interior node are given below for reference.

The equation in the r direction at node (i,j) is:

$$\left[\frac{(1-2\nu)}{2\lambda_z^2}\right] u_{ij+2} + \left\{-\frac{\nu}{2\lambda_z r_i}\right\} w_{ij+2} + \left\{-\frac{1}{2\lambda_z}\left(\frac{1}{\lambda_r} - \frac{\nu}{r_i}\right)\right\} w_{i-1j+1}$$

$$+ \left[\frac{(1-\nu)}{\lambda_r}\left(\frac{1}{\lambda_r} - \frac{1}{2r_i}\right)\right] u_{i-2j} + \left\{\frac{1}{2\lambda_z}\left(\frac{1}{\lambda_r} + \frac{\nu}{r_i}\right)\right\} w_{i+1j+1}$$

$$+ \left[-2\frac{(1-\nu)}{\lambda_r^2} - \frac{(1-\nu)}{r_i^2} - \frac{(1-2\nu)}{\lambda_z^2}\right] u_{ij} + \left\{\frac{1}{2\lambda_z}\left(\frac{1}{\lambda_r} - \frac{\nu}{r_i}\right)\right\} w_{i-1j-1}$$

$$+ \left[\frac{(1-\nu)}{\lambda_r}\left(\frac{1}{\lambda_r} + \frac{1}{2r_i}\right)\right] u_{i+2j} + \left\{-\frac{1}{2\lambda_z}\left(\frac{1}{\lambda_r} + \frac{\nu}{r_i}\right)\right\} w_{i+1j-1}$$

$$+ \left[\frac{(1-2\nu)}{2\lambda_z^2}\right] u_{ij-2} + \left\{\frac{\nu}{2\lambda_z r_i}\right\} w_{ij-2} = 0$$

The equilibrium equation in the z direction at node (i,j) is:

$$\left\{\frac{(1-\nu)}{\lambda_z^2}\right\} w_{ij+2} + \left[-\frac{1}{2\lambda_z}\left(\frac{1}{\lambda_r} - \frac{1}{2r_i}\right)\right] u_{i-1j+1}$$

$$+ \left\{\frac{(1-2\nu)}{2\lambda_r}\left(\frac{1}{\lambda_r} - \frac{1}{2r_i}\right)\right\} + \left[\frac{1}{2\lambda_z}\left(\frac{1}{\lambda_r} + \frac{1}{2r_i}\right)\right] u_{i+1j+1}$$

$$+ \left\{-2\frac{(1-\nu)}{\lambda_z^2} - \frac{(1-2\nu)}{\lambda_r^2}\right\} w_{ij} + \left[\frac{1}{2\lambda_z}\left(\frac{1}{\lambda_r} - \frac{1}{2r_i}\right)\right] u_{i-1j-1}$$

$$+ \left\{\frac{(1-2\nu)}{2\lambda_r}\left(\frac{1}{\lambda_r} + \frac{1}{2r_i}\right)\right\} w_{i+2j} + \left[-\frac{1}{2\lambda_z}\left(\frac{1}{\lambda_r} + \frac{1}{2r_i}\right)\right] u_{i+ij-1}$$

$$+ \left\{\frac{(1-\nu)}{\lambda_z^2}\right\} w_{ij-2} = 0$$

A sample of the equilibrium equations operators is presented in Figs. A-1 through A-8.

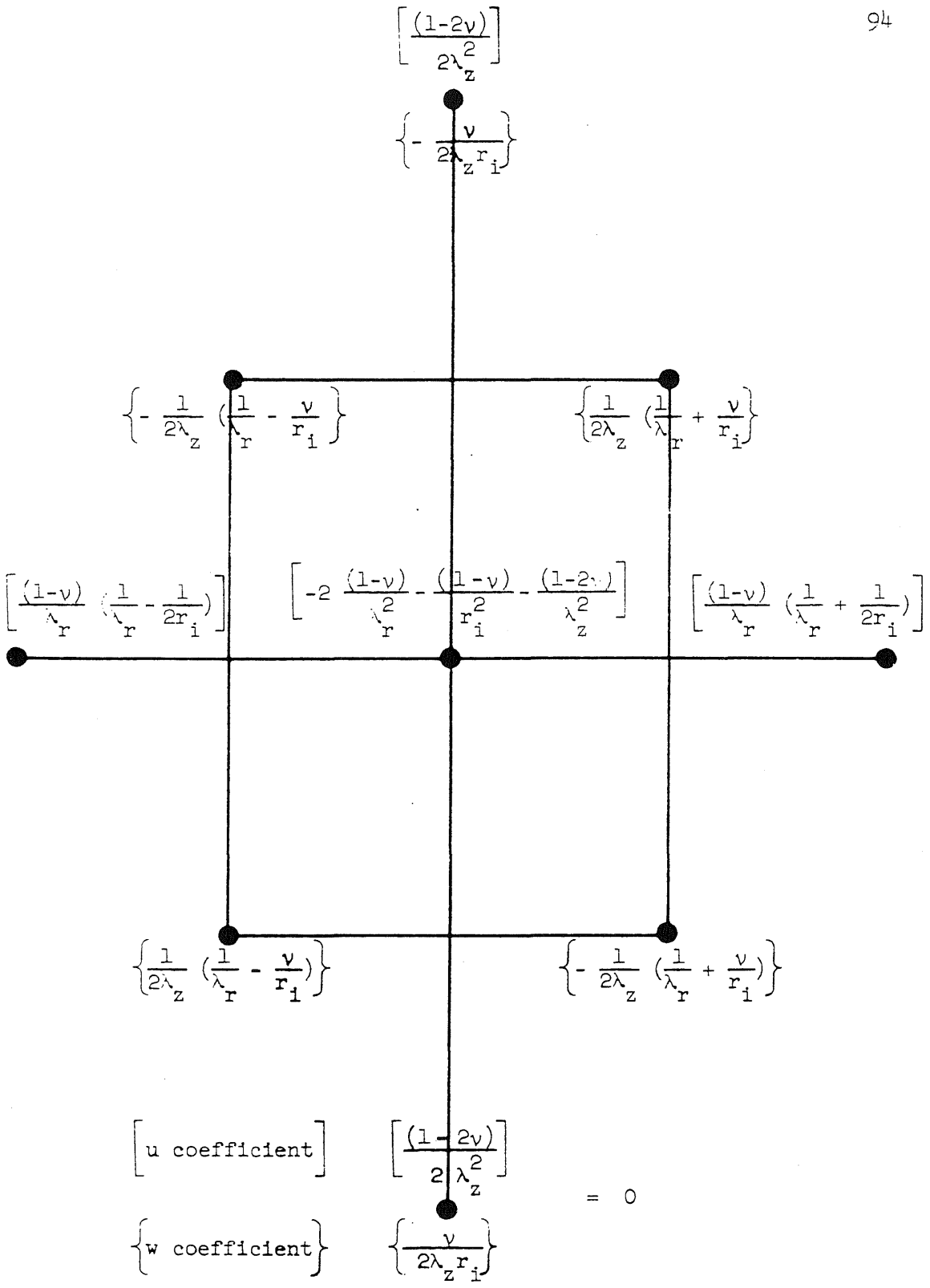

FIG. A-1. R EQUATION OPERATOR FOR A TYPICAL INTERIOR NODE

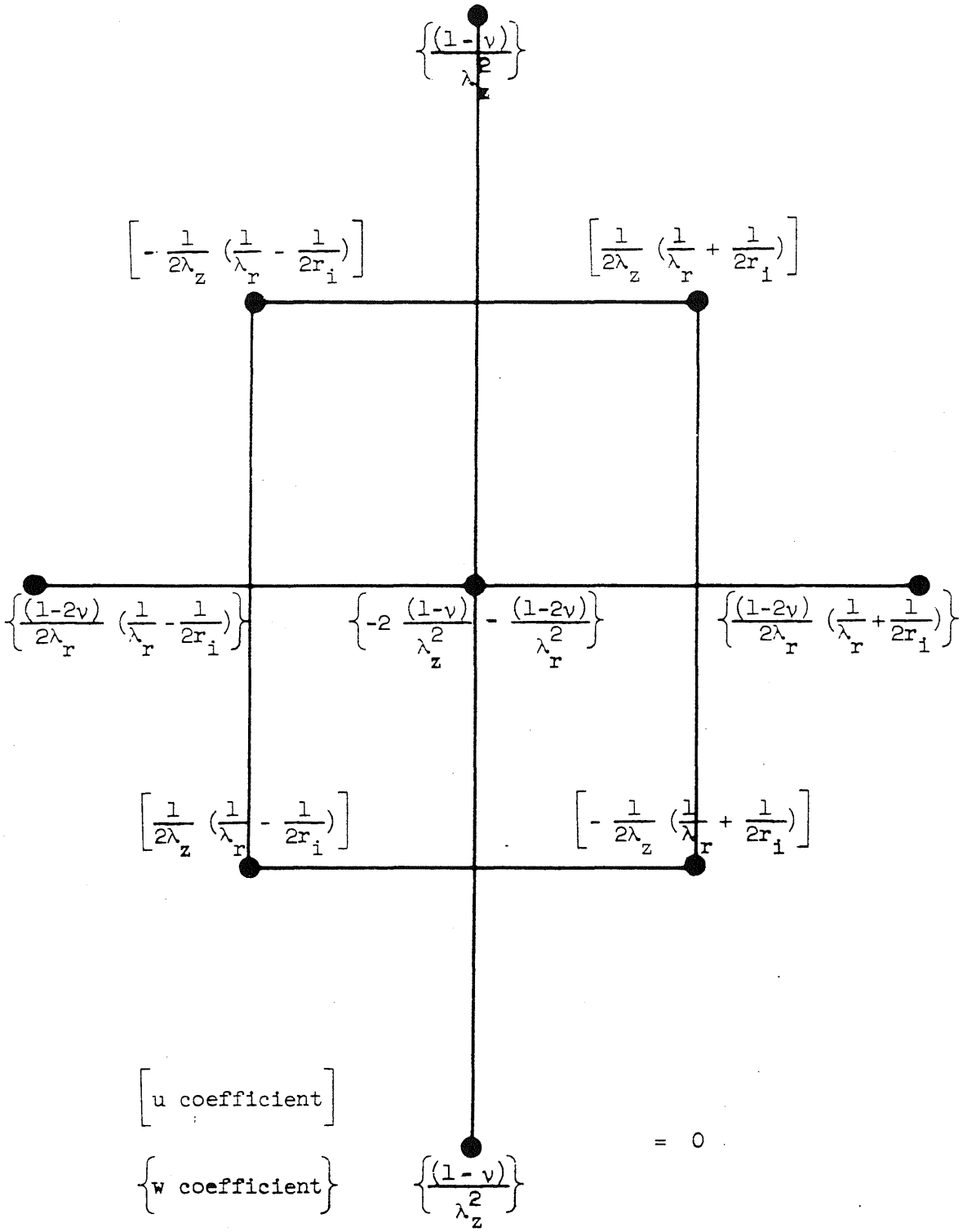

FIG. A-2. Z EQUATION OPERATOR FOR A TYPICAL INTERIOR NODE

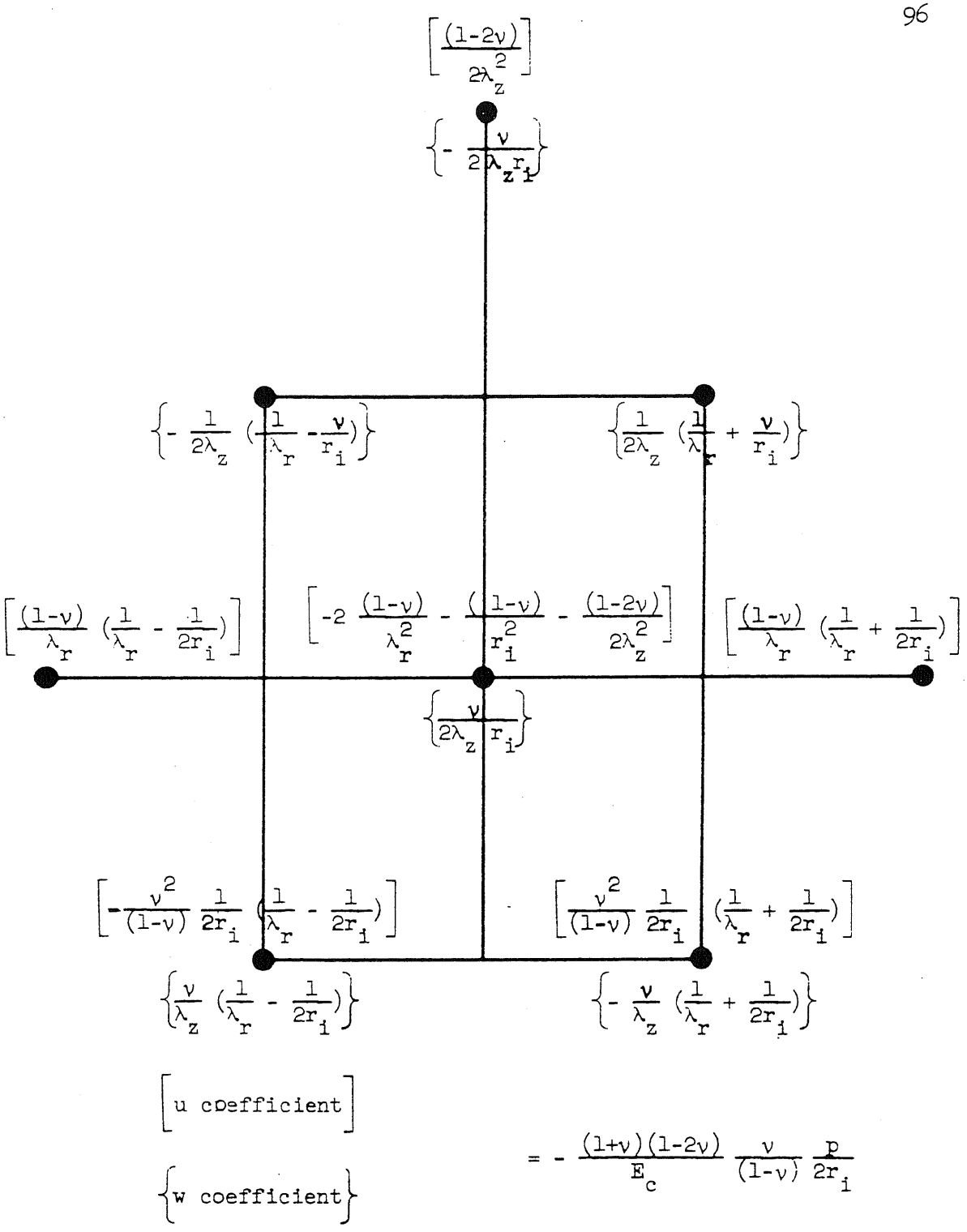

FIG. A-3. R EQUATION OPERATOR FOR A TYPICAL NODE HALF SPACE ABOVE THE LOWER FACE OF THE SLAB

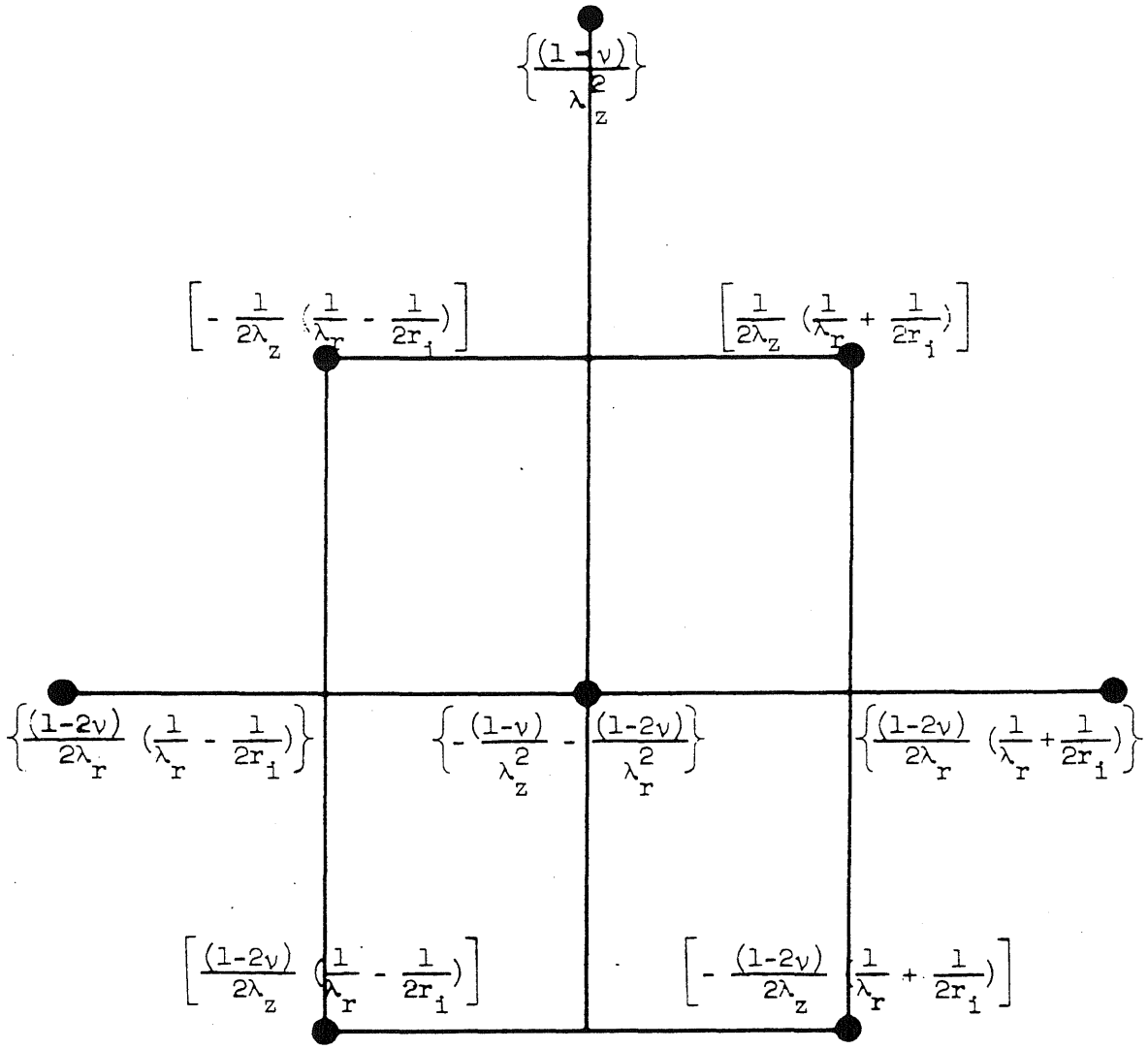

FIG. A-4. Z EQUATION OPERATOR FOR A TYPICAL NODE HALF SPACE ABOVE THE LOWER FACE OF THE SLAB

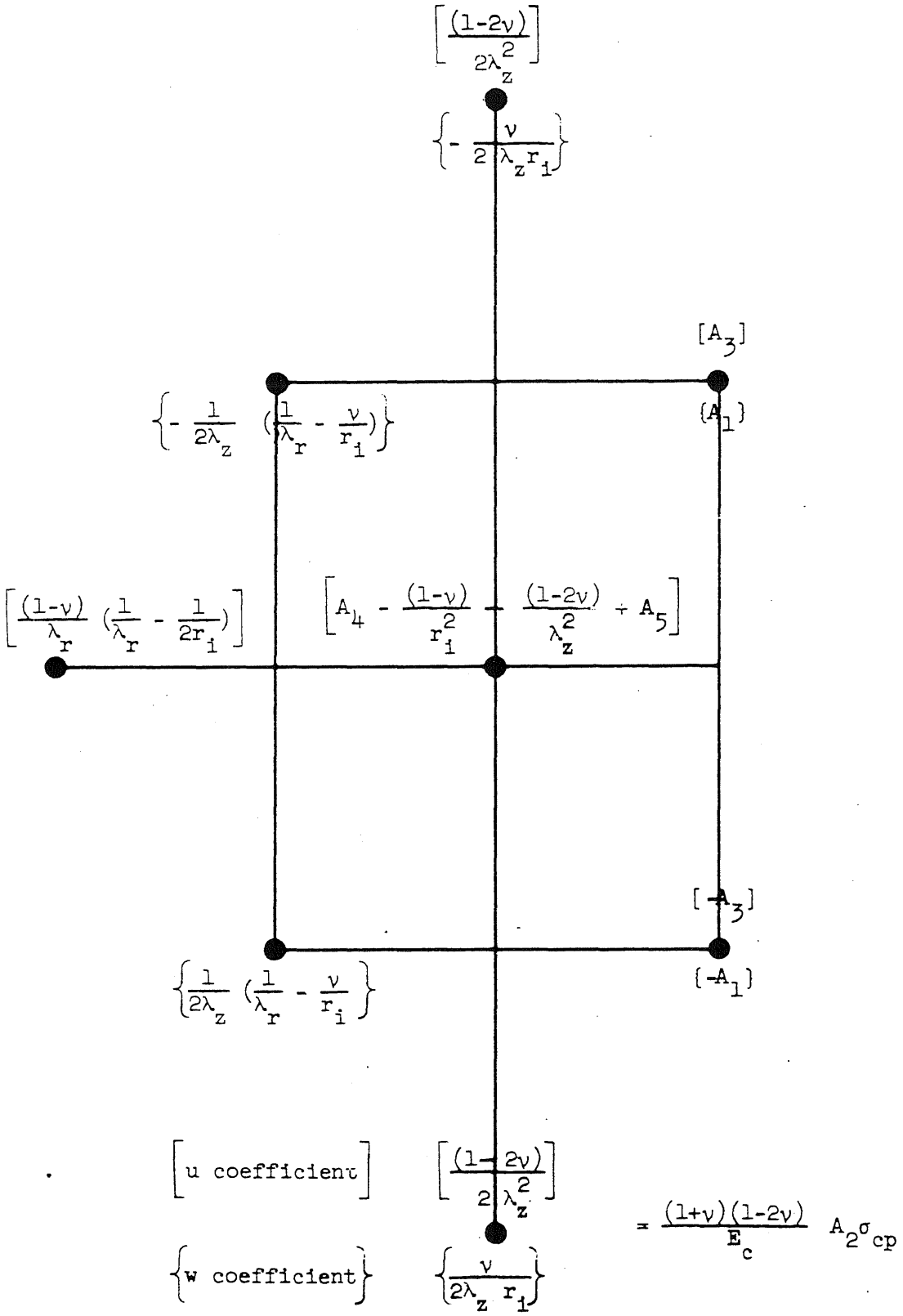

FIG. A-5. R EQUATION OPERATOR FOR A TYPICAL NODE HALF SPACE FROM THE EXTERIOR FACE OF THE WALL

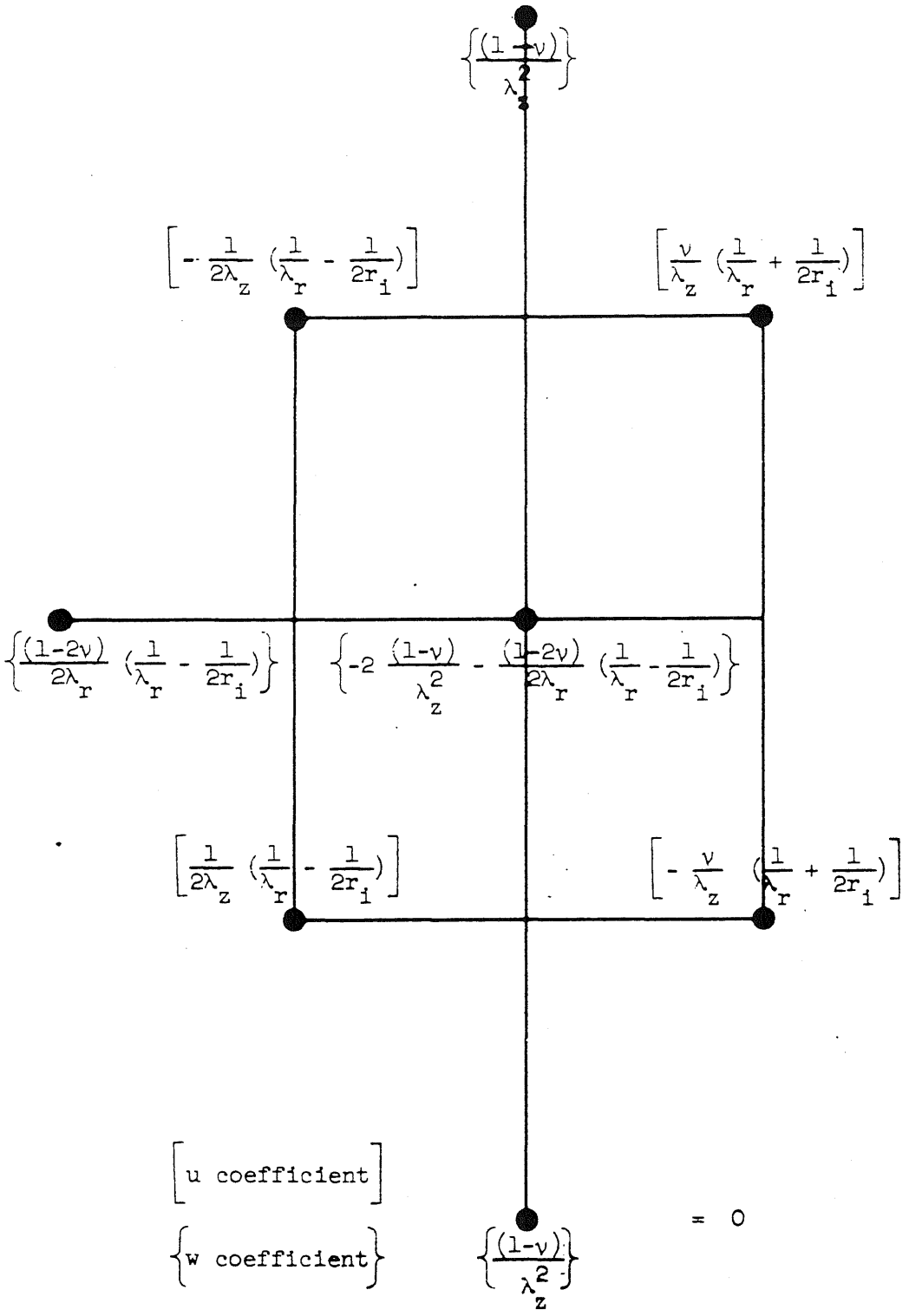

FIG. A-6. Z EQUATION OPERATOR FOR A TYPICAL NODE HALF SPACE FROM THE EXTERIOR FACE OF THE WALL

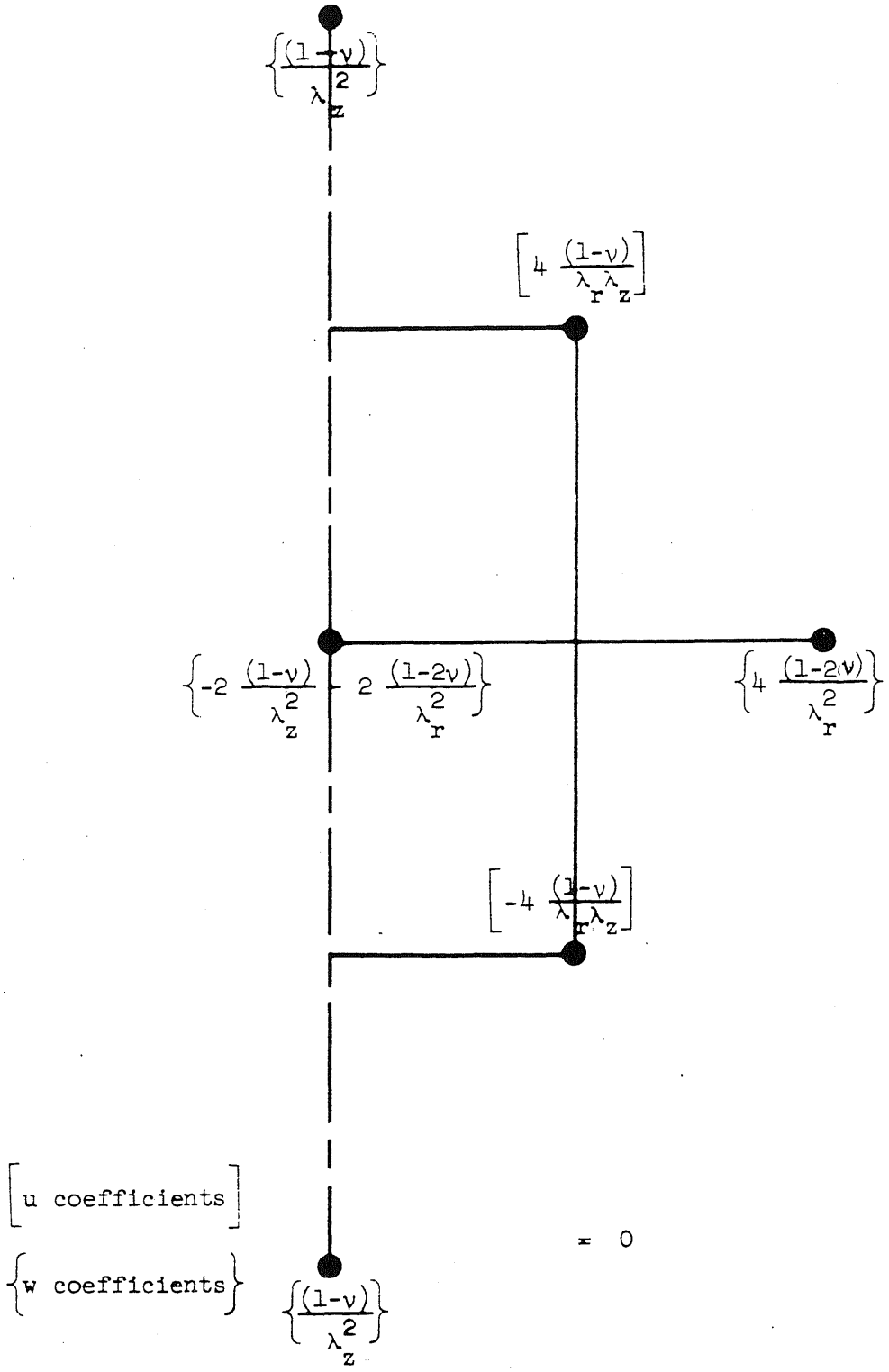

FIG. A-7. Z EQUATION OPERATOR FOR A TYPICAL NODE ON THE AXIS OF SYMMETRY

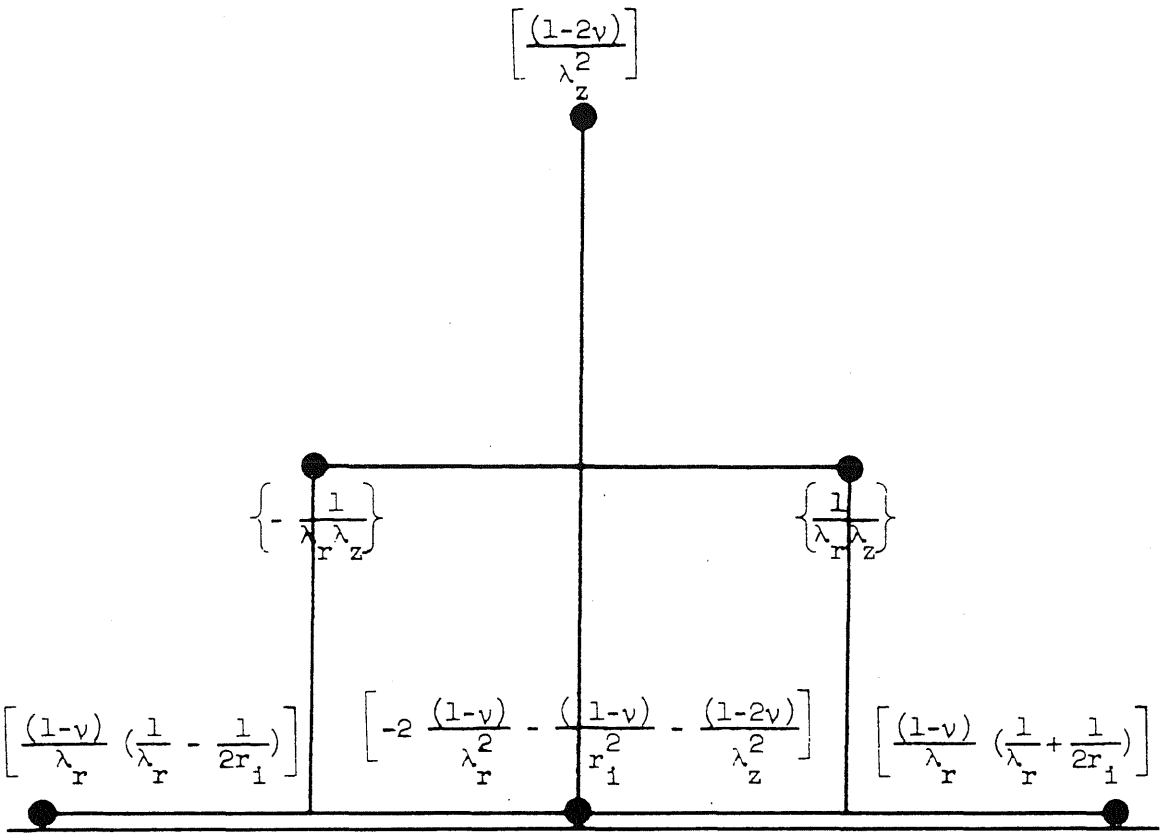

FIG. A-8. R EQUATION OPERATOR FOR A TYPICAL NODE AT MID-HEIGHT OF THE VESSEL